Development of a methodology for LES of Turbulent Cavitating Flows

A DISSERTATION
SUBMITTED TO THE FACULTY OF THE GRADUATE SCHOOL
OF THE UNIVERSITY OF MINNESOTA
BY

Aswin Gnanaskandan

IN PARTIAL FULFILLMENT OF THE REQUIREMENTS
FOR THE DEGREE OF
DOCTOR OF PHILOSOPHY

Krishnan Mahesh, Adviser

July, 2015

Acknowledgements

கற்றது கைமண் அளவு, கல்லாதது உலகளவு
Known is a drop, unknown is an ocean

A number of people have been helpful in my quest to explore this wonderful field of 'Fluid Dynamics' and it is my utmost duty to thank each and everyone of them.

My first and foremost thanks should go to my academic adviser Prof. Krishnan Mahesh. His knowledge and guidance have been instrumental in aiding the completion of my research work. His eagerness to look at my results and reply with comments even after 9 P.M. is a quality I would like to emulate in my future. I have learned a lot about scientific thinking and writing from him.

I thank Prof. Roger Arndt, Prof. Ellen Longmire and Prof. Paul Strykowski for being in my examination committee and reviewing my thesis. This work was supported by the United States Office of Naval Research (ONR) under ONR Grant N00014-11-1-0497 with Dr. Ki-Han Kim as technical monitor. Computing resources from the Arctic Region Supercomputing Center (ARSC), Minnesota Supercomputing Institute (MSI), and Texas Advanced Computing Center (TACC) are duly acknowledged.

Many thanks to my mother, father, sister, brother–in–law and nephew for their constant support and encouragement. The regular telephone conversations with them have been energizing and made me miss my home a lot lesser. Without the never–changing "What did you eat today ?" from my mother, no matter what, I think life would have been very boring. My grandfather is the main reason for whatever little discipline I have in my life and I owe him for that.

I owe a lot to Sriram and Aarthi, my adopted brother and sister, who gave me a home away from home in Minnesota. The love they showered on a complete stranger (a.k.a yours truly) speaks a lot about the wonderful kind of people they are. They are definitely a role model for me when it comes to friendship. Conversations with my childhood friends Dinesh, Cheena, Murthy and Gokul have been few and far between. However, the friendship continues unabated. Many thanks to them for being great friends. I owe a lot to Zareen for being an amazing friend and helping me learn invaluable life lessons.

My sincere thanks to Praggy, Chandru and Savio, three great friends I found here in Minnesota. Special thanks to Praggy for answering many of my silly questions and helping me hone my writing skills. Many hours have been spent happily at coffee sessions with Praggy, Savio, Ranga, Raja, Janani, Thavil and Rohini. Those sessions have definitely enriched both my technical and general knowledge. I also thank Bala, Ganesh, Kaarthick and Siva who have made my stay at Minnesota really memorable.

I thank all the past and current group members of Mahesh's lab for their help, jovial chats and friday lunches. Special thanks to Dr. Suman Muppidi and Mr. Zane Nitzkorski for their help during the initial stages of my PhD. I also thank Dr. Aman Verma, Dr. Xiachuan Chai, Mr. Praveen Kumar, Mr. Karim Alame, Ms. Yixuan Li and Mr. Mrugank Bhatt.

Thanks to two wonderful people, Dr. K. Anandhanarayanan and Sreejith whose passion and enthusiasm for fluid dynamics have made a huge impact on me and kindled in me the curiosity to learn more.

Big thanks to my wife Poorna. Her constant encouragement has gone a long way in helping me complete my thesis. I cannot ask for a more supportive wife, a better friend and a wiser partner.

To my Thaatha, Paati, Appa, Amma and Poorna

Abstract

The objective of this dissertation is to develop a numerical methodology for large eddy simulation of multiphase cavitating flows on unstructured grids and apply it to study two cavitating flow problems. The multiphase medium is represented using a homogeneous mixture model that assumes thermal equilibrium between the liquid and vapor phases. We develop a predictor-corrector approach to solve the governing Navier Stokes equations for the liquid/vapor mixture, together with the transport equation for the vapor mass fraction. While a non-dissipative and symmetric scheme is used in the predictor step, a novel characteristic-based filtering scheme with a second order TVD filter is developed for the corrector step to handle shocks and material discontinuities in non-ideal gases and mixtures. Additionally, a sensor based on vapor volume fraction is proposed to localize dissipation to the vicinity of discontinuities. The scheme is first validated for one dimensional canonical problems to verify its accuracy in predicting jump conditions across material discontinuities and shocks. It is then applied to three turbulent cavitating flow problems - over a hydrofoil, over a hemisphere nose shaped body and over a wedge. Our results show that the simulations are in good agreement with experimental data for the above tested cases, and that the scheme can be successfully applied to RANS, LES and DNS methodologies.

We first study cavitation over a circular cylinder at two different Reynolds numbers ($Re = 200$ and 3900 based on cylinder diameter and free stream velocity) and four different cavitation numbers ($\sigma = 2.0, 1.0, 0.7$ and 0.5). Large Eddy Simulation (LES) is employed at the higher Reynolds number and Direct Numerical Simulations (DNS) at the lower Reynolds number. It is observed that the simulated cases fall into two

different cavitation regimes: cyclic and transitional. Cavitation is seen to significantly influence the evolution of pressure, boundary layer and loads on the cylinder surface. The cavitated shear layer rolls up into vortices, which are then shed from the cylinder, similar to a single phase flow. However, the Strouhal number corresponding to vortex shedding decreases as the flow cavitates and vorticity dilatation is found to play an important role in this reduction. At lower cavitation numbers, the entire vapor cavity detaches from the cylinder leaving the wake cavitation–free for a small period of time. This low frequency cavity detachment is found to occur due to a propagating condensation front and is discussed in detail. The effect of initial void fraction is assessed. The speed of sound in the free stream is altered as a result and the associated changes in the wake characteristics are discussed in detail. LES of cavitating flow at $Re = 3900$ and $\sigma = 1.0$ is studied and a higher mean cavity length is obtained when compared to the cavitating flow at $Re = 200$ and $\sigma = 1.0$. The wake characteristics are compared to the single phase results at the same Reynolds number and it is observed that cavitation suppresses turbulence in the near wake and delays three dimensional breakdown of the vortices.

LES of sheet to cloud cavitation over a wedge is performed at $Re = 200,000$ (based on the wedge height and free stream velocity) and $\sigma = 2.1$. The attached sheet cavity grows upto a length of $x/h = 2.0$, after which it breaks into a cloud cavity which is highly three–dimensional and vortical in nature. The mean and RMS void fraction profiles obtained inside the cavity are compared to experiment and good agreement is observed. The frequency of the shedding process is obtained from point spectra at several locations and the obtained frequency is found to agree with the experiment. It is observed that the mean pressure at the wedge apex does not fall below vapor pressure; however cavitation occurs there due to the unsteady pressure falling below vapor pressure. The maximum mean void fraction occurs in the sheet cavity and is about 0.5, while the cloud region has even lesser amount of void fraction. The velocity fluctuations immediately downstream of the cavity show dominant fluctuations in both the streamwise and spanwise directions, while only streamwise fluctuations are dominant inside the cavity region. The probability density function of void fraction examined at

several locations inside the cavity show that the mean value obtained from time averaged data is very different from the most probable value of void fraction, indicating the considerable unsteadiness of the flow. The pressure waves produced on cloud collapse are found to display both wave–like behavior and highly intermittent small–scale behavior downstream of the wedge. The pressure waves also impinge on the growing sheet cavity and affect the shedding process significantly.

Contents

List of Tables

List of Figures

Chapter 1

Introduction

1.1 Cavitation

Phase change from liquid to vapor can occur primarily due to two thermodynamic phenomena - boiling and cavitation. Boiling occurs when the vapor pressure of the liquid is increased above the ambient pressure by heating the liquid whereas cavitation refers to the formation of vapor when the ambient pressure in a liquid drops below vapor pressure. Cavitation is thus different from boiling in terms of the thermodynamic path that precedes the formation of vapor as illustrated in the phase diagram of water in Figure 1.1.

An important fluid property that governs cavitation is the vapor pressure (p_v), which is defined as the pressure exerted by the vapor in thermodynamic equilibrium with its condensed phase at a given temperature. Figure 1.2 shows the variation of vapor pressure of water with temperature. The vapor pressure of water at 298 K is 2700 Pa, while the vapor pressure at 373 K (boiling point of water) is atmospheric pressure. The difference between the ambient pressure and the vapor pressure is an indicator of whether cavitation can occur or not and hence a non–dimensional parameter termed cavitation number $\sigma = \dfrac{p_\infty - p_v}{0.5\rho_\infty u_\infty^2}$ is used to characterize cavitating flows. Here, p_∞, ρ_∞ and u_∞ are free stream pressure, density and velocity respectively.

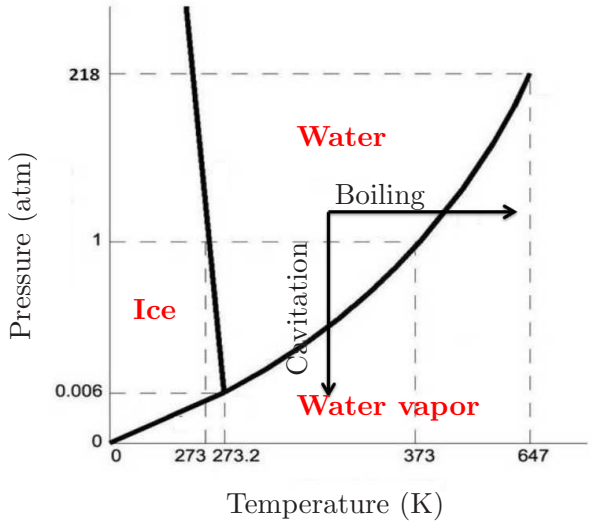

Figure 1.1: Phase diagram of water showing two different thermodynamic paths for boiling and cavitation.

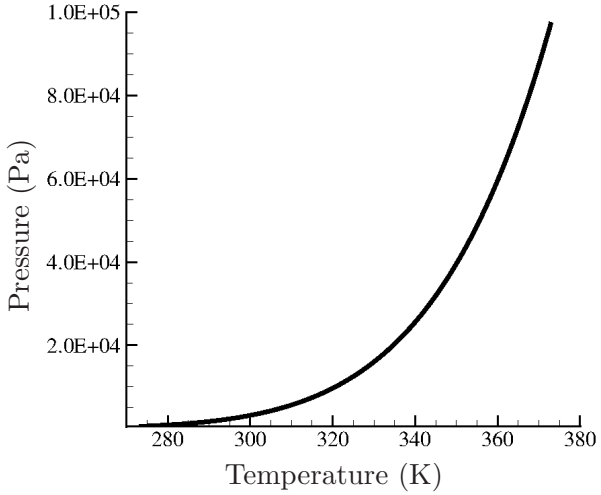

Figure 1.2: Variation of vapor pressure of water with temperature.

1.1.1 Types of cavitation

Cavitation can be classified as hydrodynamic, acoustic, optic or particle cavitation. Hydrodynamic cavitation is caused by pressure variations induced due to the geometry, while acoustic cavitation is caused by pressure variations due to a traveling acoustic wave. Optic and particle cavitation are caused due to local energy deposition using

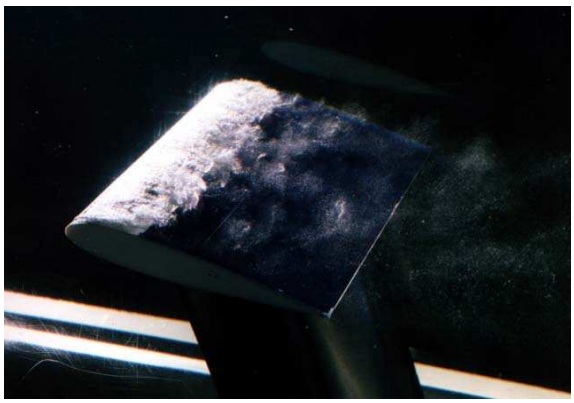

Figure 1.3: Partial sheet cavitation near the leading edge of a hydrofoil [1].

high intensity photons and charged particles respectively. This dissertation is mainly concerned with hydrodynamic cavitation; however the method developed can also be applied to study acoustic cavitation. Within hydrodynamic cavitation, there are three major classifications - fixed, traveling and vortex cavitation, based mainly on how the vapor cavities behave and the origin of low pressure that causes cavitation [11, 12].

Fixed Cavitation

Fixed cavitation occurs when a cavity or a pocket of vapor remains attached to a solid surface around which the liquid flows. Minor unsteady oscillations within the cavity or at the cavity closure are always possible: however a major portion of the cavity remains attached at a fixed position. Since the variations in the vapor volume are small, this generally does not cause lot of noise or vibration. An example is cavitation at the leading edge of a hydrofoil, which is commonly called a partial cavity or sheet cavity. Figure 1.3 shows an image of sheet cavitation near the leading edge of a hydrofoil. Note that the cavity is largely two dimensional except for span–wise variations near the cavity closure.

Figure 1.4: Sheet to cloud cavitation over a hydrofoil with a detached cloud cavity [1].

Traveling Cavitation

Traveling cavitation occurs when bubbles or large vapor cavities form in a liquid and convect along with the flow. When they encounter high pressures, they collapse violently leading to large amounts of noise and vibration. Examples of traveling cavitation are bubble and cloud cavitation. The most commonly encountered situation is the transition from a sheet cavity to a cloud cavity. Figure 1.4 shows an image of the sheet to cloud cavitation transition. A part of the sheet cavity breaks off into a large cloud which can travel downstream and collapse violently.

Vortex Cavitation

Vortex cavitation occurs in the low pressure core of vortices. Examples include apex vortex cavitation along the leading edge of delta wings and tip vortex cavitation occurring at the tip of rotating propeller blades. Vortices formed in turbulent shear layers and shedding Karman vortices behind a bluff body are additional examples. Figure 1.5 shows an image of cavitation occurring within the tip vortices of a propeller blade.

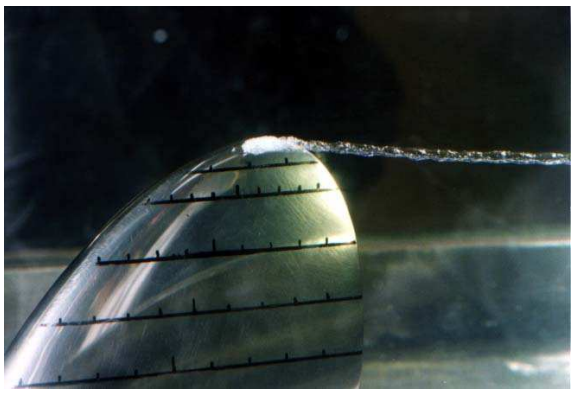

Figure 1.5: Tip vortex cavitation on a rotating propeller blade [1].

1.2 Motivation

Cavitation in many cases, is detrimental. Examples where cavitation can cause damage include pumps, propellers and hydraulic machinery, where vibration and surface erosion caused due to cavitation not only lead to adverse performance, but also reduce the overall structural integrity. The vapor pockets produced by cavitation can collapse near a solid surface generating high impact loads on the surface. Figure 1.6 shows a propeller blade damaged due to cavitation. Note the concentrated damage on the tip of the propeller blade where the speed of the blade is maximum. Erosion due to cavitation can cause undesirable noise in addition to weakening the structural integrity of the propeller. Cavitation has some beneficial effects too. For example, it is used to homogenize, mix and break down suspended particles in a colloidal liquid. Shock wave lithotripsy, a procedure to destroy kidney stones employs cavitation to achieve its end. In industrial cleaning applications, the violent nature of cavitation is used to overcome particle-substrate adhesion forces to loosen contaminants from substrate. The importance of studying cavitation lies in its occurrence in these wide array of applications. A thorough understanding of cavitation is therefore imperative, if we are to reduce the detrimental effects it causes while also exploiting its beneficial effects.

A study of cavitation can be realized both experimentally and through numerical simulations. Experimental investigation of cavitation has drastically improved our

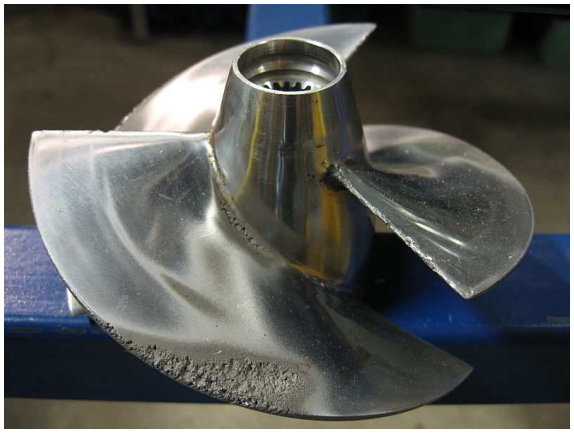

Figure 1.6: Propeller blade showing erosion near the tip due to cavitation [1].

understanding of the phenomenon over the last several years [13, 14]. However experimental measurements in cavitating flows are quite challenging; numerical simulations can therefore potentially fill critical gaps in our understanding. It is possible to simulate a large number of cases, test, validate and predict their outcomes. This can be cost-effective and also permit predicting the outcome of scenarios that may otherwise be very difficult to test experimentally. Validated simulations can also yield quantities that might be impossible to measure experimentally. Further, advanced post–processing techniques enable insight into the three–dimensional nature of cavitating flows that are difficult to extract experimentally. The numerical simulation of cavitating flows, nevertheless, has its set of challenges. Cavitating flows pose the inherent challenge of ranging over a wide array of length and time scales. Additionally, the formation of vapor is often followed by growth of vapor cavities which not only vary in size but also form and collapse at different rates, making their prediction difficult.

In order to address these challenges, many simulation methods have been developed. Traditionally time averaged methods like Reynolds Averaged Navier–Stokes (RANS) method have been used to simulate cavitation. RANS uses the Reynolds Averaged equations where an instantaneous quantity is decomposed into its time-averaged and fluctuating quantities. While the time–averaged quantities are solved for, the Reynolds stress terms containing the non–linear fluctuation terms have to be modeled. Existing

RANS models require an ad–hoc suppression of the eddy viscosity and can be inaccurate in the highly unsteady sheet to cloud transition regime. Direct Numerical Simulation (DNS) is a methodology where all relevant scales of turbulence are directly resolved on the computational grid. However, practical flows have high Reynolds number and a large range of length and time scales which makes DNS prohibitively expensive. Large Eddy Simulation (LES) is proving to be a viable tool to simulate complex flows due to the recent advances in parallel computing and numerical methods. LES resolves larger length scales and models the small unresolved scales to account for the inter–scale interaction between the resolved and unresolved scales. As a result, LES is computationally cheaper than DNS, and hence viable for practical complex flows. An overall objective of this dissertation work is to develop a novel method for LES of turbulent cavitating flows.

1.3 Overview

This dissertation develops a LES methodology for cavitating flows and applies it to study two different types of cavitation: vortex cavitation on a circular cylinder and sheet to cloud cavitation over a wedge. A LES methodology for cavitation is developed using a homogeneous mixture model. Then, the methodology is applied to study the wake characteristics of a cavitating flow over a circular cylinder at different Reynolds numbers and cavitation numbers. Finally, sheet to cloud cavitation over a wedge is studied at one Reynolds number and cavitation number and the mechanism of sheet to cloud cavitation is explored in detail. A review of relevant past work is included in appropriate chapters of this dissertation. The principal contributions of this work are as follows:

- A numerical method for simulation of turbulent cavitating flows is developed. A novel predictor–corrector type algorithm is used to solve the governing differential equations. The novelty of the method lies in the corrector step of the algorithm, where a characteristic–based filtering method has been developed for multiphase flows for the first time.

- A sensor based on divergence and void fraction is proposed to localize dissipation to the vicinity of shocks and material discontinuities. This is an important step to predict smaller scales in a turbulent flow.

- It is demonstrated that solving for a non–conserved internal energy is numerically better than solving for conserved total energy. The viscous dissipation term in the energy equation is expressed in a form that ensures that it is always positive.

- The proposed methodology is validated by simulating a number of canonical problems and comparing to analytical solutions. The method is further validated against experimental results for a turbulent cavitating flow over a hydrofoil, a hemispherical nose shaped body and a wedge.

- The numerical method is applied to investigate vortex cavitation behind a bluff body. A circular cylinder is chosen for this purpose and cavitating flow at two different Reynolds number and four different cavitation numbers are studied in detail. The study reveals the mechanism behind the reduction of vortex shedding frequency in cavitating flows. It is shown that vorticity dilatation caused due to cavitation is the main reason for the reduction in vortex shedding frequency.

- The effect of initial void fraction on the flow field is investigated in detail. The speed of sound in the medium is altered as a result and hence all acoustic related phenomena are affected. It is seen that the pressure change produced in the medium is higher on reducing the initial void fraction and the corresponding loads experienced by the body is also higher.

- LES of cavitating flow at $Re = 3900$ based on cylinder diameter and $\sigma = 1.0$ is performed and the wake characteristics are studied in detail. It is shown that cavitation suppresses turbulence and delays three dimensional breakdown of Karman vortices.

- Sheet to cloud cavitation over a wedge is studied using LES at $Re = 200,000$ based on wedge height and $\sigma = 2.1$.

- The mean and RMS void fraction profiles obtained are compared to experiment and good agreement is observed. The Strouhal number corresponding to cavity auto–oscillation is also predicted well in the simulation.

- It is found that the mean pressure inside the flow does not fall below vapor pressure; but flow unsteadiness causes the pressure to fall below vapor pressure thus causing cavitation. The velocity fluctuations inside the cavity and the probability density functions of void fraction are used to quantify the unsteadiness of the flow inside and downstream of the cavity.

- The three–dimensional nature of the flow is captured in the simulation and the process of sheet to cloud transition is described. The pressure waves produced on cavity collapse is found to exhibit both wave–like and intermittent behavior.

1.4 Outline

The dissertation is organized as follows. Chapter 2 explains the physical model used in the simulations. It also outlines the governing equations being solved and the novel predictor–corrector method used to numerically solve the equations. Chapter 3 describes the validation cases that test the accuracy of the proposed methodology. Chapter 4 applies the numerical method to study cavitation behind a circular cylinder at two low Reynolds numbers. The mechanism of vortex cavitation and its effect on the wake of the cylinder are discussed in detail. Chapter 5 explains the application of the method to study turbulent sheet to cloud cavitation over a wedge. The mechanism of sheet to cloud cavitation transition and the internal structure of the vapor cavity are investigated in detail. Finally, Chapter 6 provides a brief summary of the dissertation.

Chapter 2

Physical Model and Numerical Method

2.1 Introduction

The most commonly used physical model to simulate cavitating flows is the homogeneous mixture model. It treats the mixture of water and vapor as a single compressible fluid, and solves a separate transport equation for the mass fraction of vapor [15–24]. The key differences between commonly used physical models lie in the constitutive equation of state and the mass transfer model. Frikha et al. [25] provide a review of the different mass transfer models used. Almost all of the simulations mentioned above have used the RANS methodology. However in recent times, DES and LES are also being considered as viable options [26–31]. Also, most past simulations invoke the isothermal assumption for cavitation in water. It is known that this assumption is not valid for thermosensitive fluids like cryogenic fluids where an energy equation needs to be solved [32–34]. In this study, we use the homogeneous mixture approach with a non-barotropic equation of state for water. In order to maintain a general framework, we have solved an energy equation. In the current investigation, we have focused on hydrodynamic cavitation. The method however, can be applied to thermosensitive fluids as well. The latent heat of evaporation is not considered in this study. The reason behind this is the fact that

the mass of vapor produced by cavitation is small for all the test cases considered and hence the amount of latent heat absorbed by this mass is negligible.

A turbulent cavitating flow has a broadband spectrum which requires non dissipative numerical schemes [35, 36] to represent small scales accurately. However, non-dissipative schemes can become unstable at high Reynolds numbers. Furthermore, cavitation is characterized by large gradients in density and strong pressure waves formed during vapor cloud collapse. Accurate representation of turbulence in the presence of these strong gradients is a significant challenge and requires appropriate discontinuity capturing methods. Classical monotonic discontinuity-capturing methods are too dissipative and not suitable for turbulent simulations. Modern discontinuity capturing methods like total variation diminishing (TVD) schemes, essentially non-oscillatory (ENO) schemes and monotone upstream-centered schemes for conservation laws (MUSCL) typically incur higher computational cost for achieving higher order of accuracy in the vicinity of discontinuities. Further, these schemes require special treatment near boundaries [37]. Yee et al. [37] proposed a class of filters called 'characteristic filters', that add the dissipative part of a traditional shock capturing method to a non-dissipative base scheme. They developed this method for ideal gases on structured grids; Park and Mahesh [38] proposed an extension to unstructured grids. Numerical boundary conditions for these filters can be same as the existing base schemes, which is an added advantage. Further, the characteristic filter can be applied to the solution once, after a full time step, and hence is considerably cheaper than the TVD, ENO and MUSCL schemes [39]. A simple linear filter was first proposed by Gustafsson and Olsson [40], which provides a linear second order dissipation. Yee et al. [37] then used a second order non-linear TVD filter that takes into account the different wave characteristics of the Euler equations. Both lower order TVD or higher order ENO/WENO type terms can be used as characteristic filters. Lo et al. [39] observed that WENO type filters perform marginally better than lower order TVD filters and also found WENO type filters to be insensitive to the tunable parameters that appear in the shock capturing scheme. Both Park and Mahesh [38] and Lo et al. [39] observed that the original combination of TVD filter and Harten's artificial compression method (ACM) switch [41] proposed by Yee et al.

[37] was not able to distinguish between turbulent fluctuations and shocks, and hence proposed modified switch terms.

2.2 Governing equations

We use a homogeneous mixture model that assumes thermal and mechanical equilibrium between the phases i.e. there is no slip velocity or temperature difference between the phases. Also, surface tension effects are ignored. The constituent phases are treated as a single compressible fluid whose density

$$\rho = \rho_l(1-\alpha) + \rho_g\alpha, \tag{2.1}$$

where ρ_l is the density of liquid and ρ_g is the density of vapor. α is the vapor volume fraction which is related to the vapor mass fraction (Y) by

$$\rho_l(1-\alpha) = \rho(1-Y) \quad \text{and} \quad \rho_g\alpha = \rho Y. \tag{2.2}$$

The governing equations are the Navier-Stokes equations along with a transport equation for the mass fraction of vapor:

$$\begin{aligned} \frac{\partial \rho}{\partial t} &= -\frac{\partial}{\partial x_k}\left(\rho u_k\right), \\ \frac{\partial \rho u_i}{\partial t} &= -\frac{\partial}{\partial x_k}\left(\rho u_i u_k + p\delta_{ik} - \sigma_{ik}\right), \\ \frac{\partial \rho Y}{\partial t} &= -\frac{\partial}{\partial x_k}\left(\rho Y u_k\right) + S_e - S_c, \end{aligned} \tag{2.3}$$

where ρ, u_i and p are density, velocity and pressure respectively of the mixture. For energy transport, both total energy and internal energy forms are considered. Their relative merits and demerits are discussed in Section 3.2. The internal energy form is

used for the results shown unless specified otherwise.

$$\begin{aligned}
\frac{\partial E_T}{\partial t} &= -\frac{\partial}{\partial x_k}\left\{\left(E_T + p\right)u_k - \sigma_{ik}u_i - Q_k\right\}, \\
\frac{\partial \rho e_s}{\partial t} &= -\frac{\partial}{\partial x_k}\left(\rho e_s u_k - Q_k\right) - p\frac{\partial u_k}{\partial x_k} + \sigma_{ik}\frac{\partial u_i}{\partial x_k}.
\end{aligned} \tag{2.4}$$

Here E_T and e_s are total energy and internal energy respectively.

$$\begin{aligned}
\rho e_s &= \rho_l e_l(1-\alpha) + \rho_g e_g \alpha, \text{ where} \\
e_l &= C_{vl}T + \frac{P_c}{\rho_l}, \\
e_g &= C_{vg}T, \\
\rho e_s &= \rho C_{vm}T + \rho(1-Y)\frac{P_c K_l T}{p+P_c} \text{ and} \\
E_T &= \rho e_s + \frac{1}{2}\rho u_k u_k.
\end{aligned} \tag{2.5}$$

Here, e_l and e_g are the internal energies of liquid and gas respectively. C_{vl} and C_{vg} are the specific heats at constant volume for liquid and vapor respectively and C_{pl} and C_{pg} are the specific heats at constant pressure. The system is closed using a mixture equation of state based on stiffened equation of state for water and ideal gas equation for vapor.

$$p = Y\rho R_g T + (1-Y)\rho K_l T\frac{p}{p+P_c}. \tag{2.6}$$

Here, $R_g = 461.6$ J/KgK, $K_l = 2684.075$ J/KgK and $P_c = 786.333$ x 10^6 are constants associated with the equation of state of vapor and liquid. The density and speed of sound predicted by the stiffened equation of state are compared to the National Institute of Standards and Technology (NIST) data in Figure 2.1 (a) and good agreement is observed. However the stiffened equation of state under-predicts the value of specific heat at constant volume C_{vl} (predicts it to be 1500.3 J/KgK as opposed to the NIST value of 4157.4 J/KgK). This is not seen as a serious drawback in the current study because, heat transfer effects within the liquid phase are small in hydrodynamic cavitation at ambient pressure and temperature. A more accurate equation of state has to be used when thermal effects become important. The proposed numerical method however

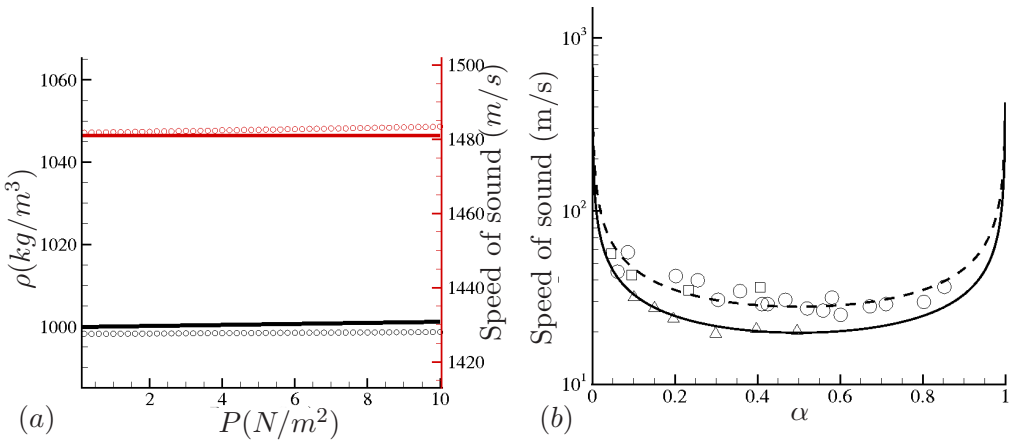

Figure 2.1: (a) Comparison of density and speed of sound in water with NIST data, ∘ : NIST data, —— : Present. (b) Comparison of speed of sound in water-air mixture to experiment, ▫ : Henry et al. [2], ∘ : Semenov and Kosterin [3], △ : Karplus [4], —— : Present (0.1 MPa), ---- : Present (0.2 MPa).

can be applied to more complicated equations of state for water; e.g. the Tait equation of state. Since internal energy is a function of both pressure and temperature, we need to obtain these variables using Eq. (2.5) and Eq. (2.6). Solving these two equations simultaneously yields the quadratic equation $ap^2 + bp + c = 0$, where

$$\begin{aligned} a &= C_{vm}, \\ b &= C_{vm}P_c + (1-Y)P_cK_l - [(1-Y)K_l + YR_g]\rho e_s \text{ and} \\ c &= -YR_gP_c\rho e_s. \end{aligned} \tag{2.7}$$

The pressure is obtained as the positive root of this quadratic equation and temperature is then computed from either Eq. (2.5) or Eq. (2.6). The viscous stress σ_{ij} and heat flux Q_i are given by

$$\begin{aligned} \sigma_{ij} &= \mu\left(\frac{\partial u_i}{\partial x_j} + \frac{\partial u_j}{\partial x_i} - \frac{2}{3}\frac{\partial u_k}{\partial x_k}\delta_{ij}\right) \text{ and} \\ Q_i &= k\frac{\partial T}{\partial x_i}, \end{aligned} \tag{2.8}$$

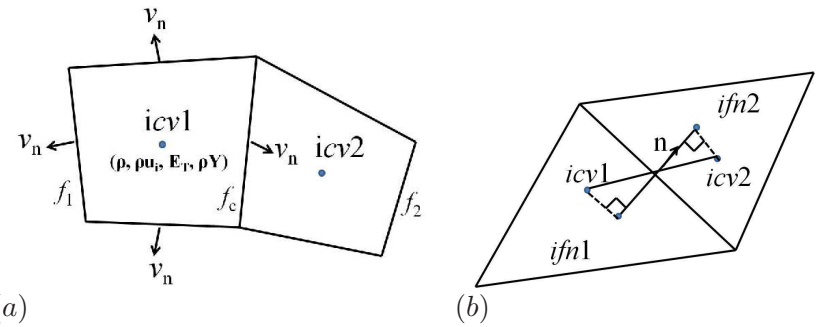

Figure 2.2: (a) Schematic of the collocated finite volume method. (b) Schematic for computation of face normal gradient for viscous terms.

where the mixture viscosity and mixture thermal conductivity are defined as

$$\begin{aligned} \mu &= \mu_l(1-\alpha)(1+2.5\alpha) + \mu_g\alpha \text{ and} \\ k &= k_l(1-\alpha) + k_g\alpha. \end{aligned} \tag{2.9}$$

To perform LES, Eqs. (2.3) are first Favre filtered spatially:

$$\begin{aligned} \frac{\partial \overline{\rho}}{\partial t} &= -\frac{\partial}{\partial x_k}\left(\overline{\rho}\tilde{u_k}\right), \\ \frac{\partial \overline{\rho}\tilde{u_i}}{\partial t} &= -\frac{\partial}{\partial x_k}\left(\overline{\rho}\tilde{u_i}\tilde{u_k} + \overline{p}\delta_{ik} - \tilde{\sigma}_{ik} - \tau_{ik}\right) \\ \frac{\partial \overline{\rho}\tilde{Y}}{\partial t} &= -\frac{\partial}{\partial x_k}\left(\overline{\rho}\tilde{Y}\tilde{u_k} - t_k\right) + \tilde{S}_e - \tilde{S}_c, \\ \frac{\partial \overline{\rho}\tilde{e}_s}{\partial t} &= -\frac{\partial}{\partial x_k}\left(\overline{\rho}\tilde{e_s}\tilde{u_k} - \tilde{Q}_k - q_k\right) - \overline{p}\frac{\partial \tilde{u_k}}{\partial x_k} + \tilde{\sigma_{ik}}\frac{\partial \tilde{u_i}}{\partial x_k}. \end{aligned} \tag{2.10}$$

Here, the tilde quantities are Favre averaged quantities and τ_{ik}, q_k and t_k are subgrid scale (SGS) terms namely: SGS stress, SGS heat flux and SGS scalar flux. These terms are modeled using the Dynamic Smagorinsky model (DSM) [38] :

$$
\begin{aligned}
\tau_{ij} - \frac{\delta_{ij}}{3}\tau_{kk} &= -2C_S(\mathbf{x},t)\overline{\rho}\Delta^2 \left|\tilde{S}\right| \widetilde{S^*_{ij}}, \\
\tau_{kk} &= 2C_I(\mathbf{x},t)\overline{\rho}\Delta^2 \left|\tilde{S}\right|^2, \\
q_i &= -\overline{\rho}\frac{C_S(\mathbf{x},t)\Delta^2 \left|\tilde{S}\right|}{Pr_T}\frac{\partial \overline{T}}{\partial x_i}, \\
t_i &= -\overline{\rho}\frac{C_S(\mathbf{x},t)\Delta^2 \left|\tilde{S}\right|}{Sc_T}\frac{\partial \overline{Y}}{\partial x_i},
\end{aligned}
\tag{2.11}
$$

where $|S| = \sqrt{2S_{ij}S_{ij}}$ and $S^*_{ij} = S_{ij} - 1/3S_{kk}\delta_{ij}$. The model coefficients C_s, C_I, Pr_T and Sc_T are determined using the Germano identity. For example,

$$
\begin{aligned}
C_S\Delta^2 &= \frac{1}{2}\frac{\left\langle L^*_{ij}M^*_{ij}\right\rangle}{\left\langle M^*_{ij}M^*_{ij}\right\rangle}, \\
L^*_{ij} &= \left(\frac{\widehat{\overline{\rho u_i}\cdot\overline{\rho u_j}}}{\overline{\rho}}\right) - \frac{\widehat{\overline{\rho u_i}}\cdot\widehat{\overline{\rho u_j}}}{\widehat{\overline{\rho}}}, \\
M^*_{ij} &= \overline{\rho}\,\widehat{\left|\tilde{S}\right|\widetilde{S^*_{ij}}} - \widehat{\overline{\rho}}\left(\frac{\widehat{\Delta}}{\Delta}\right)^2 \widehat{\left|\tilde{S}\right|}\widehat{\widetilde{S^*_{ij}}},
\end{aligned}
\tag{2.12}
$$

where, $\langle\cdot\rangle$ denotes spatial average over homogeneous direction(s) and the caret denotes test filtering. Test filtering is defined by the linear interpolation from face values of a control volume, which is again the interpolation from two adjacent cell center values [38]:

$$
\widehat{\phi} = \frac{1}{N_{\text{face}}}\sum_{\text{no of face}}\phi_f = \frac{1}{2N_{\text{face}}}\sum_{\text{no of face}}(\phi_{icv1} + \phi_{icv2}),
\tag{2.13}
$$

where N_{face} is the number of faces for a given control volume.

2.2.1 Speed of sound

The speed of sound in a liquid-gas mixture is obtained using the equation of state and Gibbs equation and is given by

$$\begin{aligned} a^2 &= \frac{C_1 T}{C_0 - \dfrac{C_1}{C_{pm}}}, \text{where} \\ C_0 &= 1 - (1-Y)\rho K_l T \frac{P_c}{(p+P_c)^2}, \\ C_1 &= R_g Y - K_l (1-Y) \frac{p}{p+P_c} \text{ and} \\ C_{pm} &= Y C_{pg} + (1-Y) C_{pl}. \end{aligned} \tag{2.14}$$

The change in speed of sound with gas volume fraction at given temperature and pressure obtained using the above relation, is compared to experimental results [2–4] in Figure 2.1(b). This sound speed is obtained assuming that there is no mass transfer between the phases and hence is the non-equilibrium sound speed. Note the good agreement with experiments; also the effect of gas volume fraction in changing the acoustic characteristics of water is evident. Note that the sound speed in the mixture ranges from 1480 m/s for pure water to 30 m/s for certain values of gas volume fraction.

2.2.2 Cavitation source terms

For cavitating flows, S_e and S_c are source terms for evaporation of water and condensation of vapor and are given by

$$\begin{aligned} S_e &= C_e \alpha^2 (1-\alpha)^2 \frac{\rho_l}{\rho_g} \frac{\max((p_v - p), 0)}{\sqrt{2\pi R_g T}}, \\ S_c &= C_c \alpha^2 (1-\alpha)^2 \frac{\max((p - p_v), 0)}{\sqrt{2\pi R_g T}}, \end{aligned} \tag{2.15}$$

where α is the volume fraction of vapor and p_v is the vapor pressure. C_e and C_c are empirical constants. Saito et al. [20] have shown that the source terms are not very sensitive to the values of these empirical constants and arrive at an optimum value of

0.1 for both the constants. Vapor pressure is related to temperature by

$$p_v = p_k \exp\left((1 - \frac{T_k}{T})(a + (b - cT)(T - d)^2)\right), \tag{2.16}$$

where p_k = 22.130 MPa, T_k = 647.31 K, a = 7.21, b = 1.152 x 10^{-5}, c = -4.787 x 10^{-9}, d = 483.16.

2.3 Numerical method

The numerical method uses a novel predictor corrector approach. In the predictor step, Eqs. (2.3) are discretized using a collocated, cell-centered finite volume method. Figure 2.2(a) illustrates the storage of variables and the notation used. The solution is first advanced using a non-dissipative predictor step. The characteristic based filter is then applied as a corrector. The road-map of the development work is shown in Figure 2.3.

2.3.1 Predictor step

A predicted value is first obtained by solving Eqs. (2.3) using a symmetric and non-dissipative scheme. The convective fluxes at the face are estimated using a symmetric average with a gradient term using Taylor series expansion to obtain

$$\phi_{f_c} = \frac{\phi_{icv1} + \phi_{icv2}}{2} + \frac{1}{2}\left(\nabla\phi|_{icv1} \cdot \Delta\mathbf{x}^{icv1} + \nabla\phi|_{icv2} \cdot \Delta\mathbf{x}^{icv2}\right), \tag{2.17}$$

where $\Delta\mathbf{x}^{icv1} = \mathbf{x}_{f_c} - \mathbf{x}_{icv1}$, and $\nabla\phi|_{icv1}$denotes the gradient defined at $icv1$. The viscous term is split into two parts, $\sigma_{ij} = \sigma^1_{ij} + \sigma^2_{ij}$, where $\sigma^1_{ij} = \frac{\mu}{Re}\frac{\partial u_i}{\partial x_j}$ and $\sigma^2_{ij} = \frac{\mu}{Re}\left(\frac{\partial u_j}{\partial x_i} - \frac{2}{3}\frac{\partial u_k}{\partial x_k}\delta_{ij}\right)$. σ^2_{ij} can be interpreted as a 'compressible' contribution, since it vanishes in the incompressible limit. The 'incompressible' component σ^1_{ij} is computed by

$$\frac{1}{V_{\text{cv}}}\sum_{\text{faces}}\left(\frac{\mu}{Re}\right)_f \left.\frac{\partial u_i}{\partial x_j}\right|_f n_j A_f = \frac{1}{V_{\text{cv}}}\sum_{\text{faces}}\left(\frac{\mu}{Re}\right)_f \left.\frac{\partial u_i}{\partial n}\right|_f A_f. \tag{2.18}$$

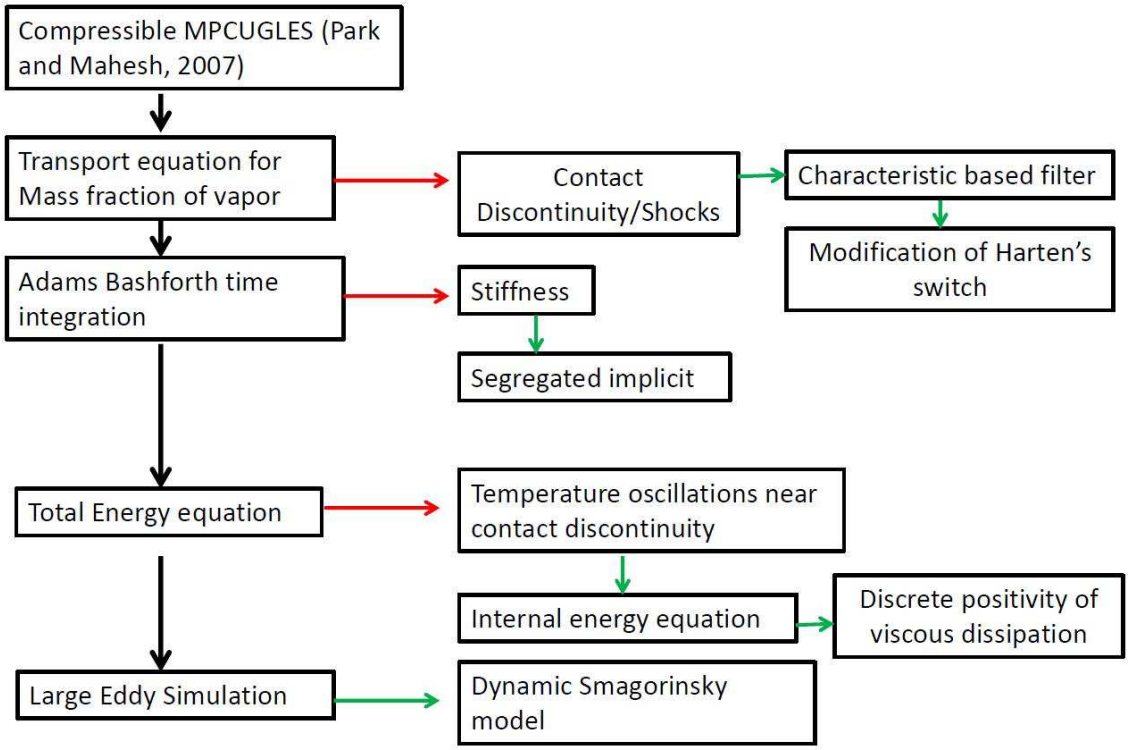

Figure 2.3: Road-map of development.

Here, the normal gradient at the face is computed by

$$\frac{\partial \phi}{\partial n} = \frac{\phi_{ifn2} - \phi_{ifn1}}{d_f}, \tag{2.19}$$

where $ifn1$ ($ifn2$) is the projection of $icv1$ ($icv2$) onto the extension of normal vector $\mathbf{n}$ and d_f is the distance between $ifn1$ and $ifn2$ as illustrated in Figure 2.2(b). ϕ_{ifn1} is given by

$$\phi_{ifn1} = \phi_{icv1} + \nabla\phi|_{icv1} \cdot (\mathbf{x}_{ifn1} - \mathbf{x}_{icv1}), \tag{2.20}$$

where the linear least-square method is used to determine the gradient $\nabla\phi$ at $icv1$. Viscosity at the cell face is obtained using Eq. (2.17) and a least square reconstruction. Thus, the incompressible part corresponds to a compact-stencil method. $\sigma^2_{ij,f}$ is constructed by the interpolation of $\sigma^2_{ij}\Big|_{icv1}$ and $\sigma^2_{ij}\Big|_{icv2}$ using Eq. (2.17).

2.3.2 Discrete positivity of viscous dissipation

The viscous term in the internal energy equation corresponds to the viscous dissipation term and by the second law of thermodynamics, should always remain positive. This term is therefore re-written to discretely ensure positivity. Note that

$$\sigma_{ik}\frac{\partial u_i}{\partial x_k} = \begin{pmatrix} \frac{4\partial u}{3\partial x} & \frac{\partial u}{\partial y} + \frac{\partial v}{\partial x} & \frac{\partial u}{\partial z} + \frac{\partial w}{\partial x} \\ \frac{\partial u}{\partial y} + \frac{\partial v}{\partial x} & \frac{4\partial v}{3\partial y} & \frac{\partial v}{\partial z} + \frac{\partial w}{\partial y} \\ \frac{\partial u}{\partial z} + \frac{\partial w}{\partial x} & \frac{\partial v}{\partial z} + \frac{\partial w}{\partial y} & \frac{4\partial w}{3\partial z} \end{pmatrix} \begin{pmatrix} \frac{\partial u}{\partial x} & \frac{\partial u}{\partial y} & \frac{\partial u}{\partial z} \\ \frac{\partial v}{\partial x} & \frac{\partial v}{\partial y} & \frac{\partial v}{\partial z} \\ \frac{\partial w}{\partial x} & \frac{\partial w}{\partial y} & \frac{\partial w}{\partial z} \end{pmatrix}$$

can be re-written as

$$\sigma_{ik}\frac{\partial u_i}{\partial x_k} = \frac{4}{3}\left[\left(\frac{\partial u}{\partial x}\right)^2 + \left(\frac{\partial v}{\partial y}\right)^2 + \left(\frac{\partial w}{\partial z}\right)^2\right] + \left(\frac{\partial u}{\partial y} + \frac{\partial v}{\partial x}\right)^2 + \left(\frac{\partial u}{\partial z} + \frac{\partial w}{\partial x}\right)^2 + \left(\frac{\partial v}{\partial z} + \frac{\partial w}{\partial y}\right)^2. \tag{2.21}$$

This sum of squares is strictly positive and hence viscous dissipation remains discretely positive at all times. This operation is also cheaper than forming the tensors and

computing their scalar product.

2.3.3 Time advancement

Two time advancement schemes are implemented: a second-order explicit Adams-Bashforth scheme and a second order segregated implicit Crank-Nicholson scheme. For the Adams-Bashforth scheme,

$$q_j^{n+1} = q_j^n + \frac{\Delta t}{2}\left[3\mathrm{rhs}_j(\mathbf{q}^n) - \mathrm{rhs}_j(\mathbf{q}^{n-1})\right], \tag{2.22}$$

where rhs_j denotes j^{th} component of the right hand side of the governing equation, and the superscript n denotes the n^{th} time step. In the segregated implicit method, the governing equations are discretized using the Crank-Nicholson method. For example, the discrete continuity equation is

$$\frac{\rho_{cv}^{n+1} - \rho_{cv}^n}{\Delta t} V_{cv} = -\frac{1}{2}\sum_{\text{faces}} (\rho V_N)_f^n A_f - \frac{1}{2}\sum_{\text{faces}} (\rho V_N)_f^{n+1} A_f. \tag{2.23}$$

The face value can be written as the sum of the neighboring control volume values as $\rho_f = \dfrac{\rho_{cv} + \rho_{nbr}}{2}$. On rearrangement,

$$\rho_{cv}^{n+1}\left[1 + \frac{\Delta t}{4V_{cv}}\sum_{\text{faces}} V_{N_f}^{n+1,k} A_f\right] + \left[\frac{\Delta t}{4V_{cv}}\sum_{\text{faces}} \rho_{nbr}^{n+1} V_{N_f}^{n+1,k} A_f\right] = -\left[\frac{\Delta t}{2V_{cv}}\sum_{\text{faces}} \rho_f^n V_{N_f}^n A_f\right]. \tag{2.24}$$

The above equation is solved iteratively to obtain an estimate for $\rho^{n+1,k}$ for all the control volumes, where k is the outer loop variable. The other equations are solved similarly to obtain $\rho u_i^{n+1,k}$, $\rho e_s^{n+1,k}$ and $\rho Y^{n+1,k}$ for all the control volumes. This step is repeated until the difference between $(k+1)^{\text{th}}$ time variables and k^{th} time variables becomes negligible, thus coupling the equations using an outer iteration. All results presented in this dissertation use explicit time advancement.

2.3.4 Corrector step : Characteristic-based Filter

The predictor step described in the previous section does not explicitly add dissipation and hence cannot capture discontinuities (both shocks and material discontinuities). An external discontinuity capturing mechanism is therefore provided. Yee et al. [37] developed a characteristic based filtering method for ideal gases on structured grids which was extended to ideal gases on unstructured grids by Park and Mahesh [38]. In this study, a characteristic based filtering method is developed for mixtures of fluids and non ideal gases on unstructured grids. Note that any time integration scheme can be used in the predictor step and it will not affect the implementation of the corrector step. Once a physical time step Δt is advanced to obtain the solution $\widehat{q}^{n+1}$ from q^n, the final solution q^{n+1} at $t + \Delta t$ is obtained from a corrector scheme

$$q_{cv}^{n+1} = \widehat{q}_{cv}^{n+1} - \frac{\Delta t}{V_{cv}} \sum_{\text{faces}} (F_f^* . n_f) A_f, \tag{2.25}$$

where F_f^* is the filter numerical flux of the following form

$$F_{fc}^* = \frac{1}{2} R_{fc} \Phi_{fc}^*. \tag{2.26}$$

Here R_{fc} is the right eigenvector vector at the face computed using Roe-average of the variables from left and right control volumes. The expression for the lth component of Φ^*, ϕ^{*l} is given by

$$\phi_{fc}^{*l} = k \theta_{fc}^l \phi_{fc}^l, \tag{2.27}$$

where k is an adjustable parameter. The value of k is problem dependent and its effect on the results is demonstrated in Section 3.3. θ_{fc} is the Harten's switch function given by

$$\begin{aligned}
\theta_{fc} &= \sqrt{0.5(\widehat{\theta}^2_{icv1} + \widehat{\theta}^2_{icv2})}, \\
\widehat{\theta}_{icv1} &= \frac{|\beta_{fc}| - |\beta_{f1}|}{|\beta_{fc}| + |\beta_{f1}|}, \\
\widehat{\theta}_{icv2} &= \frac{|\beta_{f2}| - |\beta_{fc}|}{|\beta_{f2}| + |\beta_{fc}|}.
\end{aligned} \tag{2.28}$$

Here, $\beta_f = R_f^{-1}(q_{icv2} - q_{icv1})$ is the difference between characteristic variables across the face. f_1 and f_2 in a structured grid are the face neighbors in the corresponding direction (i.e. in the direction of the face normal). This definition is not possible in an unstructured grid, hence the concept of most parallel faces was introduced in [38]. Figure 2.2(a) illustrates this concept. For ϕ^ℓ, the Harten-Yee TVD form is used as suggested by Yee et al. [37].

$$\begin{aligned}
\phi^\ell_{f_c} &= \frac{1}{2}\Psi\left(a^\ell_{f_c}\right)\left(g^\ell_{icv1} + g^\ell_{icv2}\right) - \Psi\left(a^\ell_{f_c} + \gamma^\ell_{f_c}\right)\beta^\ell_{f_c}, \\
\gamma^\ell_{f_c} &= \frac{1}{2}\frac{\Psi\left(a^\ell_{f_c}\right)\left(g^\ell_{icv2} - g^\ell_{icv1}\right)\beta^\ell_{f_c}}{\left(\beta^\ell_{f_c}\right)^2 + \epsilon},
\end{aligned} \tag{2.29}$$

where $\epsilon = 10^{-7}$ and $\Psi(z) = \sqrt{\delta + z^2}$. $\delta = 1/16$ is introduced for entropy fixing [37]. $a^\ell_{f_c}$ is the element of the jacobian matrix. For a structured grid, the value of the limiter function g_{icv} can be defined at the cell centers using the value of α at faces. Defining this in an unstructured grid will require interpolation. To avoid this, we define g at the faces. This is more natural because Eqs. (2.29) require only symmetric average $\frac{1}{2}\left(g_{icv1} + g_{icv2}\right)$ and difference $\frac{1}{2}\left(g_{icv2} - g_{icv1}\right)$ of g between the neighboring control volumes. Thus the expression of g is given by

$$\begin{aligned}
g^{+\ell}_{f_c} &\equiv \frac{1}{2}\left\{\text{minmod}\left(\beta^\ell_{f_1}, \beta^\ell_{f_c}\right) + \text{minmod}\left(\beta^\ell_{f_c}, \beta^\ell_{f_2}\right)\right\}, \\
g^{-\ell}_{f_c} &\equiv \frac{1}{2}\left\{\text{minmod}\left(\beta^\ell_{f_2}, \beta^\ell_{f_c}\right) - \text{minmod}\left(\beta^\ell_{f_1}, \beta^\ell_{f_c}\right)\right\}.
\end{aligned} \tag{2.30}$$

The expressions for $\phi^{\ell}_{f_c}$ and $\gamma^{\ell}_{f_c}$ can now be written as

$$\begin{aligned} \phi^{\ell}_{f_c} &= \Psi\left(a^{\ell}_{f_c}\right) g^{+\ell}_{f_c} - \Psi\left(a^{\ell}_{f_c} + \gamma^{\ell}_{f_c}\right) \beta^{\ell}_{f_c}, \\ \gamma^{\ell}_{f_c} &= \frac{\Psi\left(a^{\ell}_{f_c}\right) g^{-\ell}_{f_c} \beta^{\ell}_{f_c}}{\left(\beta^{\ell}_{f_c}\right)^2 + \epsilon}, \end{aligned} \tag{2.31}$$

This approach avoids any interpolation between cell center and faces and hence, on Cartesian grids will be equivalent to the expression proposed for structured grids by Yee et al. [37]. In order to determine the eigenvectors of the system, the flux Jacobian matrix needs to be computed. First the expression for pressure needs to be expressed in terms of solution variables $q_j = (\rho, \rho u_i, \rho E_T, \rho Y)$. Note that total energy is used here even though internal energy is solved in the predictor step, since jump conditions need to be obtained for conservative variables. Eq. (2.7), when expressed in terms of the solution variables q becomes

$$\begin{aligned} a &= C_{vl}(q_1 - q_6) + C_{vg} q_6, \\ b &= C_{pl} P_c (q_1 - q_6) + C_{vg} P_c q_6 - \\ &\quad [(q_1 - q_6) K_l + q_6 R_g][q_5 - 0.5 \frac{{q_2}^2 + {q_3}^2 + {q_4}^2}{q_1}] \text{ and} \\ c &= -q_6 R_g P_c [q_5 - 0.5 \frac{{q_2}^2 + {q_3}^2 + {q_4}^2}{q_1}]. \end{aligned} \tag{2.32}$$

$\dfrac{\partial p}{\partial q_j}$ is then obtained as

$$\frac{\partial p}{\partial q_j} = -\frac{[p^2 \dfrac{\partial a}{\partial q_j} + p \dfrac{\partial b}{\partial q_j} + \dfrac{\partial c}{\partial q_j}]}{2ap + b}. \tag{2.33}$$

The flux Jacobian matrix thus obtained, denoted by A_{ij} is given in Appendix A. Once the flux Jacobian matrix is obtained, the eigenvector vector matrix R_{ij} and its inverse R^{-1}_{ij} given in Appendix A can be evaluated.

Modification of Harten's switch

Park and Mahesh [38] showed that for a single phase flow, the original Harten's switch θ_{fc} proposed by Yee *et al.* is excessively dissipative. They make use of a temporally decaying isotropic turbulence problem to show that the original Harten's switch affects resolved turbulence, and propose a modified localization term based on divergence and vorticity [42]. In order to evaluate the performance of this term and the original Harten's switch in multiphase flows, we perform LES of decaying isotropic turbulence in a mixture of water and vapor. The simulation is performed on a coarse grid of 32^3 volumes with an initial Taylor micro scale Reynolds number $Re_\lambda = u_{rms}\lambda/\nu = 68.7$. The initial spectrum is given by

$$E(k) = 16\sqrt{\frac{2}{\pi}}\frac{u_0^2}{k_0}\left(\frac{k}{k_0}\right)^4 \exp\left(-2k^2/k_0^2\right), \tag{2.34}$$

and the initial fluctuation Mach number is 0.001. The pressure fluctuations are such that the flow does not cavitate. Even in the absence of any discontinuities, the Harten's switch θ_{f_c} is found to be dissipative thereby affecting the resolved turbulence as shown in Figure 2.4. Hence θ_{f_c} is modified using a sensor based on Ducros et al. [42] to prevent excessive dissipation.

$$\begin{aligned} \theta_{f_c} &= \theta_{f_c}\theta^\star_{f_c}, \\ \theta^\star_{f_c} &= \frac{1}{2}\left(\theta^\star_{icv1} + \theta^\star_{icv2}\right), \\ \theta^\star_{icv1} &= \frac{(\nabla\cdot\mathbf{u})^2_{icv1}}{(\nabla\cdot\mathbf{u})^2_{icv1} + \Omega^2_{icv1} + \epsilon}. \end{aligned} \tag{2.35}$$

Here Ω is the vorticity magnitude and $\epsilon = 10^{-7}$ is a small positive value. The modified term, henceforth called as modified single phase switch, limits dissipation away from discontinuities. This is clearly seen in Figure 2.4 which shows kinetic energy (q) decay and the radial energy spectrum. t_e is the eddy turnover time.

However, even this modification causes problems in a cavitating flow. Consider an inviscid cavitating vortex on a square domain of dimensions 100R x 100R. The initial

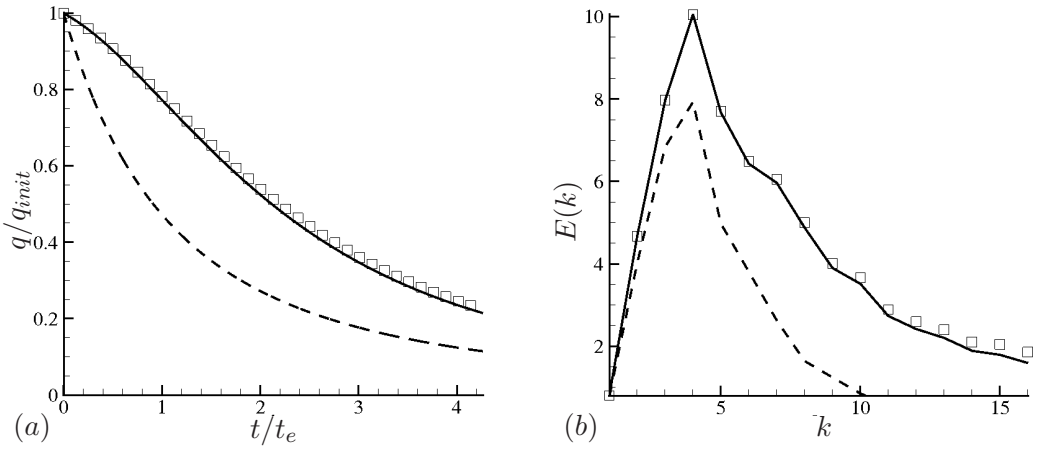

Figure 2.4: (a) Comparison of temporal decay of kinetic energy obtained using original Harten's switch and modified singlephase switch to results obtained using no shock capturing. (b) Radial energy spectrum at $t/t_e = 4.0$ obtained using original Harten's switch and modified singlephase switch compared to results obtained using no shock capturing. ▫ : No shock capturing, ---- : Harten's switch, —— : Modified switch.

velocity field is

$$\begin{aligned} u &= -\frac{C(y-y_c)}{R^2}\exp(-r^2/2) \text{ and} \\ v &= \frac{C(x-x_c)}{R^2}\exp(-r^2/2). \end{aligned} \tag{2.36}$$

Here $r^2 = \left[(x-x_c)^2 + (y-y_c)^2\right]/R^2$ and $R = 1$, $C = 5.0$, $x_c = y_c = 50R$. Constant density, pressure and temperature are specified initially. As the solution evolves, pressure in the center of the vortex drops below vapor pressure and the flow cavitates. As the vortex cavitates, the value of the modified singlephase switch becomes very small because of the large vorticity there. Hence numerical oscillations are encountered as shown in Figure 2.5(a). Figure 2.5(c) shows the variation of v-velocity and the modified singlephase switch along the $\theta = 0$ line. Note the oscillation in v-velocity and the very small value of the switch at the corresponding location. This oscillation increases with time and causes the solution to become unstable. As a remedy, an additional term is added to the modified single phase switch. This additional term prevents the switch from reaching very small values inside the cavitating vortex. Note that the additional

term automatically goes to zero in single phase regions and hence termed as modified multiphase switch. Its effect is clearly seen in Figure 2.5(b) in terms of an oscillation-free solution. Figure 2.5(d) shows that the proposed modification prevents the switch from reaching very small values inside the vortex. When applied to the turbulent problem discussed above, it yields identical results to the form proposed by Park and Mahesh [38].

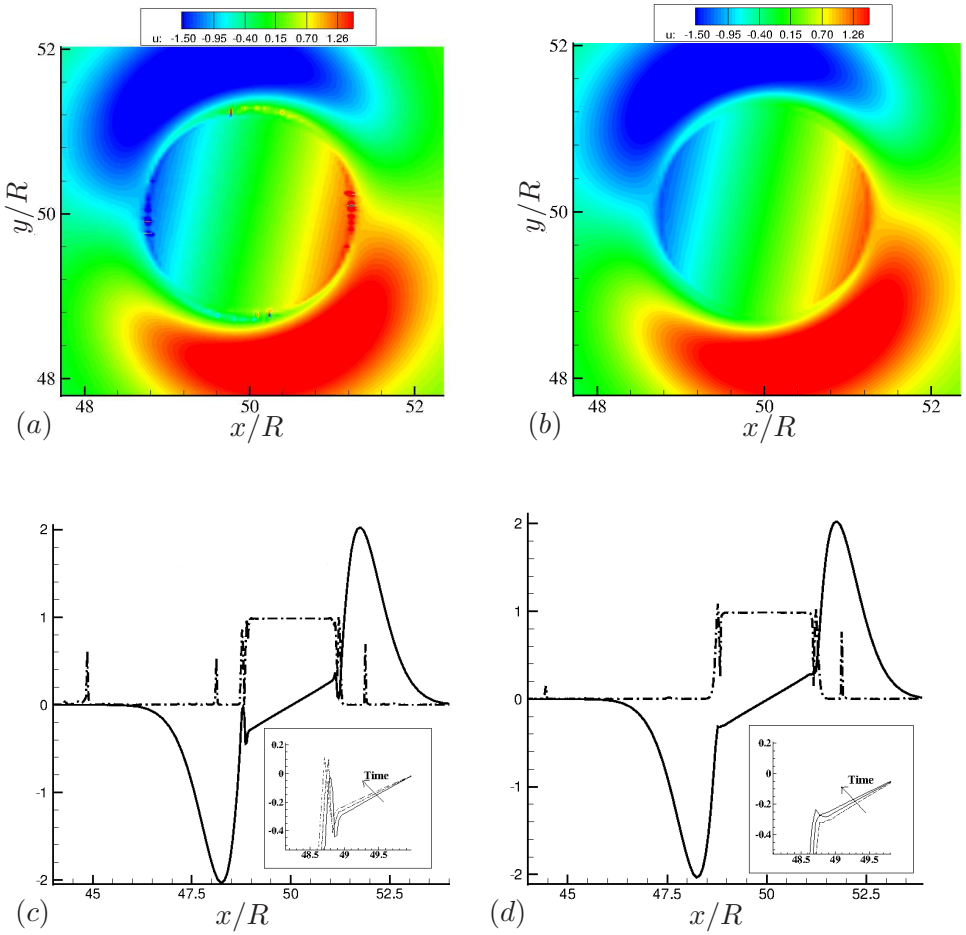

Figure 2.5: (a) and (b) Streamwise velocity contours for modified single phase and multiphase switch respectively. (c) Variation of modified singlephase switch and v-velocity along the $\theta = 0$ line. (d) Variation of modified multiphase switch and v-velocity along the $\theta = 0$ line. —— : v-velocity, ---- : Switch.

Chapter 3

Validation

3.1 Introduction

We evaluate the proposed algorithm for a variety of flows [43, 44]. In Section 3.2, a multiphase shock tube problem is discussed. This problem evaluates the accuracy of the shock capturing scheme in computing the jump conditions. In Sections 3.3 and 3.4, one dimensional cavitating problems are discussed. Finally in Section 3.5 and Section 3.6, the algorithm is validated for turbulent cavitating flows. Validation results for the wedge are presented in Chapter 5 along with a discussion of sheet to cloud cavitation.

3.2 Multiphase non cavitating shock tube

A two phase shock tube with water and compressed air [45, 46] is simulated. We use this problem to demonstrate the advantage of the internal energy equation over the total energy equation in the predictor step. The driver section contains liquid water at high pressure, the driven section contains compressed air at lower pressure and the interface is present at $x/L = 0.7$ initially. The problem is stiff; the density and pressure differ by ratios of 20 and 10^4 respectively across the discontinuities. The computational domain is discretized uniformly using 1000 volumes and a time step of $1{\times}10^{-8}$s is used. The

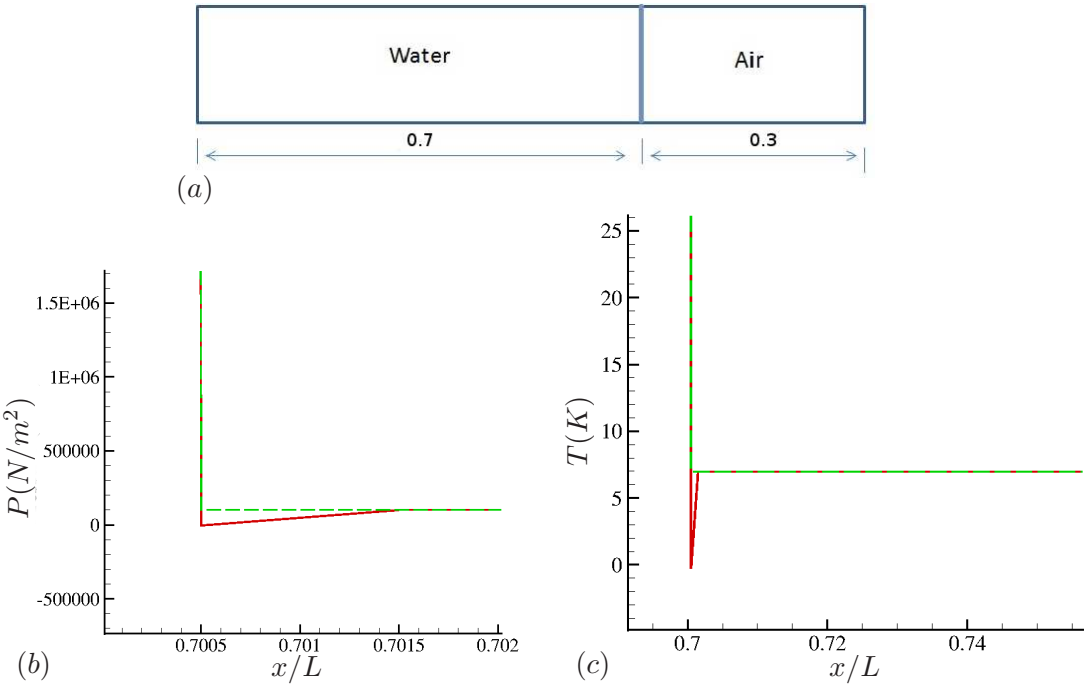

Figure 3.1: (a) Schematic for air-water shock tube. (b) Variation of pressure after the first time step. (c) Variation of temperature after the first time step. (—) : Total energy form, (- - -) : Internal energy form.

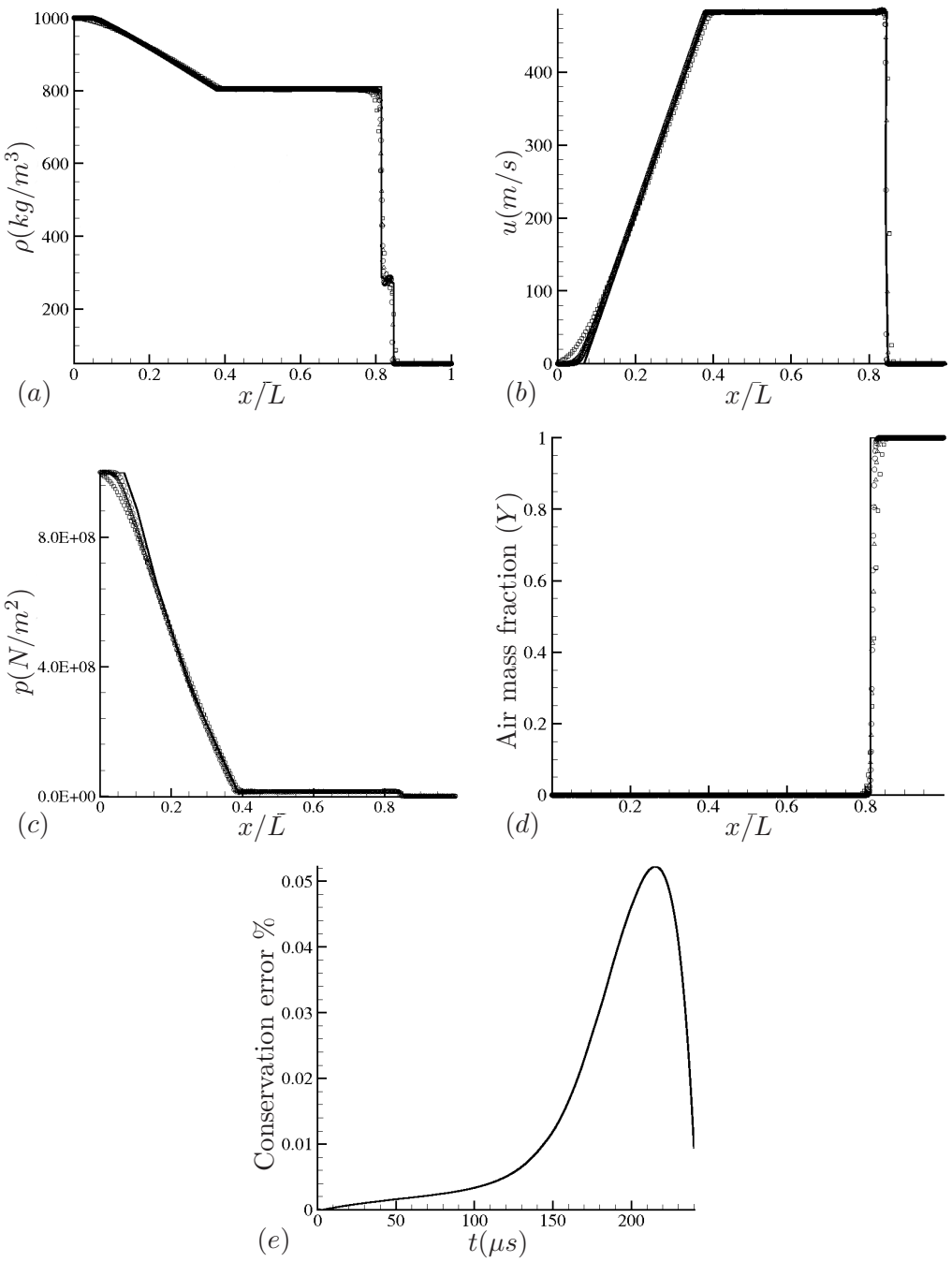

Figure 3.2: Comparison of numerical and analytical results for (a) density, (b) velocity, (c) pressure and (d) mass fraction of air, $\circ$: 1000 cells, $\triangle$: 500 cells, $\square$: 200 cells, —— : Analytical. (e) Conservation error percentage as a function of time.

initial conditions are given by

$$\begin{aligned} Q &= [\rho, u, p, \gamma, Y], \\ Q_W &= [1000, 0, 1.5.10^9, 4.4, 0.0], \\ Q_A &= [50, 0, 1.0.10^5, 1.4, 1.0]. \end{aligned} \tag{3.1}$$

Figure 3.1(a) shows a schematic of the problem and Figures 3.1(b) and (c) show the temperature and pressure obtained at the material discontinuity at the end of the predictor step of the very first iteration. It clearly shows that internal energy equation is able to produce an oscillation-free solution while the total energy equation does not, for the same time step. This is because a primitive variable formulation is less prone to aliasing errors. Consider the pressure term in the total energy equation. This term $\frac{\partial(pu_j)}{\partial x_j}$ has a product inside the derivative and associated aliasing as opposed to the term $p\frac{\partial u_j}{\partial x_j}$ in the internal energy equation. Also a spatial derivative of a linear term (as in the internal energy equation) will be more accurate than that of a quadratic product (as in the total energy equation), due to its lower spatial order. Further, Karni [47] has demonstrated the effectiveness of using primitive variables in suppressing the pressure oscillations across a material discontinuity. Hence solving for internal energy which is a primitive variable helps in reducing these errors. However conservation errors will be large if a primitive variable is used to compute jump conditions. Hence the corrector step which computes the jump conditions uses total energy which is obtained at the end of the predictor step using Eq. (2.5). Figure 3.2 shows the comparison between numerical and exact solution at 240 μs. Three different grids are used : 200, 500 and 1000 volumes. The solutions for all three grids agree with the analytical results; improvement in accuracy with grid refinement can also be observed. The shock wave initially at $x/L = 0.7$ on interaction with the contact discontinuity, reflects as an expansion wave which travels in water. Figure 3.2(e) shows that the usage of internal energy equation in the predictor step does not cause any significant conservation errors. The maximum conservative error obtained as $\frac{|\sum_{\mathrm{V}} E_T - \sum_{\mathrm{V}} E_{Tinitial}|}{\sum_{\mathrm{V}} E_{Tinitial}}$ is found to be less than 1% for the finest grid.

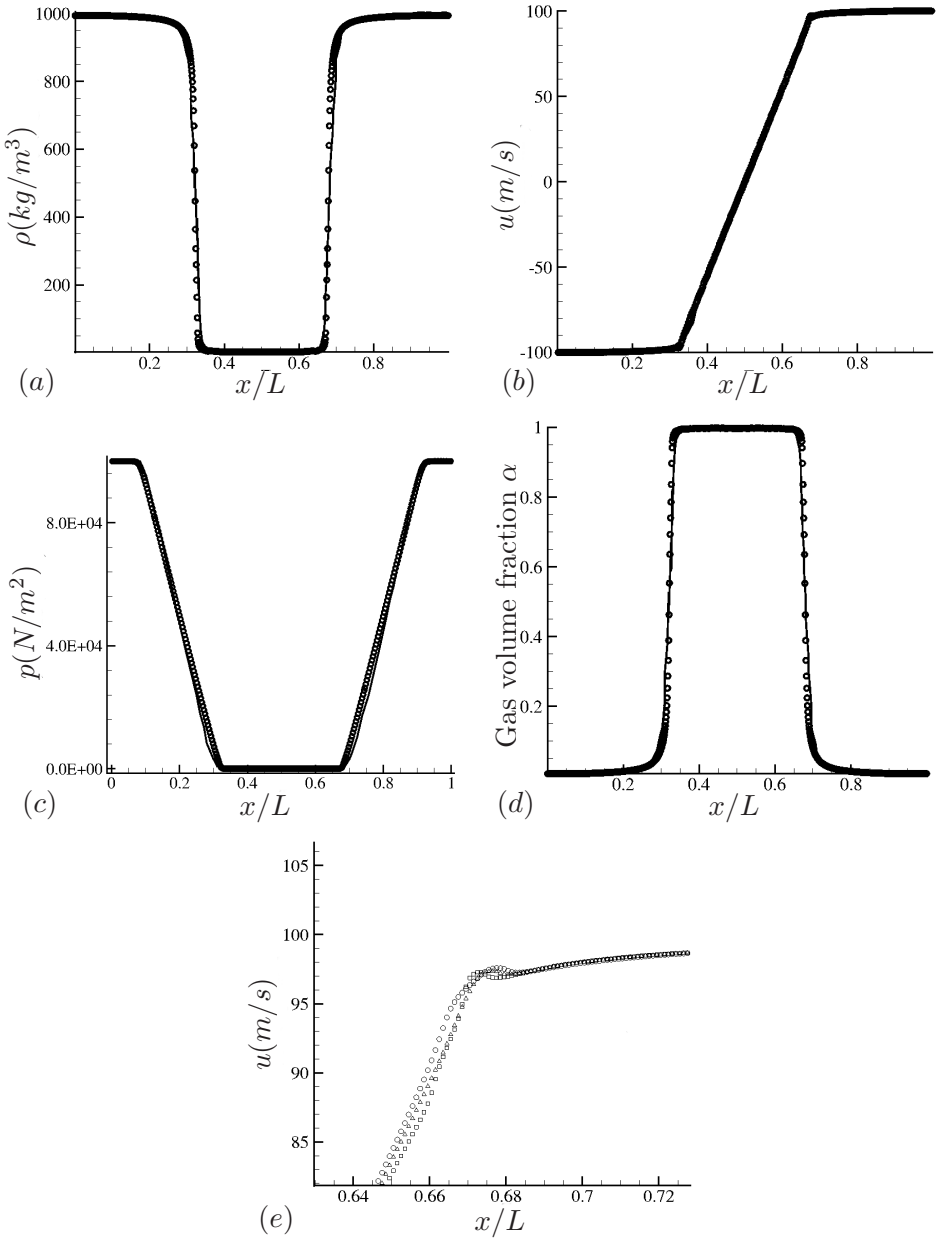

Figure 3.3: Comparison of present numerical results and numerical results of Saurel and Lemetayer [5] for (a) density, (b) velocity, (c) pressure and (d) volume fraction of vapor, $\circ$: Present, —— : Saurel and Lemetayer [5]. (e) Effect of k on velocity near a discontinuity, $\square$: $k-2.0$, $\triangle$: $k-4.0$, $\circ$: $k-8.0$.

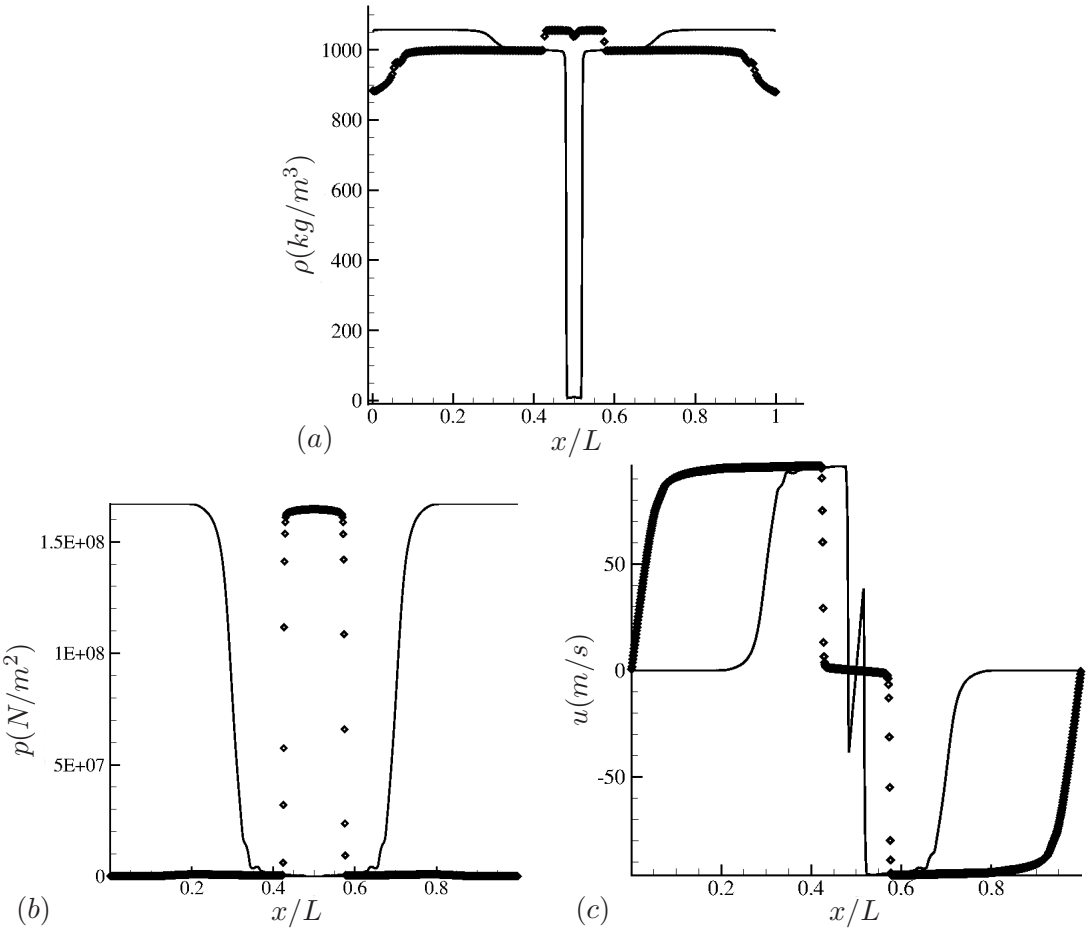

Figure 3.4: Comparison of quantities before and after bubble collapse. (a) density, (b) pressure and (c) velocity, —— : Before collapse, $\diamond$: After collapse.

3.3 One dimensional cavitating tube

This test problem involves a one dimensional tube consisting of water initially at atmospheric pressure and two streams moving away from the center at 100 m/s. The computational domain is discretized uniformly using 1000 volumes and a time step of 1×10^{-6}s is used. This problem has been previously investigated by many authors [5, 19, 48]. We compare our results with the results obtained using a multi fluid approach by Saurel and Lemetayer [5] in Figure 3.3. The expansion at the center causes a vapor bubble to be produced as soon as the pressure reaches vapor pressure. Thus two interfaces are created dynamically due to the rarefaction waves. The mixture density, pressure, velocity and vapor volume fraction at the end of 1860μs are compared with numerical results from Saurel and Lemetayer [5] and the results agree very well with each other. Further, the effect of k the adjustable parameter is evaluated and seen to be small. The velocity profile obtained using three different values of k (2,4 and 8) is magnified near a discontinuity and plotted in Figure 3.3(e). For lower values of k, small oscillations are observed which gets smoothed out at higher values. Apart from this, no other significant differences are observed.

3.4 One dimensional reflecting-cavitating tube

This case is similar to the previous problem but with the ends of the tube closed instantaneously at $t = 0$. This causes shock waves at the ends which propagate towards the center in addition to the rarefaction wave moving away from the center. This problem is used to demonstrate shock-bubble interaction and robustness of the method in handling bubble collapse. The computational domain is discretized uniformly using 1000 volumes and a time step of 1×10^{-8}s is used. The initial conditions are identical to the previous problem. Liu et al. [19] have studied this problem although with a different equation of state. The end walls act as reflecting boundaries causing a shock at time $t = 0$ and a cavitation bubble is formed at the center due to the expansion. The shock wave and the rarefaction wave meet as they travel in opposite directions and after interaction continue

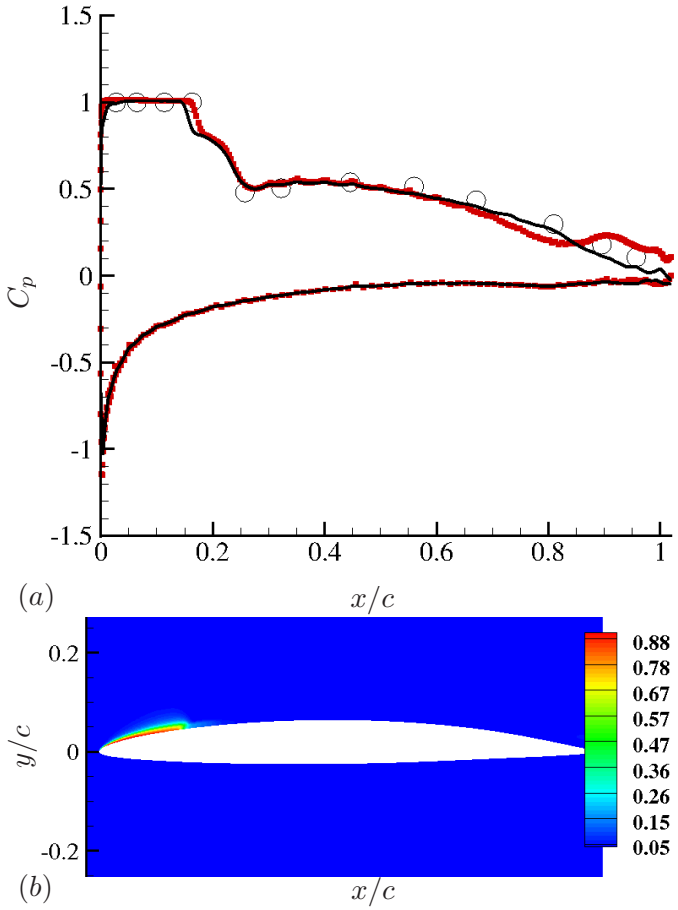

Figure 3.5: (a) Comparison of pressure co-efficient (C_p) distribution, ∘ : Shen and Dimotakis [6], □ : RANS, —— : LES, (b) Mean void fraction contour showing a partial sheet cavity.

to travel with a mitigated strength. Figure 3.4 shows two instances of time, one before vapor bubble collapse and one after collapse. Before collapse, the vapor bubble can be clearly seen at the center. The shock wave on interaction with the interface leads to a stronger discontinuity in velocity and pressure. After collapse, the center of the tube is filled with water which can be seen from the density curve. The condensation waves travel outward from the center which is also clearly seen in the pressure curve. The results agree qualitatively with Liu et al. [19], and also demonstrate that the numerical method is able to handle bubble collapse well.

3.5 Partial cavitation over a NACA hydrofoil

We consider a turbulent cavitating flow over a hydrofoil. Shen and Dimotakis [6] conducted experiments on this hydrofoil and our numerical results are compared against their experimental results. The hydrofoil section used is NACA 66 (mod) with a camber ratio of 0.02 and a thickness ratio of 0.09. The Reynolds number based on chord length c is 2 $\times 10^6$, the angle of attack is 4 degrees and the cavitation number $\sigma = \frac{p_\infty - p_v}{0.5\rho_\infty u_\infty^2}$ is 1.0. At this cavitation number, a leading edge cavity, also referred as partial sheet cavity/open cavity [49, 50] is observed in the experiment. A streamwise grid spacing of 0.0005c is used near the stagnation region to capture cavitation inception and the wall normal spacing is 0.0008c. We perform both LES and RANS and the results are compared to the experimental results. The three–dimensional grid for LES has 75 cells in the span–wise direction. For RANS, the governing equations Eqs. (2.3) are Reynolds averaged giving rise to Reynolds stress terms, which are modeled using the Spalart-Allmaras eddy viscosity model [51]. The details of Spalart-Allmaras model are given in Chapter B.

Figure 3.5 (a) shows the time averaged pressure coefficient distribution along the chord for both the suction and pressure sides. Both LES and RANS give reasonable agreement; the LES result however shows better agreement near the trailing edge when compared to RANS. This difference between RANS and LES can be understood from Figure 3.6 showing mean streamwise velocity contour. RANS predicts a larger separation bubble in the trailing edge when compared to LES and it is this discrepancy that causes the RANS result to deviate from the experimental result near the trailing edge.

As discussed in Chapter 2, localization of dissipation is essential to accurately simulate turbulent flows. To assess this effect, the filter flux $\frac{F^*_{fc}}{V_{cv}}$ is computed and plotted separately for both continuity and u-momentum equations alone for the purpose of illustration, where $F^*_{fc} = \frac{1}{2} R_{fc} \Phi^*_{fc}$. Figure 3.7 (a) clearly shows that the filter fluxes are active only near the cavity inception and cavity closure locations where the density gradient is maximum. Similar trends can be observed even in the u-momentum equation in Figure 3.7 (b). Further, small values of filter flux are seen in the cavitating vortices that

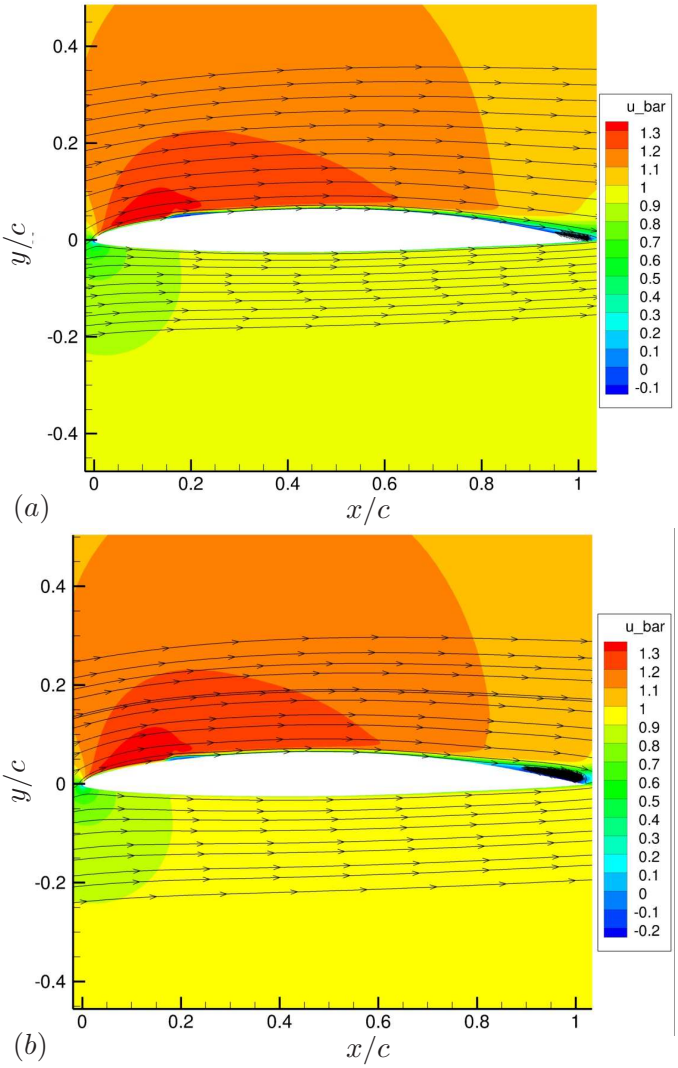

Figure 3.6: Mean streamwise velocity contours for (a) LES and (b) RANS.

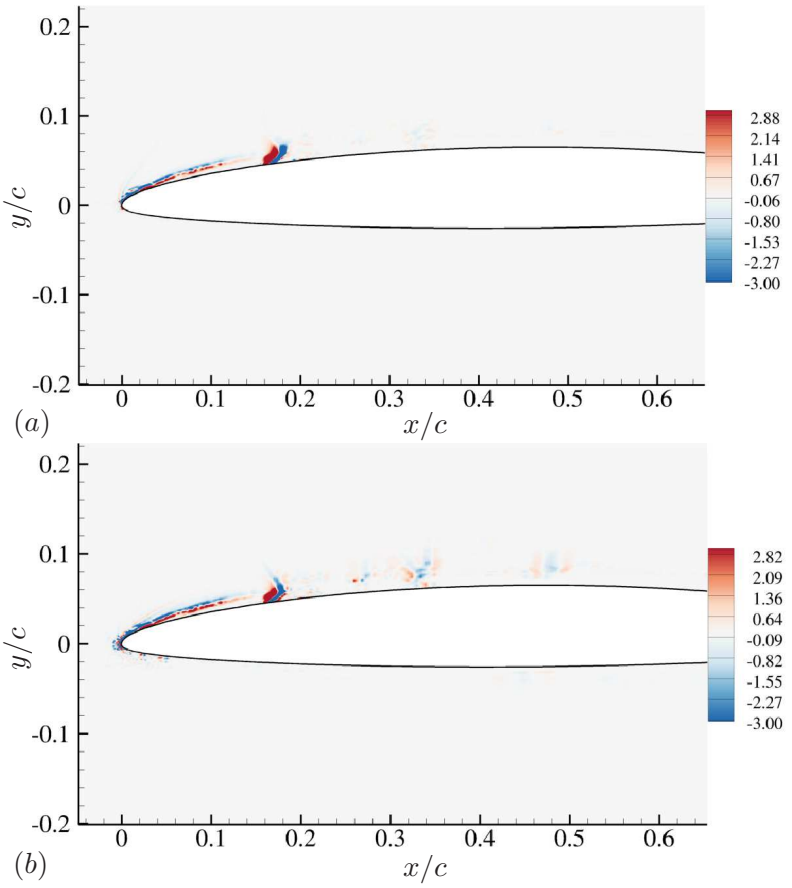

Figure 3.7: Instantaneous dissipative flux for (a) continuity equation, (b) u-momentum equation.

are shed from the cavity closure. This behavior shows that the dissipation is localized to the vicinity of discontinuities.

3.6 Cavitation over a hemispherical nose shaped body

Next, we consider partial cavitation over a hemispherical nose shaped bluff body. We compare our LES results to the experimental results of Rouse and McNown [7]. The diameter of the hemisphere is D and the length of the cylindrical body is $50D$. The extent of the domain is $50D$ in all directions. The Reynolds number based on the diameter of the hemisphere and freestream velocity is $Re_D = 1.36 \times 10^5$ and the cavitation

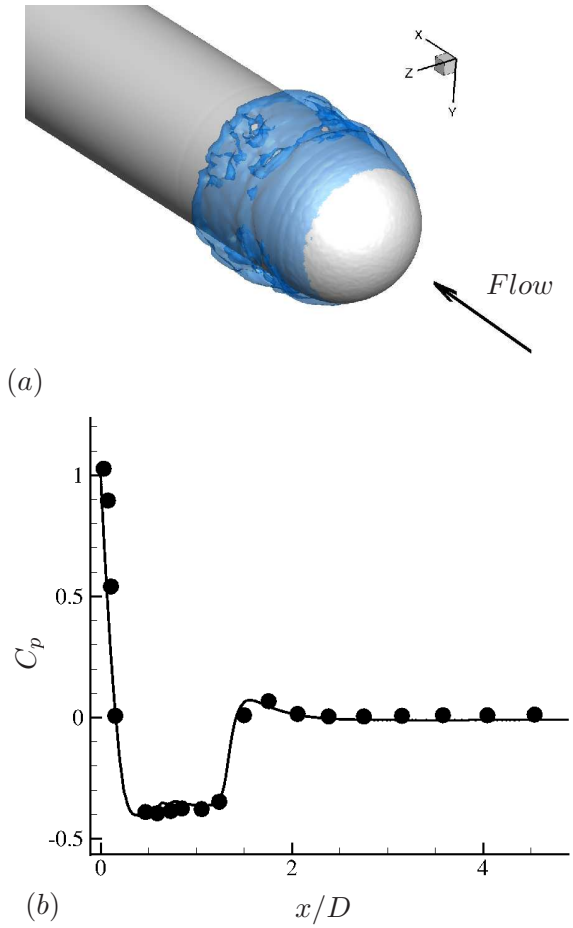

Figure 3.8: (a) Instantaneous isocontour ($\alpha = 0.1$) of void fraction, (b) Time averaged C_p distribution, —— : LES, • : Experiment [7].

number is 0.4. The grid spacing used is $0.002D$ in both streamwise and wall normal directions and the grid is clustered close to the cavity inception region. A uniform grid spacing of $0.01D$ is used in the circumferential direction. The solution is initialised with a void fraction of $\alpha_0 = 0.01$. The non–dimensional time step $tu_\infty/D = 2 \times 10^{-5}$ and the solution is advanced in a time accurate manner. Figure 3.8(a) shows instantaneous isocontours of void fraction which vary in the circumferential direction and are unsteady in time. Figure 3.8(b) compares the time averaged C_p distribution to the experimental data [7]; good agreement is obtained indicating the suitability of the method in predicting bluff body cavitation also.

Chapter 4

Cavitation over a circular cylinder

4.1 Introduction

Although cavitation on lifting bodies has been extensively studied both experimentally [26, 50, 52] and numerically [18, 53, 54], relatively fewer studies exist for bluff bodies. Figure 4.1 shows the schematic of a low Reynolds number cavitating flow over a cylinder. As the liquid accelerates past the bluff body, pressure drops in the shear layer resulting in cavitation inception. The shear layer then rolls up into vortices and depending on the conditions, the vortices can also cavitate. These vortices are shed from the body into the relatively high pressure region in the wake. Here the vapor in the vortices collapses, resulting in pressure waves (also referred to as shock waves by many authors) which propagate both downstream and upstream. Cavitation behind bluff bodies can be categorized into three types [55, 56]: cyclic, fixed and transitional cavitation. A cyclic cavity sheds from the body periodically. A major portion of a fixed cavity remains attached to the body while small portions shed from the trailing edge of the attached portion. A transitional cavity displays both of these phenomena.

While bluff body wakes have been studied extensively for single phase flows [57–61],

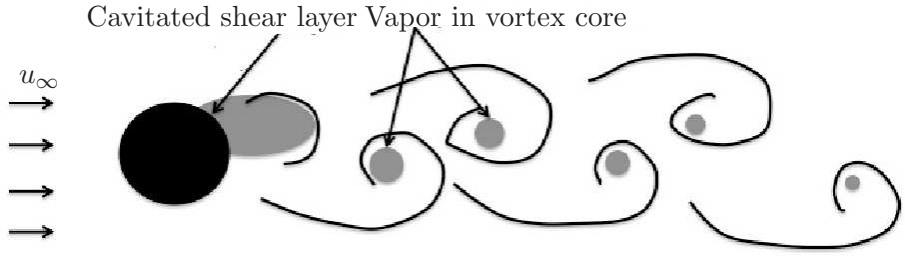

Figure 4.1: Schematic of vortex shedding and vapor formation in flow over a circular cylinder at low Reynolds number.

only a few studies exist that shed light on the effect of cavitation on Karman shedding and the near wake characteristics. Varga and Sebestyen [62] studied cavitation behind a circular cylinder with the main objective of understanding the noise generated by cavitation in water tunnels. Brandner et al. [63] conducted experiments on a sphere and observed periodic shedding caused by re-entrant jets. A few other studies [8, 64, 65] measured the shedding frequencies and cavity lengths in order to predict the effect of cavitation on the noise produced by a cavitating flow over a cylinder. Fry [55] conducted detailed experiments on the flow past a cylinder to study the effect of free stream velocity and cavitation number on the sound spectrum. He observed that the sound was correlated with the vortex shedding, and that larger cavities produced more sound upon collapse. Matsudaira et al. [56] experimentally studied Karman vortex cavities and found that regions of high impulse pressures occurred periodically behind the cylinder and were synchronized with the vortex shedding frequency. Balachandar and Ramamurthy [66] studied the effect of cavitation on base pressure coefficient and proposed a scaling based on wake parameters which unifies the wake pressure distribution for several cavitation numbers. Saito and Sato [67] observed that cavities that collapse near solid walls generate high impact on the walls due to their proximity to the walls. They also observed three patterns of cavity collapse : $3D$ radial, axial and $2D$ radial. Seo et al. [22] used DNS to compute sound produced by a cavitating flow over a cylinder at $Re = 200$ and found that the main source of noise in the cavitating flow was the

collapse of vapor cavities.

The wakes of two–dimensional wedges are another canonical configuration that have been studied experimentally, and differ from cylinder wakes in some respects. Young and Holl [68] measured vortex shedding frequency behind two–dimensional symmetric wedges and concluded that cavitation had a negligible effect on the frequency when the cavitation number was decreased from inception to half the incipient value. They also found that the shedding frequency reduced as choking conditions were approached. The flow over a wedge is relatively independent of Reynolds number unlike flow over circular cylinders. Also the dependence of the shedding frequency on cavitation number is different. Rao and Chandrasekhara [8] observe that the vortex shedding frequency for cylinders increased to large values when choking conditions were approached. Also for symmetric wedges, the existence of a maximum in the variation of Strouhal number with cavitation number is well established [68, 69] unlike that for cylinders.

The objective of this study is to assess the effect of cavitation on the near wake characteristics of a cylinder [70]. We consider two Reynolds numbers and four different cavitation numbers. Two interesting phenomena are observed: a low frequency cavity detachment and a reduction in vortex shedding frequency with decreasing cavitation number. In single phase flows, Gerrard [71] characterized vortex shedding frequency using two important length scales: the vortex formation length and the wake diffusion width. Strykowski and Sreenivasan [72] showed that introduction of a strategically placed control cylinder resulted in an increased diffusion causing vortex shedding suppression. They showed that vortex shedding frequency can be reduced and eventually completely suppressed. Dipankar et al. [73] and Mittal and Raghuvanshi [74] performed numerical studies that confirmed the control cylinder experiments. In this study, we analyze the effect of cavitation in reducing the vortex shedding frequency.

Also, the effect of cavitation nuclei which are included in the simulations in the form of initial vapor volume fraction is studied. Cavitation nuclei are known to play an important role in the inception process [14, 75–77]. Within the context of homogenous mixture models, the initial vapor volume fraction determines the speed of sound which is very sensitive to vapor volume fraction values < 0.1. The dynamics of pressure waves

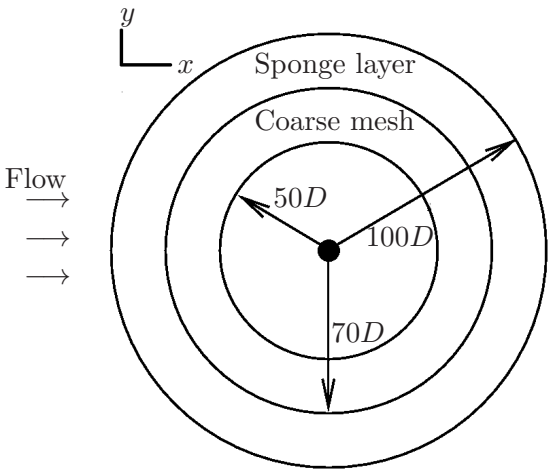

Figure 4.2: Computational domain illustrating sponge layer and region of coarse mesh (not to scale).

may therefore be affected even in advanced stages of cavitation. The Reynolds numbers considered in this study are 200 and 3900, which are low enough to allow parametric studies. A circular cylinder is chosen as the bluff body, since the Karman shedding behind a cylinder is well understood for single phase flows.

4.2 Problem Description

Figure 4.2 shows a schematic of the problem. A circular cylinder of diameter D is placed at the center of a circular domain of radius equal to $100D$, chosen to minimize acoustic reflection from the far field boundaries. The free stream flow is spatially uniform and the velocity is in the positive x direction as shown in Figure 4.2. The subscript ∞ is used to denote free stream conditions and $\rho_\infty, p_\infty, u_\infty$ and μ_∞ denote free stream density, pressure, velocity and dynamic viscosity respectively. Free stream conditions are imposed on all far field boundaries. Acoustically absorbing boundary conditions [78] are applied in the sponge layer shown in Figure 4.2. The term $-\gamma(\vec{q} - \vec{q}_{ref})$ is added to the governing equations, where γ is zero outside the sponge layer, $\vec{q}$ denotes the vector of conservative variables and the subscript 'ref' denotes the reference solution to which the flow inside the sponge layer is damped which in this case is the free stream value.

Reynolds number (Re)	**Cavitation number (σ)**	**Initial void fraction (α_0)**
200	2.0	0.01
200	1.0	0.01
200	0.7	0.01
200	0.5	0.01
200	1.0	0.005
3900	1.0	0.01

Table 4.1: Flow conditions used in the simulations.

Also the mesh is coarsened in the far–field to further reduce any reflections.

Table 4.1 lists the flow conditions for all the cases considered in this study. Here, cavitation number $\sigma = \frac{p_\infty - p_v}{0.5\rho_\infty u_\infty^2}$ and Reynolds number $Re = \frac{\rho_\infty u_\infty D}{\mu_\infty}$. The simulations are initialized with a spatially uniform void fraction (α_0) that nucleates the cavitation. Insensitivity to computational grid and domain size is demonstrated using two grids and two domain sizes for one case ($Re = 200$ and $\sigma = 1.0$). The mesh spacing for the fine grid is $0.005D \times 0.01D$ in the radial and azimuthal directions near the wall and stretches to $0.03D \times 0.03D$ at about $2D$ downstream and then further stretches to $0.07D \times 0.07D$ at a distance of $5D$ downstream. The coarse grid has a near wall mesh spacing of $0.01D \times 0.02D$ and stretches to $0.05D \times 0.05D$ at about $2D$ downstream. The corresponding domain radii are $100D$ and $50D$ respectively. Figure 4.3 shows the lift and drag coefficient as function of time for both the grids. Note that the solutions show good agreement, and the fine grid and the larger domain has therefore been used for all the subsequent simulations at $Re = 200$. The mesh spacing and the spanwise extent for the $3D$ simulation are the same as that in the simulation of Verma and Mahesh [9] for a single phase flow at the same Reynolds number, where good agreement was obtained with experiment. The near wall mesh spacing is $0.002D \times 0.005D$ in size and stretches to $0.004D \times 0.003D$ at a downstream location of $5D$. Since the presence of vapor decreases the effective Reynolds number, this resolution is deemed sufficient.

The nature of the instantaneous solution is illustrated in Figure 4.4 using the $Re = 200$ and $\sigma = 1.0$ simulation. The void fraction contours show the presence of vapor immediately downstream of the cylinder as well as in the core of the Karman vortices

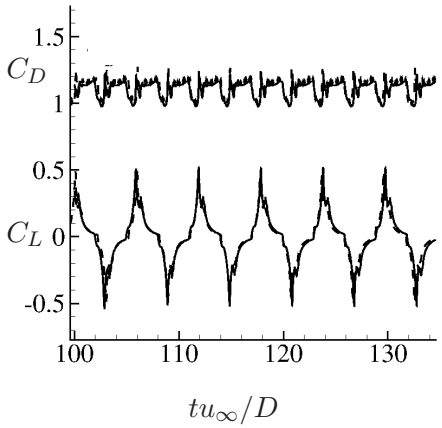

Figure 4.3: Comparison of lift and drag coefficient history showing grid convergence between two grids and domain insensitivity between two domains (----) : Coarse grid, Small domain (——): Fine grid, Big domain.

downstream. The superposed contour lines of pressure show the presence of 'pressure waves', which are compression waves that form when vapor pockets collapse in the higher pressure regions downstream of the cylinder. The speed of sound drops significantly in regions of vapor resulting in supersonic Mach numbers in some parts of the flow. Figure 4.4 (b) reveals Mach numbers as high as 6 in the cavitated shear layer immediately downstream of the cylinder. The large spatial variation in sound speed results in the pressure waves refracting through the near field vapor and impinging upon the cylinder. The $Re = 3900$ flow exhibits similar qualitative behaviour and is discussed in Section 4.5.

The effect of σ on the time averaged flow behind the cylinder as well as the unsteady loads on the cylinder are discussed below (Section 4.3) for $Re = 200$. The $\sigma = 0.7$ and 0.5 flows exhibit a 'low frequency cavity detachment' phenomenon, where a pocket of vapor attached to the cylinder sheds downstream. This behaviour is analyzed in Section 4.3.6. σ also affects the Karman vortex shedding frequency which is discussed in Section 4.3.7. The influence of α_0 is considered in Section 4.4 and LES of the $Re = 3900$ flow is discussed in Section 4.5.

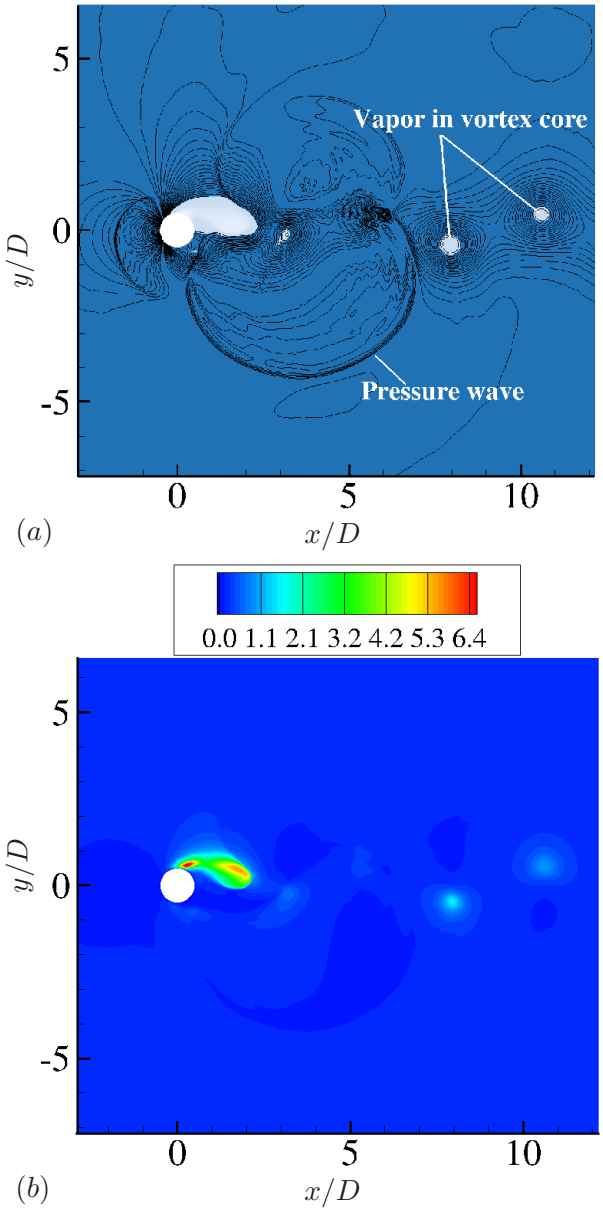

Figure 4.4: (a) Instantaneous snapshot showing colored contours of void fraction and contours lines showing pressure. (b) Instantaneous Mach number contours.

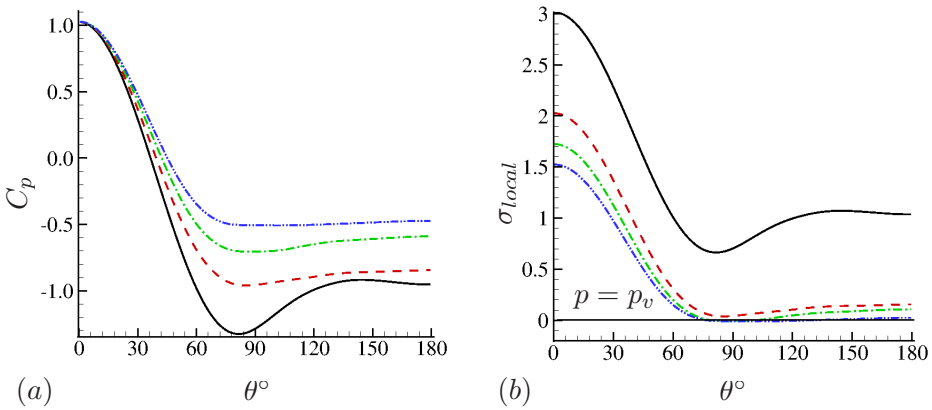

Figure 4.5: (a) Time averaged C_p on the cylinder, (b) Time averaged distribution of σ_{local} on the cylinder, ——— : $\sigma = 2.0$, - - - - : $\sigma = 1.0$, —·—·— : $\sigma = 0.7$, —··—·· : $\sigma = 0.5$.

4.3 Effect of cavitation number (σ)

Cavitating flows at three different cavitation numbers (σ = 1.0, 0.7 and 0.5) are considered and compared to the non-cavitating flow at $\sigma = 2.0$. The cavitation number is varied by changing the free stream velocity while keeping all other quantities constant. The flow is seeded with a free stream void fraction of $\alpha_0 = 0.01$.

4.3.1 Pressure on the cylinder surface

Figure 4.5(a) shows the mean pressure coefficient on the cylinder surface. Here, θ = 0° and 180° correspond to the leading edge stagnation point and trailing edge respectively. In the absence of cavitation, the pressure coefficient decreases to its minimum value at approximately 80 degrees as the flow accelerates from the stagnation point, then increases as the flow decelerates, prior to becoming approximately constant in the wake region at the trailing edge. Cavitation is seen to decrease the magnitude of minimum C_p, with lower values of σ causing a larger decrease in magnitude. This is because once flow cavitates (close to the minimum C_p location), the pressure in the vapor region remains close to the vapor pressure; it does not further decrease with fluid acceleration. The upstream flow therefore sees lower values of favorable pressure gradient and the downstream flow experiences approximately constant pressure.

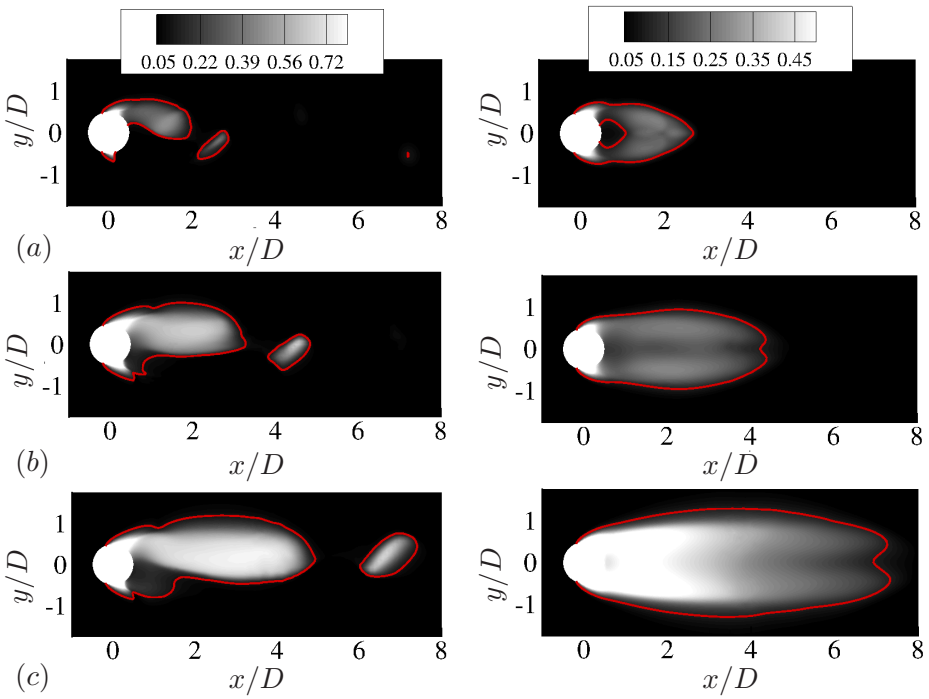

Figure 4.6: Instantaneous (left) and mean (right) void fraction contours for (a) $\sigma = 1.0$, (b) $\sigma = 0.7$ and (c) $\sigma = 0.5$.

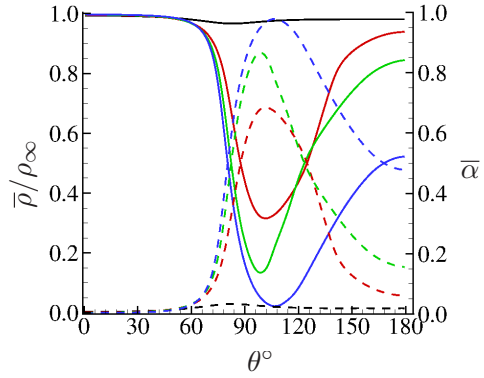

Figure 4.7: Variation of density (solid) and void fraction (dashed) along the cylinder surface as a function of azimuthal location, —— : $\sigma = 2.0$, —— : $\sigma = 1.0$, —— : $\sigma = 0.7$, —— : $\sigma = 0.5$.

Defining $\sigma_{local} = 2(p - p_v)/\rho_\infty u_\infty^2$ and $\sigma_\infty = 2(p_\infty - p_v)/\rho_\infty u_\infty^2$ yields $\sigma_{local} = C_p + \sigma_\infty$. Figure 4.5(b) reveals small values for σ_{local} downstream of the minimum C_p location on the cylinder surface for the cavitating flows. Also, for $\sigma = 1.0$ the mean pressure is always above vapor pressure, whereas for $\sigma = 0.7$ and 0.5, the mean pressure falls below vapor pressure and recovers to values slightly above vapor pressure near the trailing edge of the cylinder. High density fluid can therefore be present near the trailing edge, in the mean flow. This behavior is illustrated in figure 4.6 which shows contours of instantaneous and mean void fraction. Since when $\sigma = 1.0$, only the instantaneous pressure falls below vapor pressure, vapor is observed largely in the core of the Karman vortices. In contrast, when $\sigma = 0.7$ and 0.5, since the mean pressure in the near wake is also below vapor pressure, vapor is also present in substantial portions of the near–wake. Figure 4.7 shows the variation of mean void fraction and mixture density along the cylinder surface from the leading edge towards the trailing edge. Note the presence of higher density fluid near the trailing edge, and that the mean void fraction is not necessarily 1 due to vapor unsteadiness. Although vapor decreases the density of the mixture, the density is still skewed towards the liquid due to its significantly higher value.

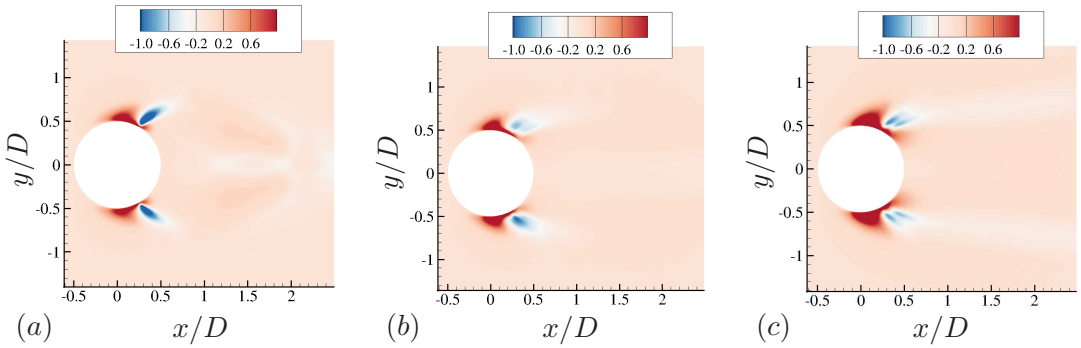

Figure 4.8: Contours of divergence of velocity field for $(a)\ \sigma = 1.0$, $(b)\ \sigma = 0.7$ and $(c)\ \sigma = 0.5$.

4.3.2 Velocity divergence due to cavitation

Cavitation causes density change which implies a considerable change in the divergence of the velocity field. Figure 4.8 shows the mean velocity divergence ($\nabla.\vec{V}$) contours for all the cavitating cases. Expansion caused due to cavitation can be seen as positive divergence and as the flow cavitates more, the region of positive $\nabla.\vec{V}$ also increases due to the increased amount of vapor. It is interesting to note a compression region (negative $\nabla.\vec{V}$) downstream of the expansion region and the magnitude of this compression region appears to decrease as the cavitation number reduces. This behavior can be understood by revisiting the mean void fraction contours in Figure 4.6. For $\sigma = 1.0$, there is large decrease in void fraction corresponding to the region of negative divergence. This is a result of the cavitating vortex being shed from the body, which takes away vapor from close to the body leading to a sharp decrease in void fraction in the mean, However, we observe that for $\sigma = 0.7$ and 0.5, the void fraction does not decrease as much as in $\sigma = 1.0$, since for these cases, the cavitating vortex sheds from the attached cavity at a downstream location. Thus this compression region is an indication of some amount of vapor being converted back to water.

4.3.3 Boundary layer on the cylinder surface

The pressure along the cylinder surface affects evolution of the boundary layer. Figure 4.9 shows boundary layer velocity profiles at four different azimuthal locations for $\sigma =$

2.0 and 0.5. The azimuthal locations $\theta = 70°,\ 90°,\ 110°$ and $130°$ are chosen to represent regions of favorable pressure gradient, minimum pressure, adverse pressure gradient and separated flow respectively. The figure contrasts only $\sigma = 2.0$ (non–cavitating) and 0.5 (cavitating) cases for clarity. Here, u_θ is the tangential velocity and r is the normal distance from the cylinder at any given azimuthal location. Cavitation causes expansion (positive dilatation) at the inception location which causes the flow upstream to decelerate as seen in Figure 4.9. For instance, the maximum velocity in the boundary layer ($u_{\theta_{max}}/u_\infty$) drops to a value of 1.10 for $\sigma = 0.5$ from a value of 1.34 for $\sigma = 2.0$ at an azimuthal location of 70°. The location where maximum velocity in the boundary layer occurs is also shifted away from the wall for the cavitating flow as a result. The magnitude of the maximum velocity in the boundary layer ($u_{\theta_{max}}$) and the location of its occurrence are plotted as a function of θ in Figure 4.10 for all four cases. Note that the boundary layer thickens with decreasing cavitation number. Also the magnitude of $u_{\theta_{max}}$ initially increases in the favorable pressure gradient region and then drops after 80°. The drop in magnitude of $u_{\theta_{max}}$ is rapid for $\sigma = 2.0$ after 90° when compared to the cavitating flow, which points to a rapid thickening of the boundary layer leading to separation. The location of maximum velocity is shifted away from the wall as the flow cavitates more and this difference between cavitating and non–cavitating flow increases further as we move closer to the trailing edge.

Figure 4.11 shows the time averaged skin friction distribution along the cylinder. The magnitude of C_f initially increases in the favorable pressure gradient region and then drops as the boundary layer thickens due to adverse pressure gradient. Note that the cavitating flows have a reduced skin friction value compared to $\sigma = 2.0$ upto 80° due to the deceleration caused by the vapor cavity. Flow expansion due to cavitation also causes the flow downstream of the inception location to accelerate. This can be seen in the form of a local increase in skin friction co-efficient in Figure 4.11 for $\sigma = 1.0,\ 0.7$ and 0.5 at about 80°.

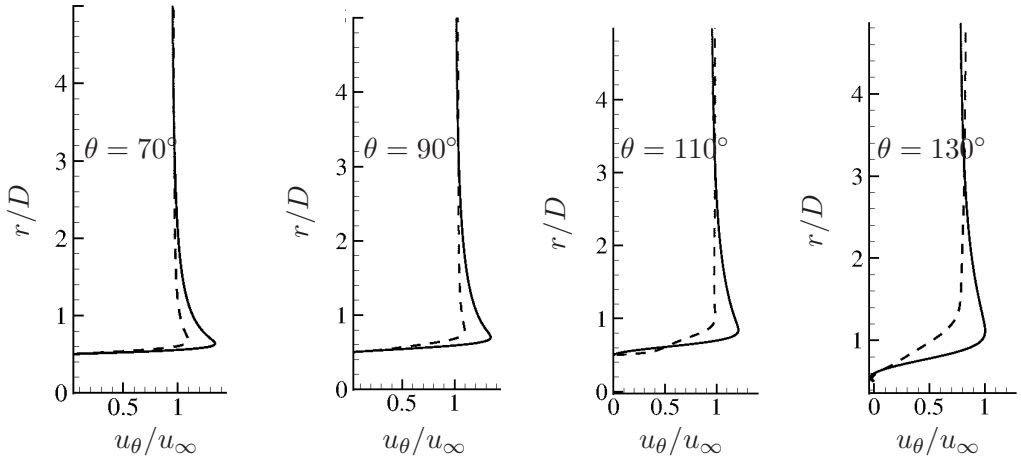

Figure 4.9: Boundary layer profile at four azimuthal locations, —— : $\sigma = 2.0$ and ---- : $\sigma = 0.5$.

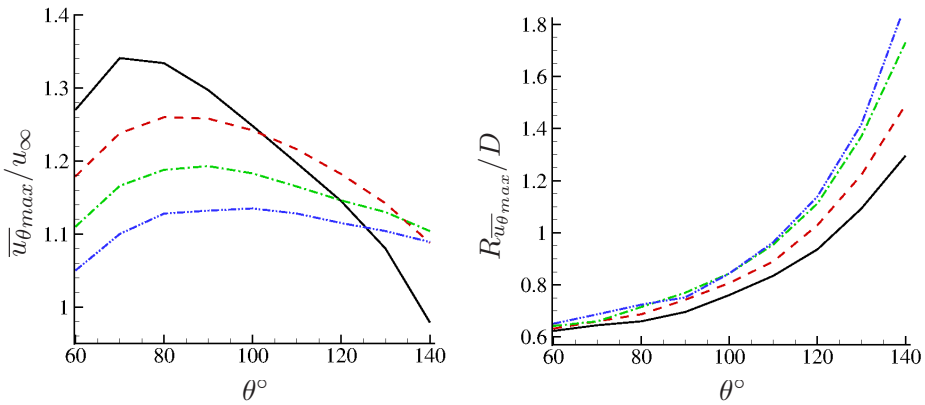

Figure 4.10: (a) Variation of maximum velocity in boundary layer as a function of azimuthal location, (b) Variation of location of maximum velocity in boundary layer as a function of azimuthal location, —— : $\sigma = 2.0$, ---- : $\sigma = 1.0$, –·–·– : $\sigma = 0.7$, –··–··– : $\sigma = 0.5$.

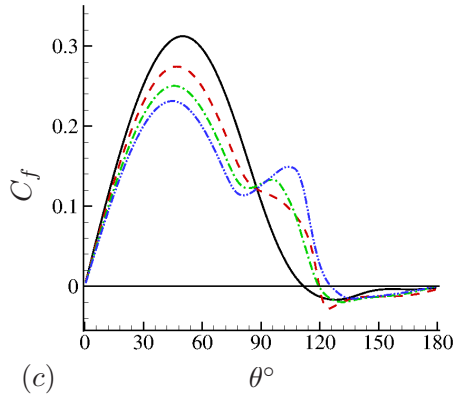

Figure 4.11: Time averaged skin friction coefficient distribution on the cylinder, —— : $\sigma = 2.0$, - - - - : $\sigma = 1.0$, –·–·– : $\sigma = 0.7$, –··–··– : $\sigma = 0.5$.

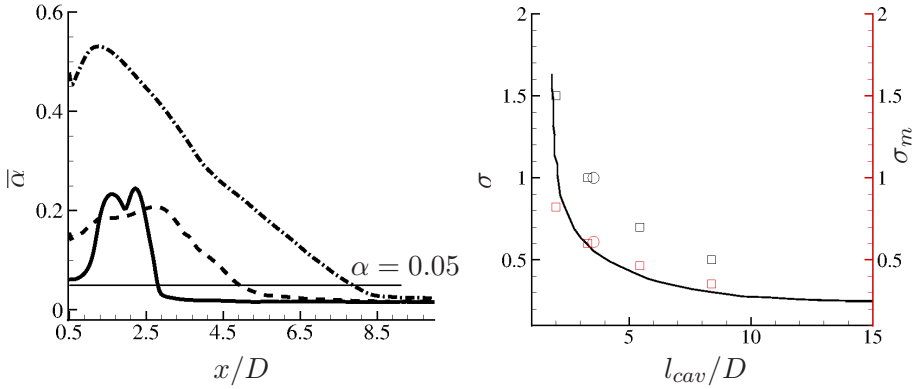

Figure 4.12: (a) Variation of $\overline{\alpha}$ with downstream distance in the wake, —— : $\sigma = 1.0$, - - - - : $\sigma = 0.7$ and – · – · – : $\sigma = 0.5$. (b) Variation of normalized cavity length with cavitation number, —— : Experimental fit Rao and Chandrasekhara [8], ▫ : $Re - 200$, ○ : $Re - 3900$.

4.3.4 Cavity length

The mean cavity length progressively increases as the cavitation number decreases. The mean length of the cavity is computed from Figure 4.12 (a) as the location downstream where $\overline{\alpha}$ reaches a value of 0.05 after its initial increase. This figure also shows the maximum $\overline{\alpha}$ obtained in the near wake. As the cavitation number decreases, it is expected that more vapor will be formed in the wake. Interestingly, the $\overline{\alpha}_{max}$ is higher for $\sigma = 1.0$, when compared to $\sigma = 0.7$. This is due to the effect of the low frequency cavity detachment when $\sigma = 0.7$, which will be discussed in detail in Section 4.3.6. The mean cavity length as a function of cavitation number is shown in Figure 4.12 (b) and shows that the length increases as cavitation number is reduced. The plot also shows the mean cavity length as a function of a modified cavitation number $\sigma_m = \frac{p-p_v}{0.5\rho u_{max}^2}$. Here, u_{max} is the maximum mean velocity in the boundary layer which is obtained from Figure 4.10. This modification was first suggested by Rao and Chandrasekhara [8], who observed that when mean cavity length was plotted against σ, a family of curves were obtained for different Reynolds numbers for cavitating flow over a circular cylinder. Hence they introduced the modified cavitation number which unified the different family of curves onto a single curve. We observe in Figure 4.12 (b) that the mean cavity length obtained at a lower Reynolds number also collapses onto this experimental fit if the modified cavitation number is used. Given that the experimental fit is obtained purely based on experiments at high Reynolds number (typically 10^5), it is interesting to see that the data from our low Reynolds number simulations also collapses onto this curve.

4.3.5 Unsteady loads on the cylinder

Figure 4.13 shows the unsteady characteristics of the flow in the form of lift and drag history and their corresponding spectra in the frequency domain. The Strouhal number (fD/u_∞ where f is the vortex shedding frequency) computed from the lift and drag histories are tabulated in Table 4.2. Further, it is also verified that the same shedding Strouhal number is obtained from the pressure history at three different points at x/D = 2.5, 5.0 and 10.0 along the wake center line (not shown here). The lift and drag

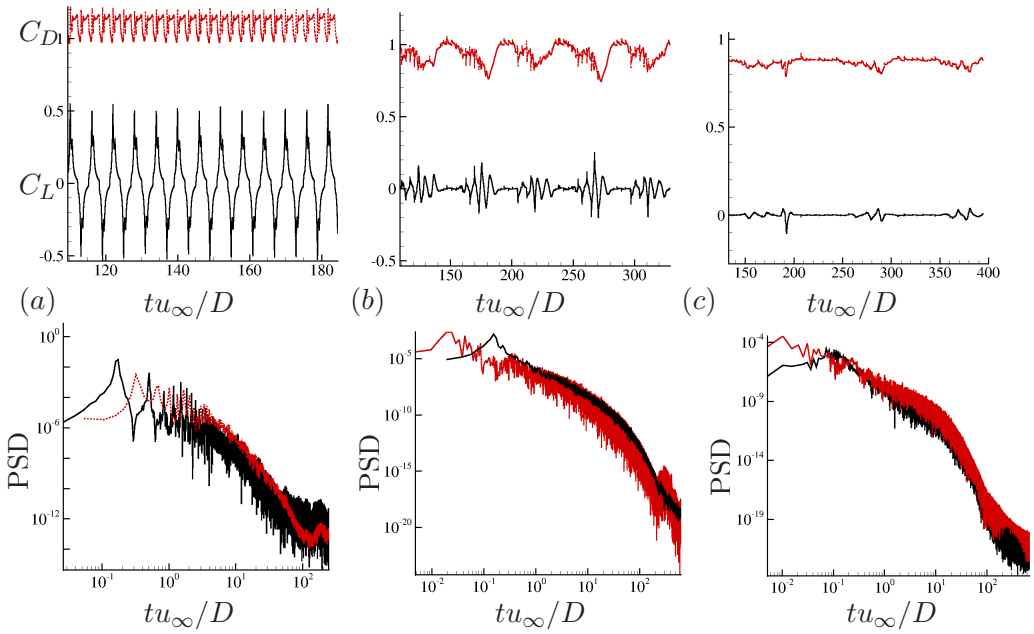

Figure 4.13: Lift and Drag history and their spectra for (a) $\sigma = 1.0$, (b) $\sigma = 0.7$ and (c) $\sigma = 0.5$, —— : C_L, ---- : C_D.

curve for $\sigma = 1.0$ in Figure 4.13 (a) is periodic (but not sinusoidal as in a single phase flow) and the cavitating vortices are shed at periodic intervals. The cavitating vortices in $\sigma = 1.0$ shed directly from the body and hence this flow belongs to the cyclic cavitation category. The Strouhal number for $\sigma = 1.0$ is reduced to 0.16 from a value of 0.19 for a single phase flow at $Re = 200$. Apart from the primary peaks which correspond to the pressure variation due to vortex shedding, smaller secondary peaks are also observed in the lift curve. These secondary peaks correspond to those instants when a pressure wave impinges on the cylinder. The lift and drag histories for $\sigma = 0.7$ and 0.5 in Figures 4.13 (b) and (c) are quasi–periodic with more than one frequency being observed. Further, the magnitude of fluctuations are also reduced when compared to $\sigma = 1.0$ pointing to a more steady behaviour near the cylinder as the flow cavitates more. The cavitating vortex does not shed directly from the body as in $\sigma = 1.0$, but from the trailing edge of the cavity attached to the cylinder. The Strouhal number corresponding to this shedding is 0.15 for $\sigma = 0.7$. At $\sigma = 0.5$, the vortex

Cavitation number (σ)	**Strouhal number (from C_L)**	**Strouhal number (from C_D)**
2.0	0.1984	0.3967
1.0	0.1603	0.3206
0.7	0.1526	0.3042
0.5	0.08–0.103	0.2231

Table 4.2: Strouhal number obtained from lift and drag coefficient history.

shedding becomes intermittent and a peak is observed between a Strouhal number of 0.08 and 0.11. Thus decreasing cavitation number has two main effects on the unsteady loads: vortex shedding frequency is reduced, the mechanism of which will be discussed in Section 4.3.7 and the magnitude of unsteady loads on the cylinder is also reduced pointing to a more steady behaviour near the cylinder.

Figure 4.14 illustrates the dynamics of vapor cloud collapse and the subsequent pressure wave formation for $\sigma = 1.0$. This figure shows void fraction contours, pressure contours and the corresponding instant in the load cycle for various instants of time. Figure 4.14 (a) shows the impending collapse of the vapor cavity, and (b) shows the subsequent collapse of the cavity leading to two separate smaller regions of vapor denoted as Cav 1 and Cav 2. This collapse causes a pressure wave (Wav 1) that propagates outwards. By this time, the separated cavity (Cav 2) also collapses leading to another pressure wave (Wav 2) as shown in (c). (d) shows the fully formed vapor cavity on the top half of the cylinder and this entire cycle repeats itself. This process of cloud collapse and pressure wave formation is similar for both $\sigma = 0.7$ and 0.5, except for a low frequency detachment of the vapor cavity in the wake in these two cases.

4.3.6 Low frequency cavity detachment in $\sigma = 0.7$ and 0.5

For $\sigma = 0.7$ and 0.5, in addition to the vortex shedding from the trailing edge of the attached cavity, the entire attached vapor cavity also gets detached as a part of the cycle. As a result, the near wake is cavitation–free for a small interval of time. For $\sigma = 0.7$ this cavitation–free time period is approximately 20 tu_∞/D and for $\sigma = 0.5$ it is approximately 30 tu_∞/D. The frequency corresponding to this detachment can be

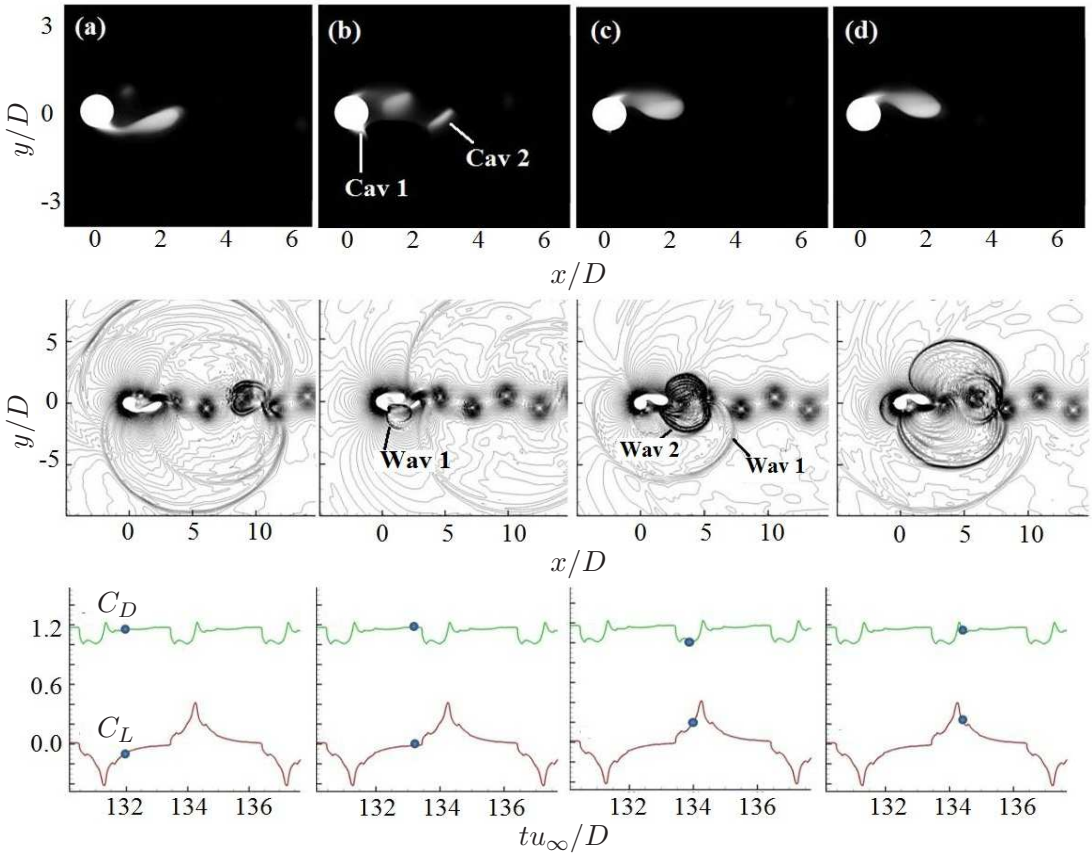

Figure 4.14: Vapor collapse dynamics for $\sigma = 1.0$.

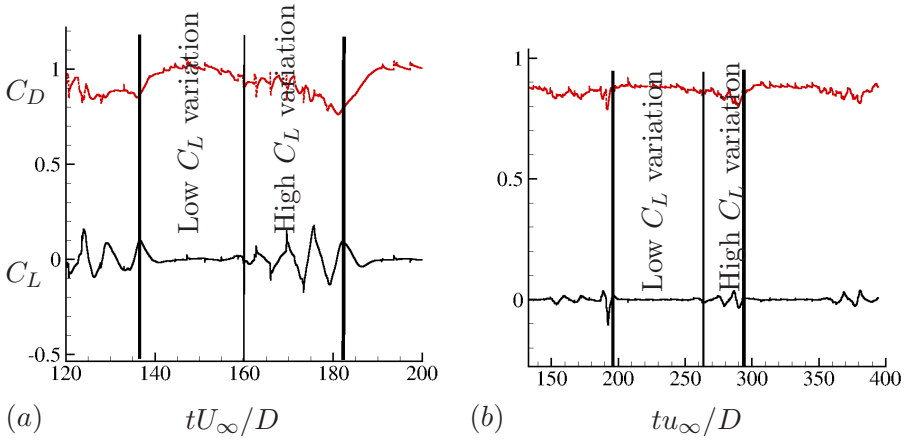

Figure 4.15: Time history of lift showing two phenomena in a single cycle for (a) $\sigma = 0.7$ and (b) $\sigma = 0.5$, —— : C_L, ---- : C_D.

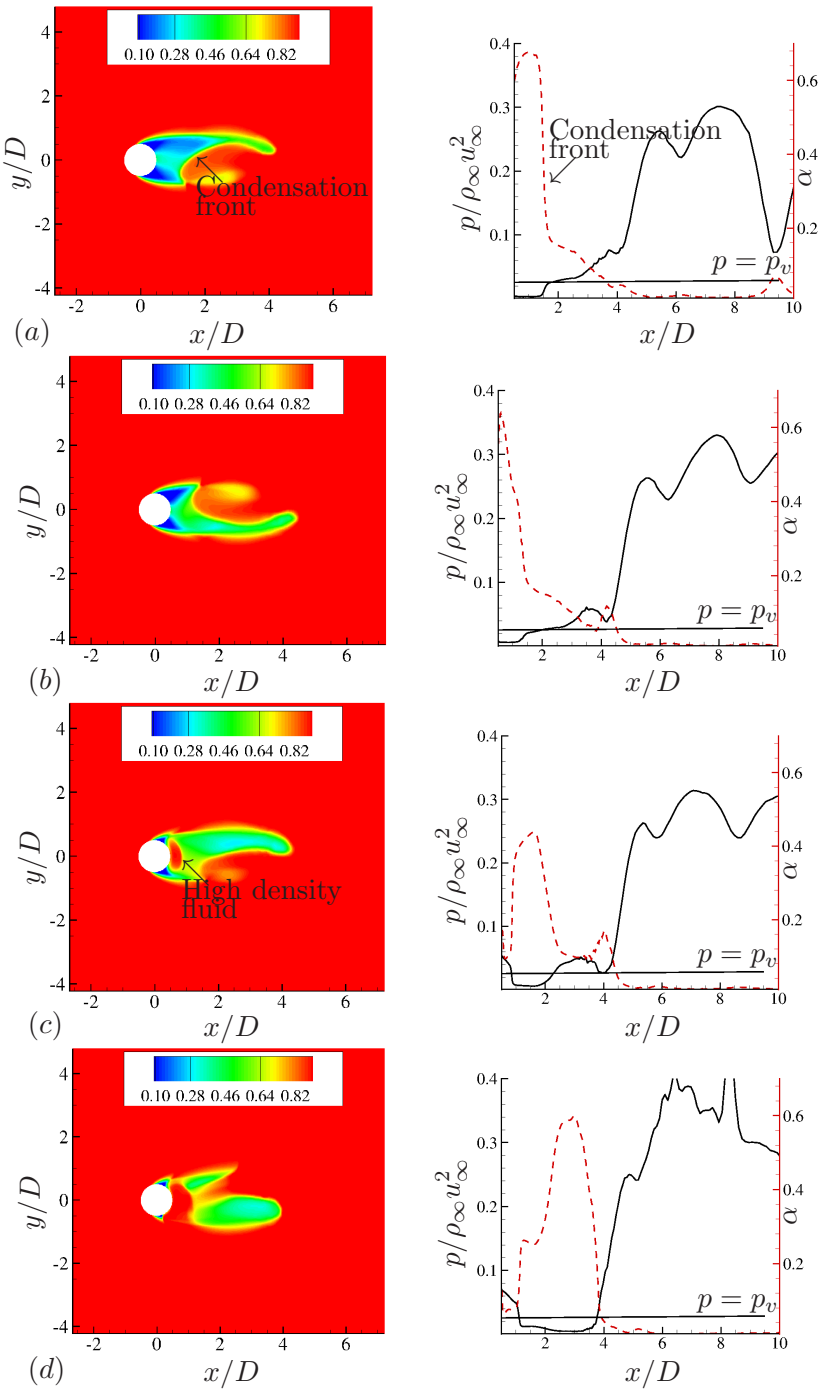

Figure 4.16: (left) Density contours at four time instants illustrating propagating condensation front causing cavity detachment, (right) Variation of pressure and void fraction along wake center line at four time instants.

observed as a peak in the drag spectra in Figures 4.13 (b) and (c) and is computed to be 0.0218 for $\sigma = 0.7$ and 0.0102 for $\sigma = 0.5$. The lift curves in Figure 4.15(a) and (b) suggest that there are two distinct parts within one cycle: one with a relatively low variation in C_L and other with a higher variation in C_L. The first part with low C_L variation corresponds to the time when the vapor cavity is attached to the body. Since the pressure in vapor region is close to vapor pressure, variation in C_L is very small. As the vapor cavity detaches, water in the wake causes higher variations in the lift coefficient.

The mechanism behind this detachment is illustrated in Figure 4.16, where a series of snapshots show the presence of a propagating condensation front, that causes cavity detachment from the base of the cylinder. (a-b) show the propagation of condensation front towards the low pressure base. This causes the pressure in the base to increase which can be seen as a small patch of high density fluid near the base of the cylinder (c). This causes the vapor cavity to detach as seen in (d). The detached cavities advect downstream leaving the near wake cavitation free for a while. The presence of condensation front can also be seen from the line plots in the figure. The pressure increase and the corresponding void fraction decrease close to $x/d = 2.0$ seen in (a) and (b) is the condensation front. (c) and (d) also show the presence of high density (low void fraction) fluid near the base once the cavity detaches.

4.3.7 Mechanism of vortex shedding frequency reduction

At low Reynolds number, the vorticity transported into the wake from the boundary layers on the cylinder is diffused away from the shear layer predominantly by viscous action. As Reynolds number increases, viscous diffusion alone cannot keep up with the increased vorticity production from the boundary layers, and so vortices break away at regular intervals, constituting vortex shedding [72]. Gerrard [71] observed vortex street formation to be a function of two length scales: formation length and diffusion length. Formation length l_f is defined as the distance downstream of the cylinder along the center line where the streamwise velocity fluctuations are maximum and diffusion length l_d is the width to which the free shear layers diffuse. He found that vortex

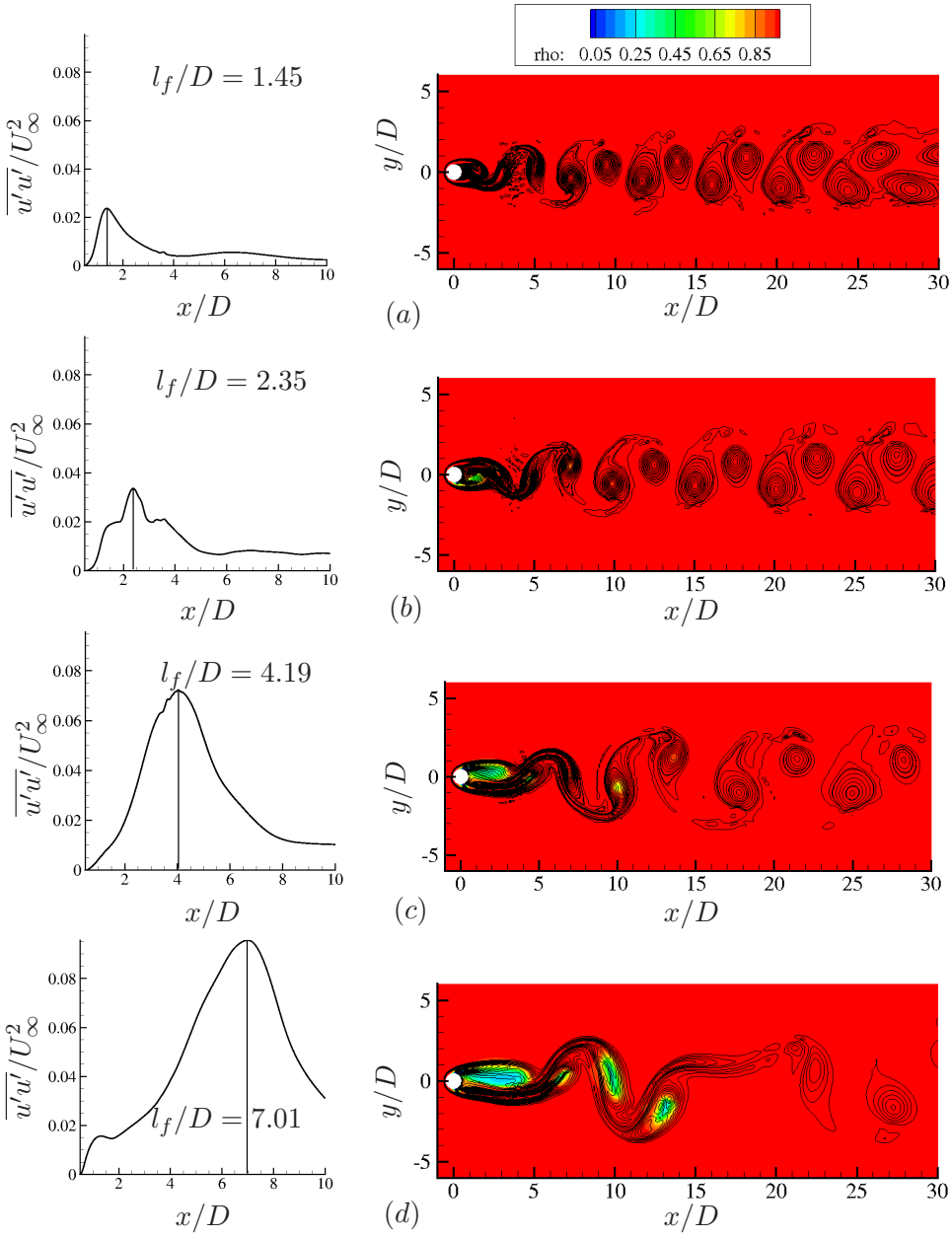

Figure 4.17: Formation length (left) and Instantaneous vorticity contours colored with density (right) for (*a*) $\sigma = 2.0$, (*b*) $\sigma = 1.0$, (*c*) $\sigma = 0.7$ and (*d*) $\sigma = 0.5$.

shedding frequency could be reduced if the shear layer vorticity was reduced over a critical diffusion length which in turn increases the formation length.

In order to understand the mechanism of vortex shedding suppression due to cavitation, we first compute the formation length (l_f) by plotting the streamwise velocity fluctuations in Figure 4.17 for $\sigma = 2.0, 1.0, 0.7$ and 0.5. The formation length is seen to increase with decreasing cavitation number which signifies a reduction in shedding frequency [71]. It is also worthwhile to note that the magnitude of streamwise velocity fluctuation also increases as the flow cavitates. This points out to higher oscillations at the cavity closure as σ is lowered. Also shown in Figure 4.17 are the instantaneous vorticity contours showing fewer vortices being shed over a given distance as the cavitation number is reduced.

Figure 4.18 shows the mean vorticity distribution in the top half of the shear layer. The arguments presented here can be applied to the bottom half also by symmetry. Note that the magnitude of negative vorticity in the top shear layer decreases progressively as cavitation number decreases. Thus cavitating flow has lesser vorticity across a given shear layer width and the reason for this reduction is explained below using the vorticity equation,

$$\frac{\partial \boldsymbol{\omega}}{\partial t} = -(\boldsymbol{v}.\boldsymbol{\nabla})\boldsymbol{\omega} + (\boldsymbol{\omega}.\boldsymbol{\nabla})\boldsymbol{v} - \boldsymbol{\omega}(\boldsymbol{\nabla}.\boldsymbol{v}) + \frac{1}{\rho^2}(\boldsymbol{\nabla}\rho \times \boldsymbol{\nabla}p) + \boldsymbol{\nabla} \times \frac{\boldsymbol{\nabla}.\tau}{\rho}. \qquad (4.1)$$

For a non–cavitating flow, the vorticity dilatation term ($\boldsymbol{\omega}(\boldsymbol{\nabla}.\boldsymbol{v})$) and the baroclinic vorticity ($\frac{1}{\rho^2}(\boldsymbol{\nabla}\rho \times \boldsymbol{\nabla}p)$) terms are zero. However for a cavitating flow, these values are non–zero. Figure 4.18 shows the contribution of the mean baroclinic vorticity term. At the inception location, baroclinic vorticity is produced because pressure becomes a function of both vapor mass fraction and density thus causing a misalignment between pressure and density gradients. The baroclinic term produces more negative vorticity on the top half for all the cavitating cases thus increasing the total vorticity in the shear layer. The main reason for vorticity reduction is the vorticity dilatation term. As seen in Figure 4.8, there is a large region of positive divergence (expansion) corresponding to the vapor region. The magnitude of vorticity dilatation is also shown in Figure 4.18.

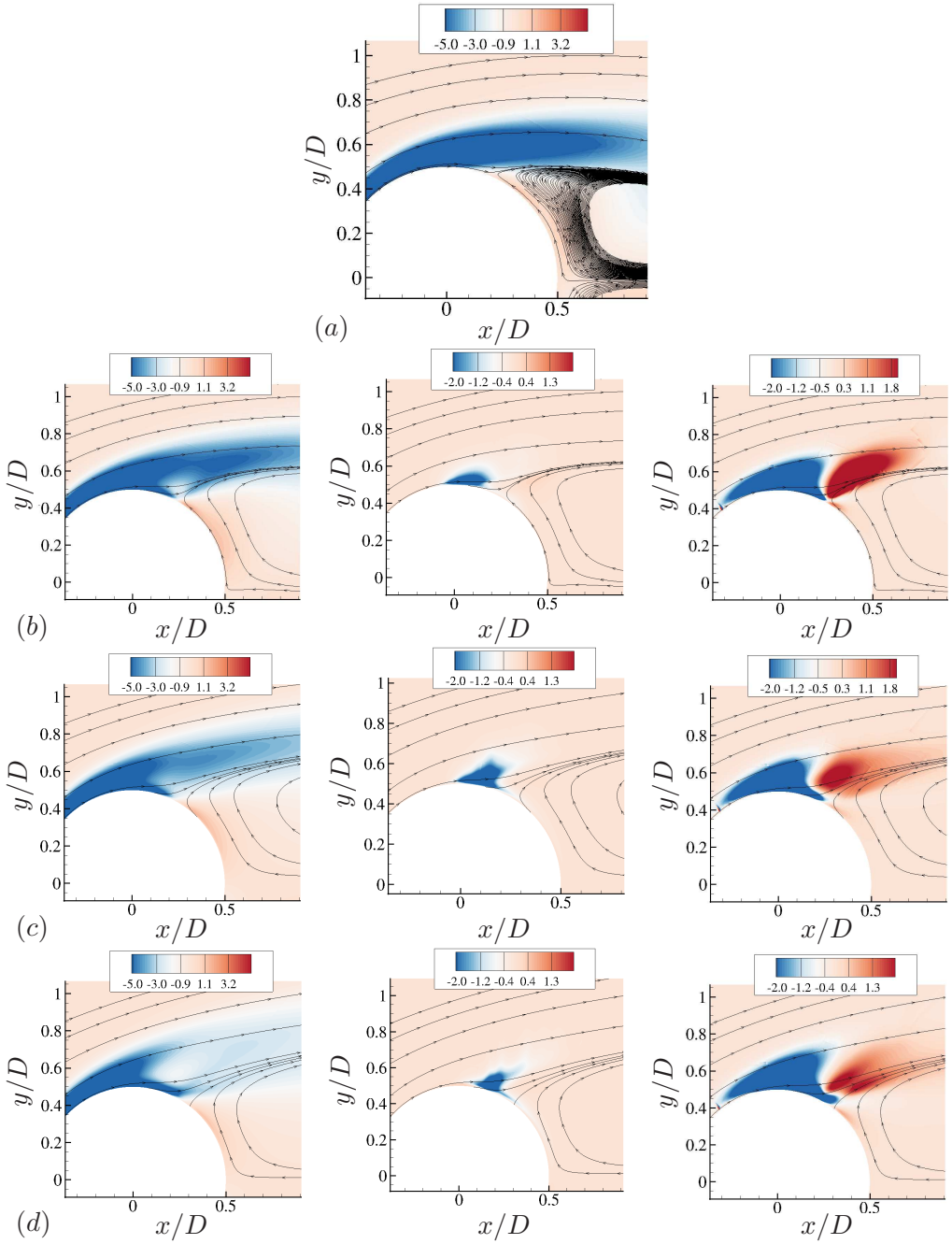

Figure 4.18: Mean vorticity contours (left), Mean baroclinic vorticity (center) and Mean Vortex dilatation (right) for (a) $\sigma = 2.0$, (b) $\sigma = 1.0$, (c) $\sigma = 0.7$ and (d) $\sigma = 0.5$.

Cavitation number (σ)	**Circulation** (Γ)	**Formation length** (l_f/D)
2.0	4.80	1.45
1.0	4.03	2.35
0.7	3.08	4.19
0.5	2.78	7.01

Table 4.3: Values of circulation Γ and formation length l_f.

Note that this term appears in the right hand side of the vorticity equation with a negative sign. The blue region corresponds to vorticity dilatation which reduces the vorticity in the shear layer. The compression region (discussed in Section 4.3.2) causes the vorticity to increase downstream shown as the red contours: however the larger influence of expansion region results in a net decrease in vorticity.

To quantify the extent of vorticity reduction, the circulation in the shear layer is computed as $\oint \vec{V}.\ \vec{dl}$ over a rectangular domain from $0.5 < x/D < 4.0$ and $0 < y/D < 1.0$, where the center of the cylinder lies at the origin. As the flow cavitates more, the amount of circulation decreases pointing to reduced vorticity in the shear layer. Table 4.3 lists the value of circulation and the corresponding formation length for all the cases. Thus the presence of vapor in the wake causes dilatation of vorticity resulting in a reduction of the vortex shedding frequency.

4.4 Effect of initial void fraction

In this section, we discuss the effect of initial void fraction (α_0) on the flow field by simulating $\sigma = 1.0$ flow with $\alpha_0 = 0.005$ and comparing it to $\alpha_0 = 0.01$. The main effect of changing α_0 is the change in free stream speed of sound. At a temperature of 293 K and a pressure of 1 bar, the speed of sound in a mixture with $\alpha_0 = 0.01$ is 100.24 m/s, while that at $\alpha_0 = 0.005$ is 141.07 m/s. Hence pressure waves propagating in the medium will travel at these substantially different speeds which would affect related phenomena. However, phenomena that are driven largely by inertia (for e.g. cavitation in shear layer, vortex shedding) are not expected to vary significantly.

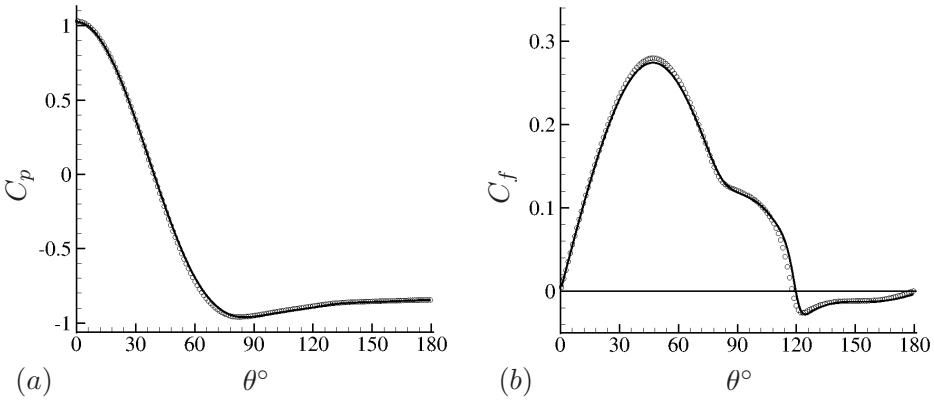

Figure 4.19: (a) Time averaged C_p distribution on the cylinder, (b) Time averaged C_f distribution on the cylinder, —— : $\alpha_0 = 0.01$, $\circ$: $\alpha_0 = 0.005$.

4.4.1 Mean C_p and C_f distribution on the cylinder

The time averaged C_p distribution and C_f distribution are shown as a function of θ in Figures 4.19 (a) and (b) for both $\alpha_0 = 0.01$ and 0.005. Note that neither C_p nor C_f vary significantly for different α_0. The time averaged load on a cylinder is predominantly due to the alternate vortex shedding which is not affected significantly by change in acoustic speed. The inflection point (at $\theta = 80^\circ$) in the C_f curve that indicates the cavity inception location (as discussed in Section 4.3) also remains unchanged between the two flows. Figure 4.20 shows the mean void fraction contours for both the flows. The cavity shape and cavity length ($l_{cav}/D = 2.71$) remain largely unaffected.

4.4.2 Unsteady loads on the cylinder

The effect of changing α_0 on the unsteady loads is investigated in Figure 4.21 (a) and (b). The lift and drag history shown in Figure 4.21 (a) is very similar to the $\alpha_0 = 0.01$ (Figure 4.13 (a)) case and the corresponding shedding Strouhal number obtained in Figure 4.21 (b) is also unaltered. The only effect of reducing α_0 below 0.005 is an increase in the speed of sound in the medium, effectively reducing the Mach number of the flow, which is not expected to affect the shedding characteristics significantly. Figure 4.21 (c) shows a single lift and drag cycle for both the cases. It can be observed that the time period

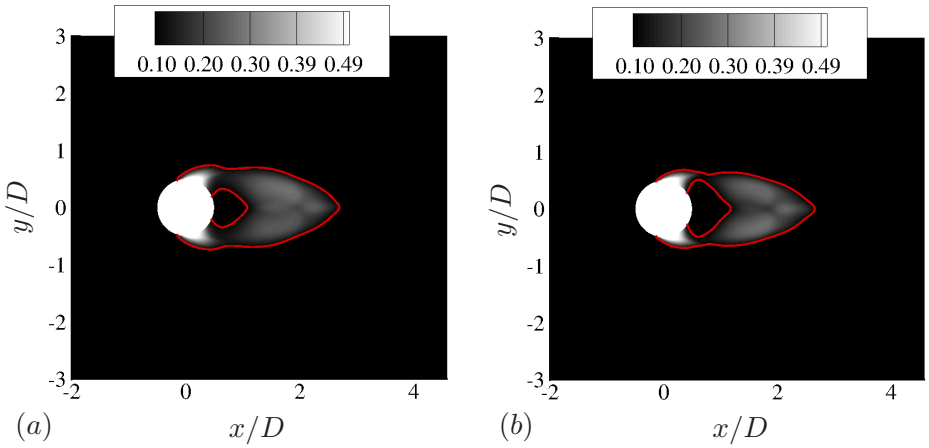

Figure 4.20: Mean void fraction contours for (a) $\alpha_0 = 0.01$ and (b) $\alpha_0 = 0.005$.

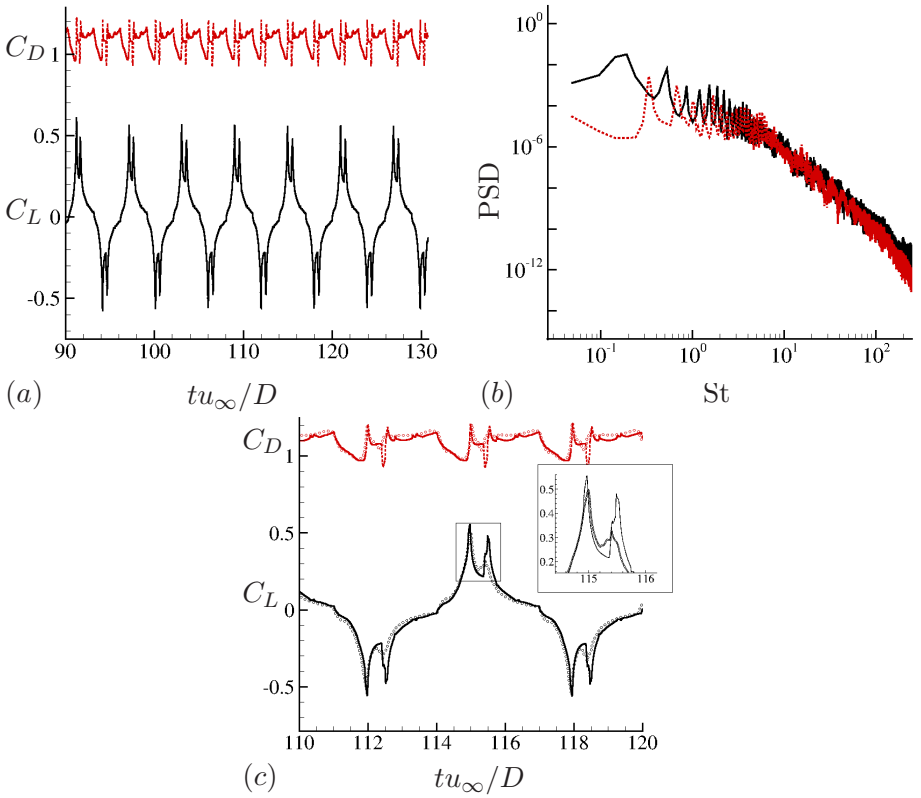

Figure 4.21: (a) Lift and drag history for $\alpha_0 = 0.005$ (b) Power spectral density for $\alpha_0 = 0.005$, —— : C_L, ---- : C_D, (c) Comparison of a single lift and drag cycle for $\circ$: $\alpha_0 = 0.01$ and —— : $\alpha_0 = 0.005$.

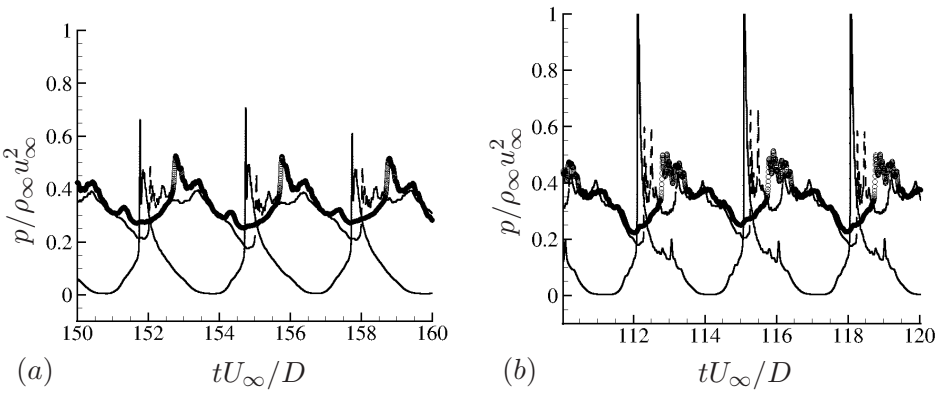

Figure 4.22: Pressure history at three different locations along wake center line for (a) $\alpha_0 = 0.01$ and (b) $\alpha_0 = 0.005$,—— : $x/D = 2.5$, ---- : $x/D = 5.0$, $\circ$: $x/D = 10.0$.

and the magnitude of the primary peak of the cycle is the same. However, the pressure wave impingement causes a higher pressure increase for $\alpha_0 = 0.005$ leading to a larger secondary peak as can be observed from the inset plot in Figure 4.21 (c). This implies that a stronger pressure wave is produced due to vapor collapse for $\alpha_0 = 0.005$ and this aspect is investigated further.

4.4.3 Pressure waves due to cavity collapse

To understand the effect of α_0 on pressure waves, pressure history at three different locations ($x/D = 2.5, 5.0$ and 10.0) along the wake center line is examined in Figure 4.22 for both the flows. There are adequate number of time samples (≈ 50) within each peak to resolve it accurately. Note that higher values for pressure peaks are obtained for $\alpha_0 = 0.005$. This change in pressure can be explained as follows. For an inviscid, isentropic flow, the pressure perturbation due to an acoustic wave is

$$p - \overline{p} = \overline{c}^2(\rho - \overline{\rho}) = \overline{\rho}\ \overline{c}^2\ S = Z\ \overline{c}\ S, \tag{4.2}$$

where $\overline{c}$ is the mean speed of sound, $Z \equiv \overline{\rho}\,\overline{c}$ is the acoustic impedance and $S \equiv (\rho - \overline{\rho})/\overline{\rho}$ is the condensation ratio. The time history of pressure perturbation scaled by $\overline{\rho}\ \overline{c}^2$ is shown in Figure 4.23(a) and (b) for both the cases. It can be observed that the

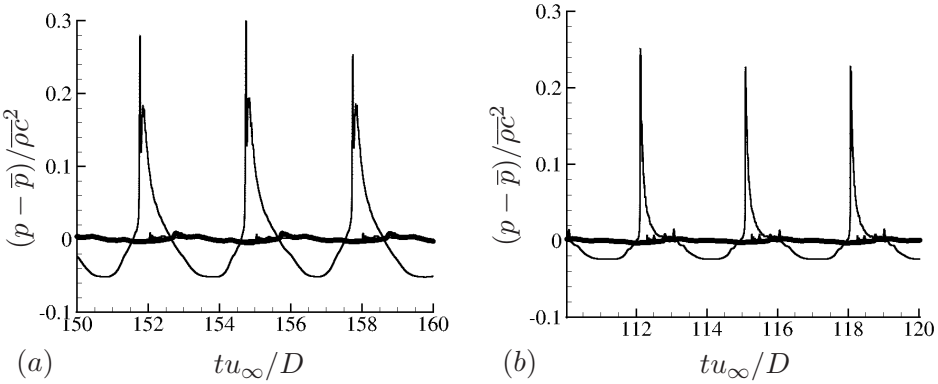

Figure 4.23: Change in condensation ratio along wake center line at three different locations along wake center line for (a) $\alpha_0 = 0.01$ and (b) $\alpha_0 = 0.005$, —— : $x/D = 2.5$, ---- : $x/D = 5.0$, $\circ$: $x/D = 10.0$.

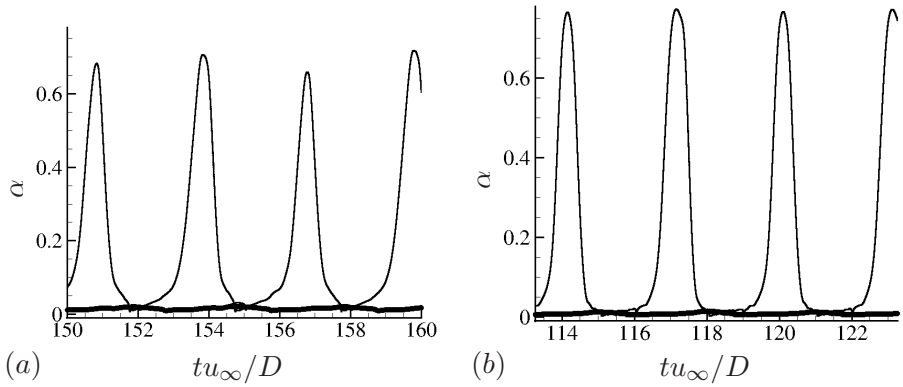

Figure 4.24: Time history of vapor volume fraction at three different locations along wake center line for (a) $\alpha_0 = 0.01$ and (b) $\alpha_0 = 0.005$, —— : $x/D = 2.5$, ---- : $x/D = 5.0$, $\circ$: $x/D = 10.0$.

Location (x/D)	**Initial void fraction** (α_0)	**Avg. condensation wave speed** (u_c/u_∞)	**Avg. sound speed** (c/u_∞)
$2.5 - 5.0$	0.01	8.3	8.0
$5.0 - 10$	0.01	6.8	7.0
$2.5 - 5.0$	0.005	17.0	18.0
$5.0 - 10$	0.005	10.0	9.5

Table 4.4: Average speed of pressure wave and sound speed.

peak values of the scaled pressure perturbation is similar for both the flows indicating similar values of condensation ratio S. To obtain the same condensation ratio in a less compressible medium (higher Z and $\bar{c}$), a higher pressure rise would be required explaining the larger pressure peaks for $\alpha_0 = 0.005$. Thus the major consequence of changing α_0 seems to be in producing a pressure wave that has higher pressure rise across it, but produces the same amount of density change in the medium. The similarity in S for both α_0 can be explained using Figure 4.24, that shows vapor volume fraction history corresponding to the pressure history in Figures 4.22 and 4.23. The vapor volume fraction drops from a value of about 0.6 to the free stream value corresponding to the time instant where pressure spike occurs in Figure 4.22. Since the free stream values are at least an order of magnitude lesser (0.01 and 0.005) than 0.6, the change in vapor volume fraction produced is almost the same for both the flows, which explains the density change also being similar for both the flows.

The difference in the average speed of a pressure wave as it travels between two points can also be observed from Figure 4.22. Waves move faster when $\alpha_0 = 0.005$ due to the higher speed of sound. The average speed of the pressure wave is computed and tabulated along with average speed of sound in Table 4.4. To compute these quantities it is assumed that the speed does not change between the probe locations. Although this assumption is not strictly valid, it gives a sense of the propagation speed of the pressure waves with respect to sound speed (c). It is observed that the pressure waves travel almost at the local speed of the sound in the medium.

Pressure fluctuation levels of the two flows are compared to the pressure fluctuations in a non–cavitating flow in Figure 4.25. The difference in the contours downstream of

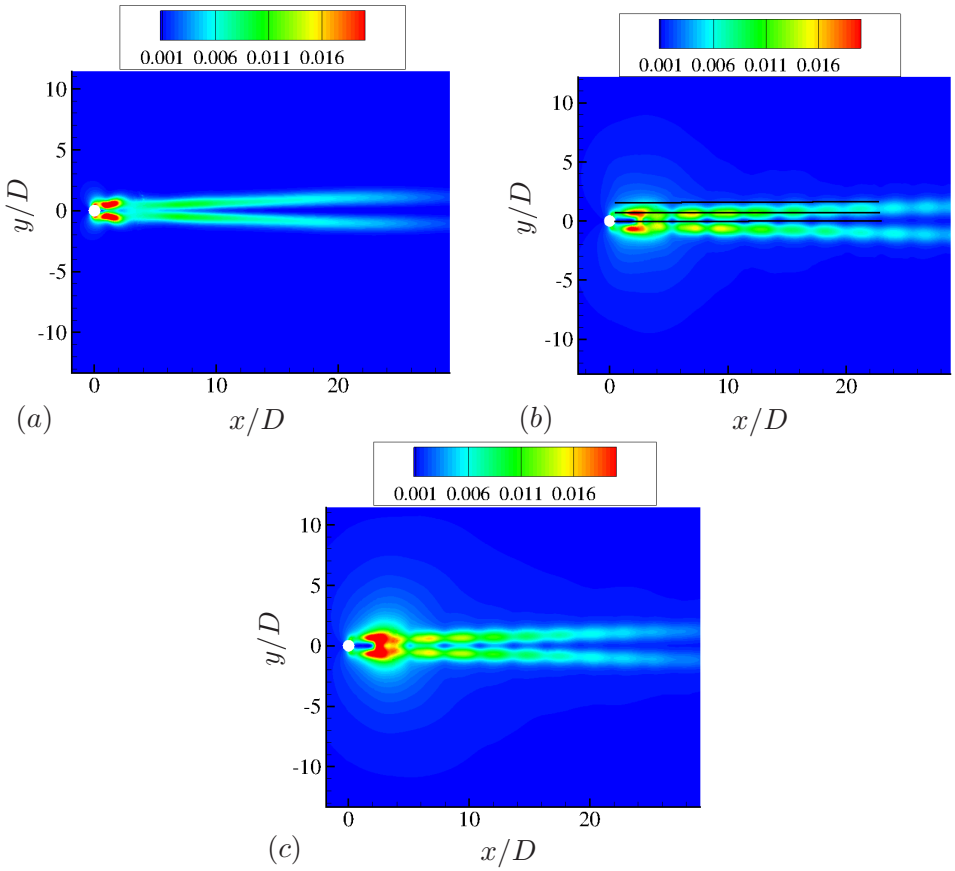

Figure 4.25: Comparison of pressure fluctuation ($\overline{p'^2}$) contours for (a) Non–cavitating flow, (b) $\alpha_0 = 0.01$ and (c) $\alpha_0 = 0.005$.

the cylinder on either side of the centerline is evident. The 'cell' shaped structures formed in the cavitating cases ((b) and (c)) are due to the pressure fluctuations caused by the pressure waves due to cavity collapse, which are absent in a single phase flow. The structures are localized in space due to the fact that the pressure wave impinges with the vortices only at specific points in space. This interaction causes the residual vapor in the vortex core to collapse leading to a momentary increase in pressure followed by a recovery back to a lower pressure due to the rotation of the vortices. Since this happens until the pressure waves decay and the vapor in the vortices are destroyed completely, a train of 'cell' shaped structures can be observed until about $20D$. Such behavior would be absent if the wake only had advecting vortices or propagating pressure waves: it is a result of their interaction. Figure 4.26 shows the variation of pressure fluctuations along the streamwise direction at three different y locations as marked in Figure 4.25 (b) for both the cavitating flows. Both the wake center line plot ($y/D = 0.0$) and the cut through the vortex core ($y/D = 0.7$) shows several cycles of cavity growth and collapse, and in each cycle, the crest corresponds to the collapse of bubble and each trough is the cavity at its maximum regrown state. The absence of vapor in at $y/D = 2.0$ means that pressure fluctuation change is not as substantial as inside the vortices. The propagation speed of the wave is also different and can be observed from the figure. Owing to larger speed of sound, the pressure wave for $\alpha_0 = 0.005$ travels faster and impinges with the vortex at an upstream location than in the $\alpha_0 = 0.01$ flow.

4.5 LES of Turbulent cavitating flow at $Re = 3900$

LES of turbulent cavitating flow at $Re = 3900$ and $\alpha_0 = 0.01$ is performed. The topology used for the simulation is similar to the lower Reynolds number cases; the grid however is three dimensional and more refined in the near wake. The averaged statistics are obtained over 10 shedding cycles and satisfactory convergence is obtained in the near wake region. The number of samples are further increased by averaging along the spanwise direction and also about the wake center line to improve convergence. Figure 4.27 shows the instantaneous vortical structures in the form of Q-criterion colored by

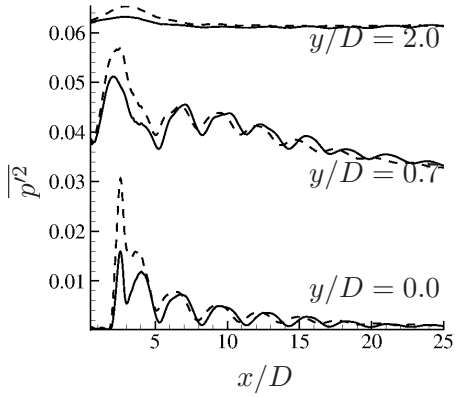

Figure 4.26: Comparison of pressure fluctuations as a function of downstream distance at three different locations in the wake, —— : $\alpha_0 = 0.01$, ---- : $\alpha_0 = 0.005$. The curves at $y/D = 0.7$ and $y/D = 2.0$ have been shifted along the y-axis by 0.03 and 0.06 respectively.

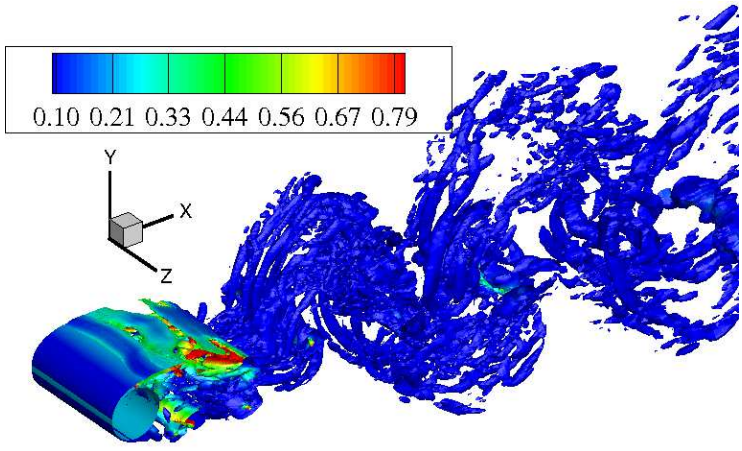

Figure 4.27: Isocontours of Q = 2 colored by void fraction.

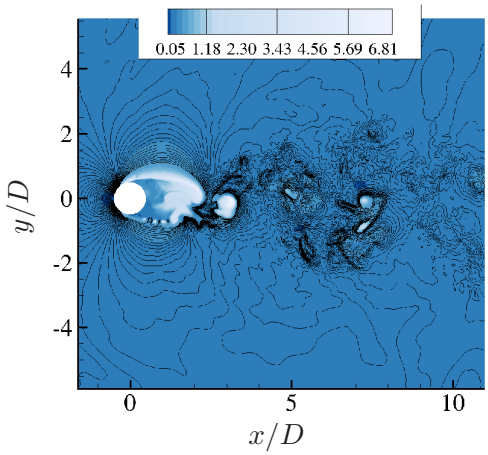

Figure 4.28: Instantaneous Mach number contours superimposed with lines of pressure.

void fraction. Three dimensional flow structures of varying scales can be observed. The shear layer breaks up into smaller spanwise structures. The flow structures in the near wake, especially in the vapor cavity appear to be larger when compared to the flow structures observed by Verma and Mahesh [9] (Figure 16 in their paper) in the single phase flow. This is because of the effective lowering of Reynolds number by the presence of vapor. Further, small vapor pockets can be seen trapped in the smaller scale vortices downstream of the wake. Although the flow is three–dimensional inside the vapor cavity immediately downstream, breakdown to finer scales occurs downstream of the cavity closure. Figure 4.28 shows instantaneous contours of Mach number showing supersonic Mach numbers in the shear layer. Cavitation in wake vortices also causes locally supersonic Mach numbers there. The contour lines of pressure shows distorted fronts of pressure waves. Turbulence causes different points in the wave fronts to have different speeds resulting in their distortion.

4.5.1 Comparison of $Re = 3900$ cavitating flow to $Re = 200$ cavitating flow

Figure 4.29 compares the mean void fraction for $Re = 3900$ to the $Re = 200$ flow. There are minor differences in the cavity shape; the major change however is the fact

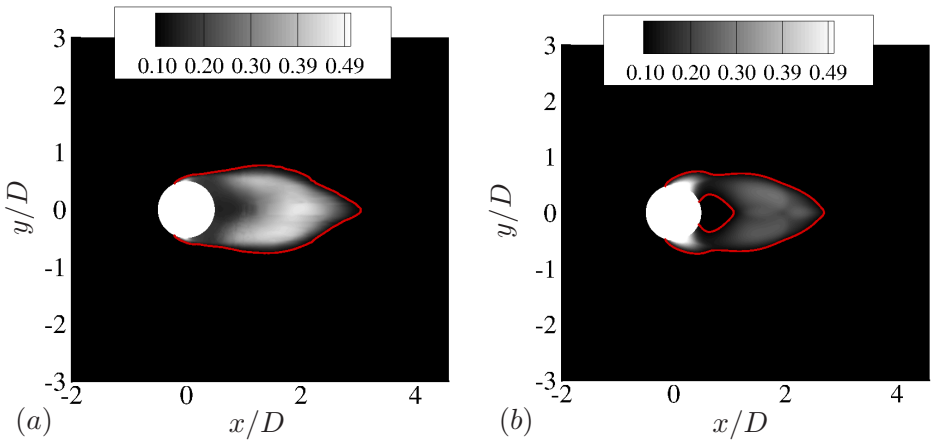

Figure 4.29: Mean void fraction contours for (a) $Re = 3900$ and (b) $Re = 200$.

that vapor is distributed uniformly in the wake for the turbulent case as opposed to only in the vortices for the laminar case. The length of the cavity (l_{cav}/D) is 3.04 for the high Reynolds number flow, while it is only 2.71 for the low Reynolds number flow. Also note the presence of larger fraction of vapor in the wake for $Re = 3900$. Thus increasing Reynolds number at the same cavitation number makes the flow cavitate more resulting in a larger cavity dimension. This observation is also in line with that of Rao and Chandrasekhara [8]. The presence of increased amount of vapor also affects the C_p and C_f distribution. Figures 4.30 (a) and (b) compare the time averaged C_p and C_f distribution of $Re = 3900$ at $\sigma = 1.0$ with the $Re = 200$ flow at the same cavitation number. Also shown in the figure are the C_p and C_f distribution from the single phase flow at $Re = 3900$ which will be discussed in Section 4.5.2. When compared to the $Re = 200$ flow, the minimum C_p location is shifted upstream pointing to the inception location moving upstream. The magnitude of the minimum C_p is also reduced in the $Re = 3900$ flow which is also consistent with the increased amount of vapor. The C_f curve for the $Re = 3900$ flow in Figure 4.30 (b) shows a different behaviour when compared to the $Re = 200$ flow. The main difference is that there is a marked difference in the inflection point in the C_f curve. This is due to the fact that the deceleration upstream of inception location and acceleration downstream of inception caused by cavitation explained in Section 4.3.3 is subdued at $Re = 3900$ when compared

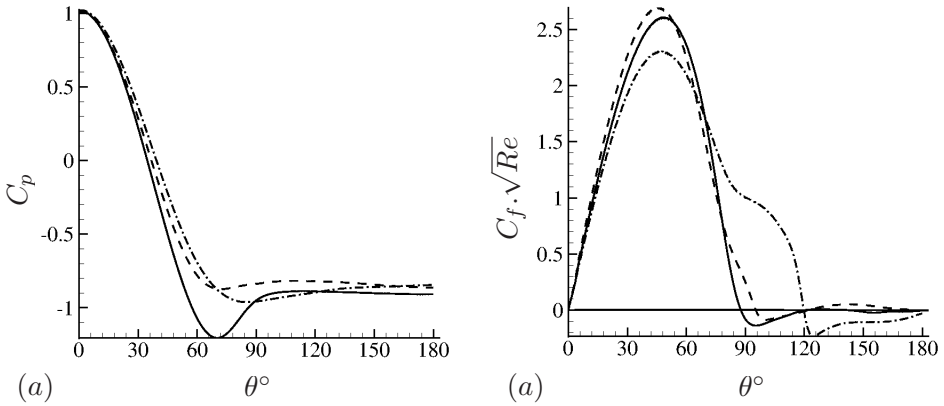

Figure 4.30: (a) Time averaged C_p distribution along the cylinder. (b) Time averaged C_f distribution along the cylinder, ——— : $Re = 3900$ single phase flow, - - - - : $Re = 3900$ cavitating flow and $-\cdot-\cdot-$: $Re = 200$ cavitating flow.

to $Re = 200$ due to three dimensional effects. This also results in the separation location to be shifted upstream (95°) for the $Re = 3900$ flow since the acceleration effect present in the $Re = 200$ flow is now reduced.

The mean boundary layer evolution of the high Reynolds number flow is compared with the low Reynolds number flow in Figure 4.31. At an azimuthal location of 70°, the $Re = 3900$ flow has a higher magnitude for maximum velocity which is consistent with the reduced amount of deceleration due to cavitation inception. Further, the location of maximum velocity is also shifted closer to the wall for the $Re = 3900$ flow. The maximum velocity at 90° is lower for $Re = 3900$ since the flow is closer to the separation point and is decelerating much more than the $Re = 200$ flow at the same location. The flow separates at about 95° and instances of separated flow can be observed at the downstream locations.

The lift and drag history and their power spectral density are plotted in Figure 4.32. The secondary peaks due to pressure wave impingement are not as prominent as they were in the $Re = 200$ flow. The presence of increased amount of vapor in the wake presumably reduces the effect of pressure wave impingement. The Strouhal number corresponding to vortex shedding frequency is 0.167 and the reason for the Strouhal number reduction from the single phase value of 0.2 is very similar to that of the $2D$

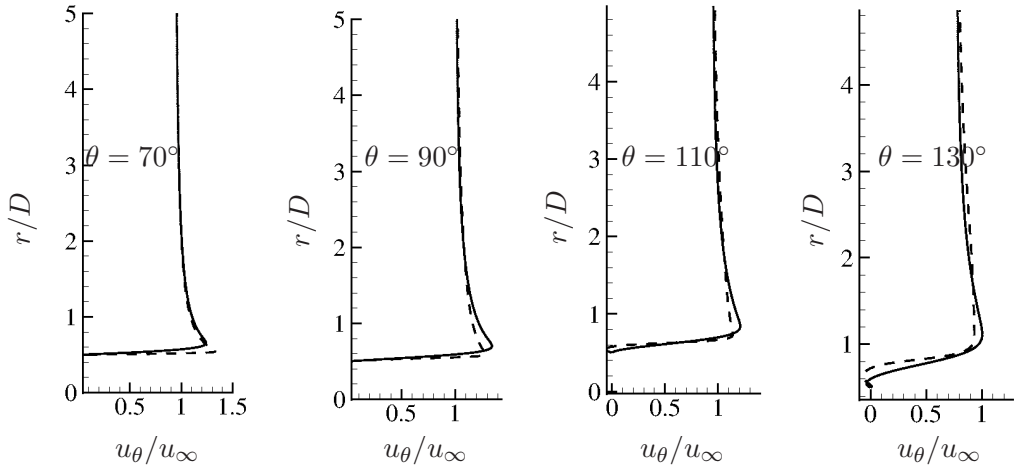

Figure 4.31: Boundary layer profile at four azimuthal locations, —— : $Re = 200$ and ---- : $Re = 3900$.

flow and is depicted in Figures 4.33 (a) and (b). The mean velocity divergence contours show an expansion region corresponding to vapor formation. A compression region is found immediately downstream of the expansion similar to the $Re = 200$ flow. The expansion region causes vorticity dilatation the can be observed in Figure 4.33 (b). As in the $Re = 200$ flow, this vorticity dilatation is the main reason for the vorticity reduction which reduces the vortex shedding frequency.

4.5.2 Comparison of $Re = 3900$ cavitating flow to $Re = 3900$ non–cavitating flow

Figures 4.32 (a) and (b) also compare the C_p and C_f distribution of $Re = 3900$ cavitating flow with that of single phase results of Verma and Mahesh [9] at the same Reynolds number. Cavitation decreases the magnitude of minimum C_p when compared to the single phase C_p and the flattening of C_p curve is due to the presence of vapor, similar to the discussion in Section 4.3.1. The C_f curve comparison shows that the separation location is shifted downstream compared to the single phase flow. The reason for this shift is same as that discussed in Section 4.3.3.

Figures 4.34 and 4.35 compare the mean velocity profiles and turbulence intensity profiles respectively in the wake for the cavitating case at $Re = 3900$ to the single

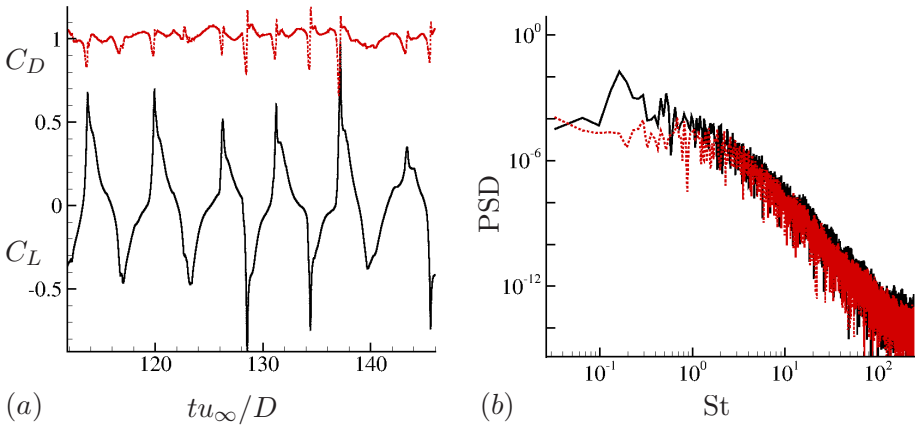

Figure 4.32: (a) Lift and Drag coefficient history, (b) Power spectral density, —— : C_L, ---- : C_D.

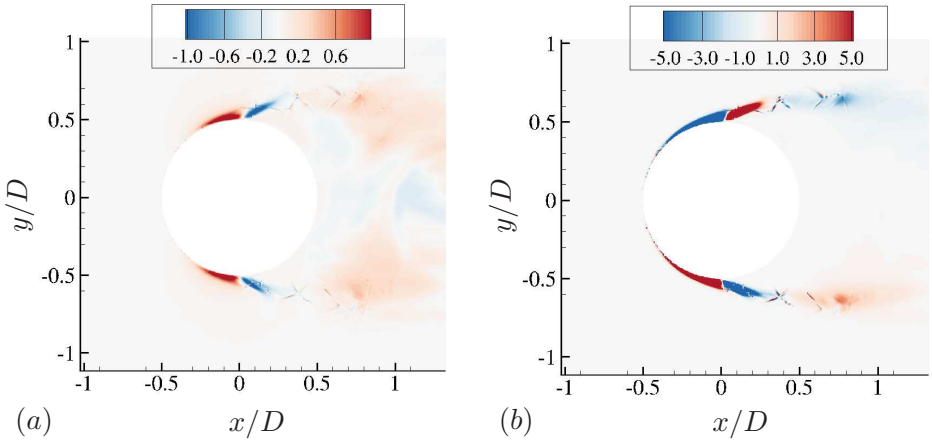

Figure 4.33: (a) Mean divergence contours. (b) Mean vorticity dilatation contours.

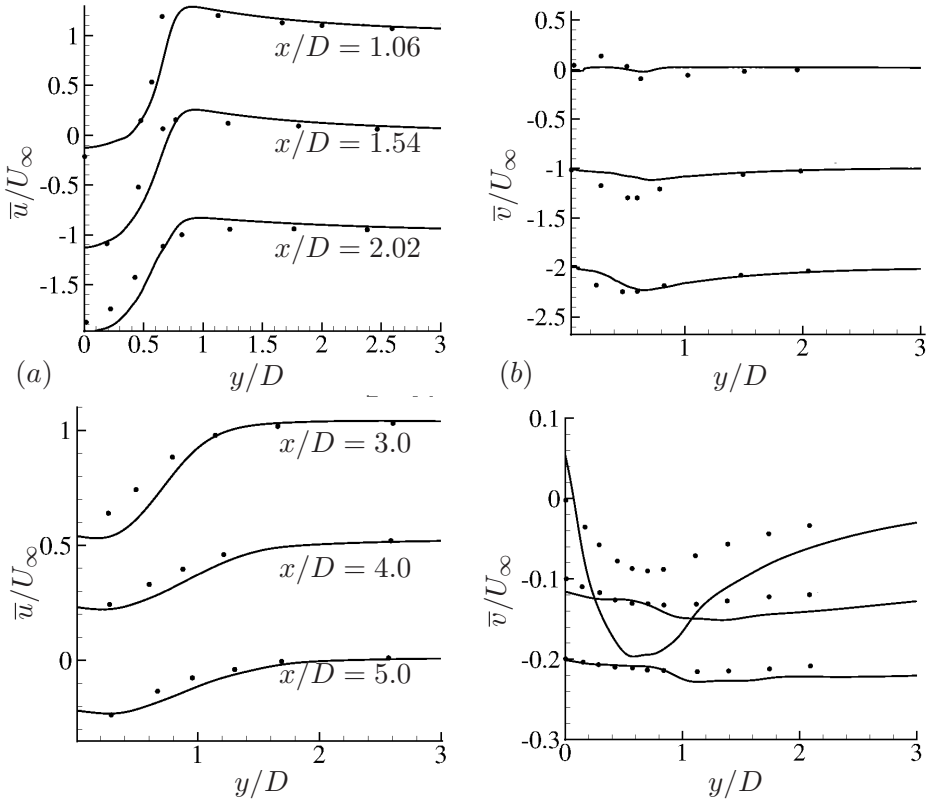

Figure 4.34: Comparison of vertical profiles at streamwise stations downstream of the cylinder at $Re = 3900$, • : Verma and Mahesh [9], —— : Present.

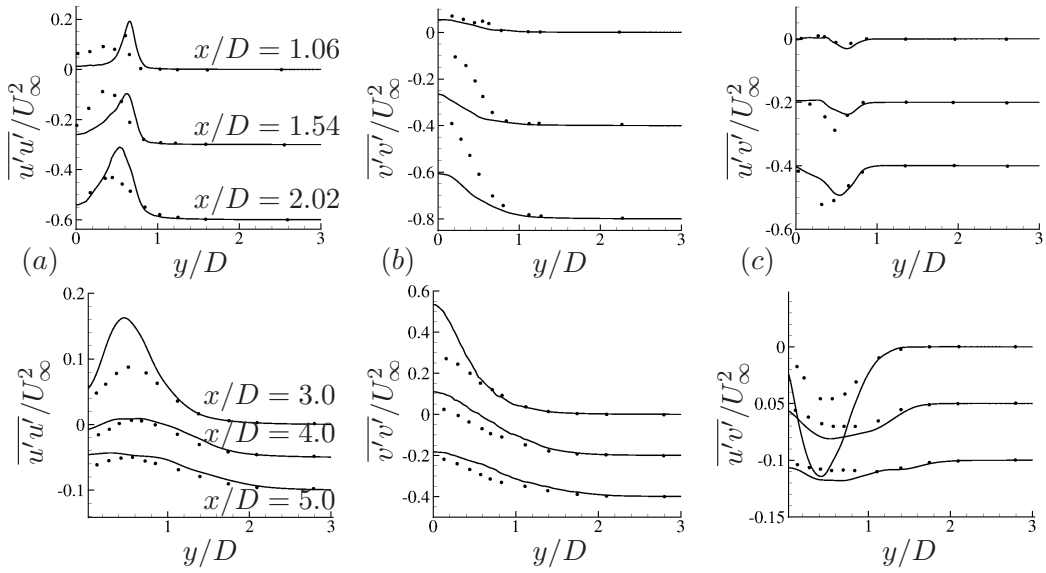

Figure 4.35: Comparison of vertical profiles at streamwise stations downstream of the cylinder at $Re = 3900$, • : Verma and Mahesh [9], —— : Present.

phase results of Verma and Mahesh [9] at the same Reynolds number. The streamwise velocity profiles at all stations show a wider wake profile for the cavitating flow. The station $x/D = 3.0$ shows the maximum difference in the vertical velocity profile since it corresponds to the cavity closure region. Inside the cavity (except at $x/D = 1.06$), larger values of vertical velocity are obtained. The maximum value for $\overline{u'u'}$ occurs downstream ($x/D = 3.0$) pointing to a larger formation length. Inside the cavity, the values for $\overline{v'v'}$ are much smaller than those obtained for the single phase flow. However the cavity closure at $x/D = 3.0$ is highly unsteady with higher fluctuation values in both streamwise and vertical velocity. The $\overline{u'v'}$ curve shows a similar trend to the mean vertical velocity profiles. Overall, cavitation seems to have delayed the complete three dimensional breakdown of the Karman vortices by effectively lowering the Reynolds number in the wake. This fact is corroborated in Figure 4.36 which shows the instantaneous magnitude of vortex stretching in the symmetry plane for the multi phase and single phase flows. Note that the vortex stretching magnitude in the wake is reduced in a cavitating flow. Hence formation of vapor suppresses turbulence, yielding highly correlated span–wise structures in the near wake in Figure 4.27.

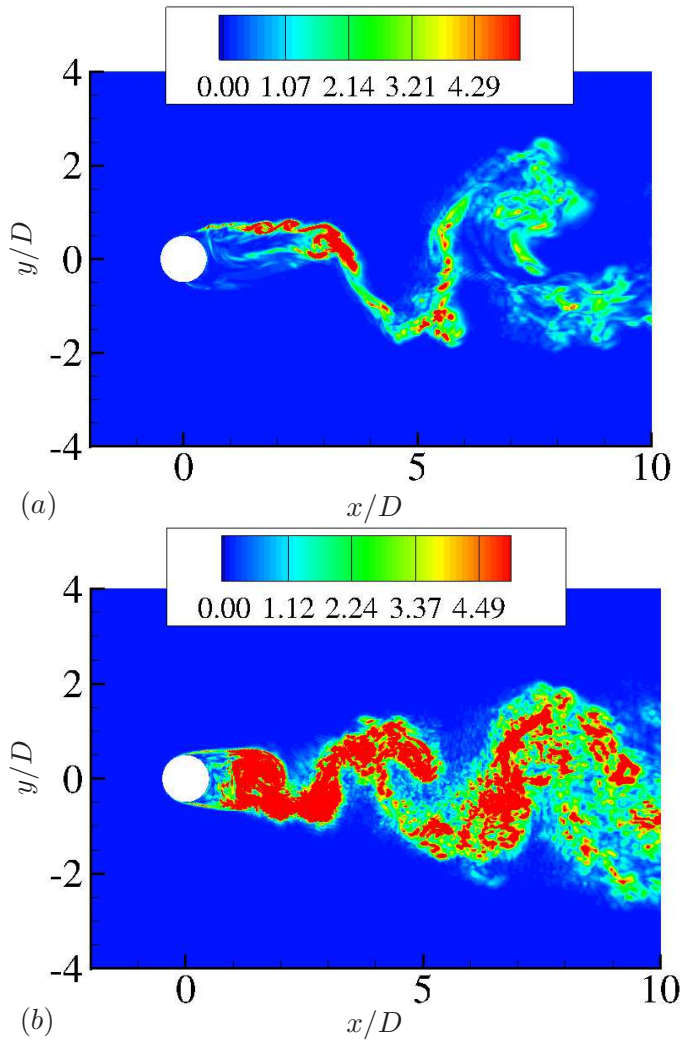

Figure 4.36: Magnitude of vortex stretching in the symmetry plane for (a) Cavitating flow (b) Non–cavitating flow.

Chapter 5

Transition of sheet to cloud cavitation over a wedge

5.1 Introduction

Sheet cavitation and its transition to cloud cavitation is of great practical interest since the highly unsteady flow can induce significant fluctuations in the thrust and torque of marine propellers. The collapse of the cloud also causes material damage to the blades. Several experiments have been conducted to understand the sheet to cloud transition mechanism. Arndt et al. [26] studied a NACA 0015 hydrofoil and observed two types of behavior based on the parameter $\frac{\sigma}{2\alpha}$, where σ is the cavitation number and α is the angle of attack. They concluded that a re-entering jet was responsible for cavity destabilization for $\frac{\sigma}{2\alpha} > 4$, while at lower values, a bubbly shock dominates the flow. More recently, Ganesh [10] performed experiments on a wedge and also concluded that at lower cavitation numbers a propagating shock wave is the dominant mechanism that causes periodic shedding; they term this regime 'periodic cavitation'. At slightly larger cavitation numbers, they observe intermittent cloud shedding and term this 'transitory cavitation'. In this regime, they observe that re–entering jet is dominant during earlier stages and a propagating shock wave is dominant during later stages of the experimental cycle. Leroux et al. [49] observed a quasi stable partial sheet cavity on a hydrofoil for

cavity lengths less than half the chord length and sheet to cloud cavitation for lengths greater than half the chord length. They also agreed with the conclusions of Arndt et al. [26] but modified the parameter to be $\frac{\sigma}{2(\alpha - \alpha_0)}$, where α_0 is zero for symmetric hydrofoils. Stutz and Reboud [79] measured local void fraction inside the cavity formed on a wedge and confirmed the presence of a re–entering jet along the wall. Experiments by Pham et al. [80] also showed the role of re–entering jet in cloud formation on a hydrofoil. Kawanami et al. [81] showed that a small obstacle in the path of the re–entering jet was able to prevent the formation of cloud cavity and thus conclusively proved the role of re-entering jet in producing the cloud. Interestingly though, Ganesh [10] also placed an obstacle inside the cavity and showed that it did not prevent the formation of a cloud cavity. Their experiments show the considerable significance of the propagating discontinuity which exists not only close to the wall but spans the entire thickness of the cavity. Callenaere et al. [82] established the importance of an adverse pressure gradient at the cavity closure for the formation of a re-entering jet. They observed two types of cavity, thick and thin based on the amount of interaction between the re-entering jet and the cavity interface. For thick cavities, the interaction between the re-entering jet and the cavity is minimum until the re-entering jet reaches the leading edge of the cavity, giving rise to the classical sheet to cloud transition. On the other hand in a thin cavity, the interaction with re-entering jet causes the cavity to split into many small structures. In this case, although the cavity does not auto–oscillate, the re-entering jet is still periodic with a Strouhal number in the range 0.2 - 0.4. Laberteaux and Ceccio [50] further classified cavities as open and closed based on the absence and presence of re-entering jet respectively. A closed cavity has a clear interface and a re-entering jet is often found, whereas an open cavity is typically frothy with no clear re-entering jet.

Most computational studies of sheet to cloud cavitation have employed the homogeneous mixture model [53] where the multiphase fluid mixture is treated as a single compressible fluid. The major difference between the several studies using this model lies in the equation of state of the mixture, and the mass transfer model that governs the rate of evaporation and condensation. A comparative study of various mass

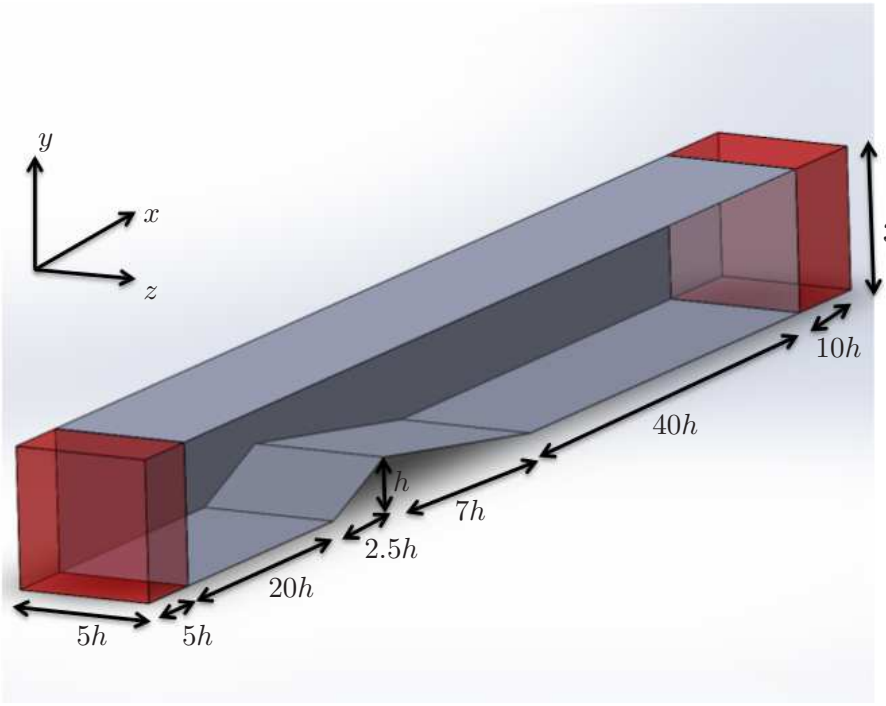

Figure 5.1: Schematic of the computational domain (Not to scale).

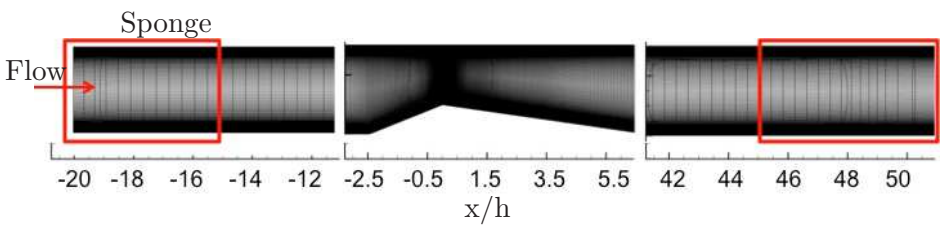

Figure 5.2: $2D$ slice of the computational domain showing the mesh.

transfer models can be found in [25, 83]. A number of studies have used the homogeneous mixture assumption to study cavitation over two–dimensional geometries (e.g. [21, 23, 54, 84, 85]), and three-dimensional geometries with variation in the span and sidewalls (e.g. [18, 20, 86, 87]) Most of the above studies used RANS to model the turbulence. However, RANS models need an ad–hoc suppression of eddy viscosity in order to predict sheet to cloud cavitation (see e.g. [54]). Recently, LES has been considered since it can predict flow unsteadiness better without ad–hoc modifications (e.g. [27, 28, 31, 43, 88]). The various LES studies differ in their detail. Bensow and Bark [27] used an incompressible segregated method using a pressure Poisson equation to predict cavitation over a hydrofoil and concluded that the discrepancy in the cavity length predicted by their method could be a result of the incompressible method. Dittakavi et al. [28] used a fully compressible Favre–filtered algorithm for simulating cavitating flow over a wedge; however they artificially modified the sound speed to reduce the stiffness of the system. This method predicts the general dynamics of sheet to cloud cavitation well, however the frequencies predicted by this are not accurate. Huang et al. [89] also used a compressible method to simulate sheet to cloud cavitation over a hydrofoil and found that their method over predicts the vapor volume fraction inside the cavity and this contributed to the discrepancy in the velocity and vorticity field. Arndt et al. [90] used a weakly compressible approach to perform LES of sheet to cloud cavitation over a NACA hydrofoil and studied the large scale structures produced in the wake of the hydrofoil. However, they specify an arbitrary Mach number in the liquid to accelerate their computation. They justify this in their study by saying that their primary interest is to study hydrodynamic quantities and not acoustic quantities. Yu et al. [91] used a $k - \mu$ SGS model to perform LES of sheet to cloud cavitation over a hydrofoil and

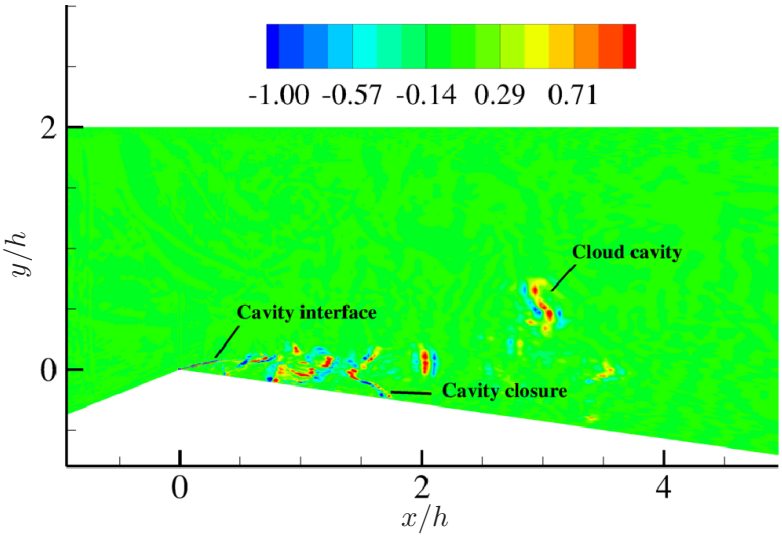

Figure 5.3: Dissipative flux showing localization near cavity interface, closure and inside cloud cavity.

obtained good comparison for the re–entering jet velocity. However the cavity length predicted by their method differs significantly from the experimental values. The studies of Wang and Ostoja-Starzewski [31] and Ji et al. [88] also used compressible LES to study cavitation over hydrofoil. Few past LES studies have shown satisfactory quantitative comparisons for void fraction. In this study, we quantitatively compare the length of the cavity, Strouhal number corresponding to cavity auto–oscillation and void fraction profiles inside the cavity with the experiments of Ganesh [10].

5.2 Problem Description

Figure 5.1 shows a schematic of the computational domain. The mean flow is along the $x - axis$ and the wedge apex is located at the origin. The height of the wedge is $h = 1\ inch$. The computational domain is extended in both upstream ($25h$) and downstream directions ($50h$) to minimize the effect of acoustic reflection from the boundaries. Velocity and pressure are prescribed at the inlet and downstream pressure is prescribed at the outlet. The boundary conditions are iteratively changed in order to match the average cavitation number obtained from the experiment at the $y - z$ plane located at

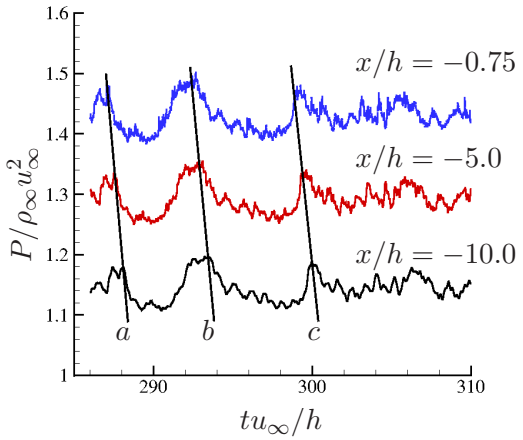

Figure 5.4: Pressure history upstream of the wedge showing the effect of non–reflecting boundary conditions.

$x/h = -3.25$ just before the converging section starts. No slip boundary conditions are imposed on top and bottom walls. Periodic boundary conditions are enforced at the spanwise boundaries. Acoustically absorbing boundary conditions [78] are applied in sponge layers at both inlet and outlet as shown in Figure 5.1. The term $-\gamma(\vec{q} - \vec{q}_{ref})$ is added to the governing equations, where γ is zero outside the sponge layer, $\vec{q}$ denotes the vector of conservative variables and the subscript 'ref' denotes the reference solution to which the flow inside the sponge layer is damped. Velocity and pressure at the inlet sponge are damped to the inlet values, while only the thermodynamic variables are damped to the downstream value at the outlet. The Reynolds number of the flow based on the wedge height ($h = 1$ *inch*) and a bulk velocity of 7.9 m/s is approximately 0.2×10^6.

The computational mesh at the inlet, outlet and test sections are shown in Figure 5.2. The mesh is made very fine near the wedge apex and along the entire length of the wedge where the major portion of the vapor is expected to form. The minimum grid spacing near the wedge is $0.001h\times$ $0.001h\times$ 0.01h in the wall normal, streamwise and spanwise directions respectively. The wall normal spacing stretches to $0.005h$ at a height of $0.5h$ from the wedge apex and further to about $0.01h$ at a height of h from the apex. In the streamwise direction, the grid is stretched to $0.02h$ at a distance

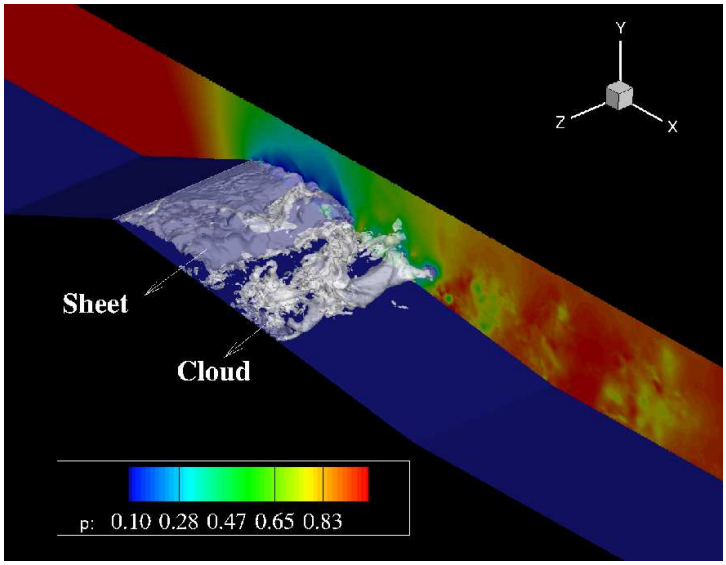

(*a*)

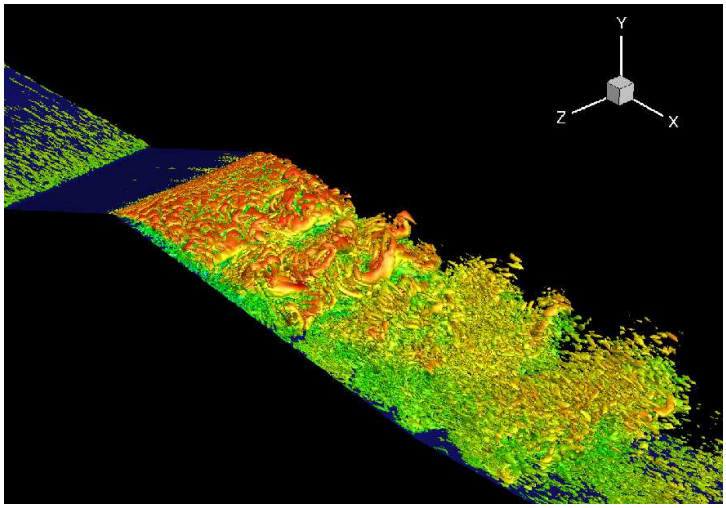

(*b*)

Figure 5.5: (*a*) Instantaneous void fraction contours showing sheet and cloud cavities, (*b*) Isocontours of Q-criterion showing vortical structures.

$3.5h$ from the apex and further to $0.01h$ at the end of the wedge. The total number of control volumes is approximately 45 million. The non–dimensional time step used in the simulation is $tu_\infty/h = 1 \times 10^{-5}$. The simulation is initialized using a two dimensional solution obtained from a RANS simulation performed using Spalart–Allmaras model [51] under the same conditions prescribed for the LES simulation. The cavitation number obtained in the experiments at $x/h = -3.25$ is 2.0 and that in the simulation is 2.1. The cavitation number obtained in simulation is using a pressure of 69 KPa and a velocity of 7.9 m/s while the corresponding values in the experiments are 66 KPa and 8 m/s.

Localization of dissipation is essential to accurately simulate turbulent flows. To assess this effect, the filter flux $\frac{F^*_{fc}}{V_{cv}}$ is computed and plotted in Figure 5.3 for the continuity equation, where $F^*_{fc} = \frac{1}{2}R_{fc}\Phi^*_{fc}$ as defined in Section 2.3.4. From Figure 5.3, it can be observed that the dissipation is significant only at the cavity interface, cavity closure and inside the cloud cavity. The dissipative fluxes for other equations also show similar behavior and hence are not shown here. In order to illustrate that pressure waves traveling towards inlet are not reflected back into the domain, we plot time history of pressure at three different locations upstream of the wedge in Figure 5.4. The major pressure rise events tagged as a, b and c indicate that the direction of pressure waves is towards the inlet and that no waves are reflected back into the domain.

5.3 Results

The nature of the instantaneous solution is illustrated using isocontours of void fraction in Figure 5.5(a) which shows the presence of both sheet and cloud cavities. The flow accelerates in the converging portion and the instantaneous pressure drops below vapor pressure at the wedge apex which results in cavitation. The cavity then grows along the flow direction and on reaching a critical length, breaks into a cloud. This cloud is highly three dimensional and it is the collapse of this cloud that causes noise, vibration and surface erosion. The vertical plane in Figure 5.5(a) shows pressure contours. It can be observed that pressure exhibits both wave–like behavior (close to leading edge of the cavity) and highly intermittent behavior (downstream of the cloud). The turbulent

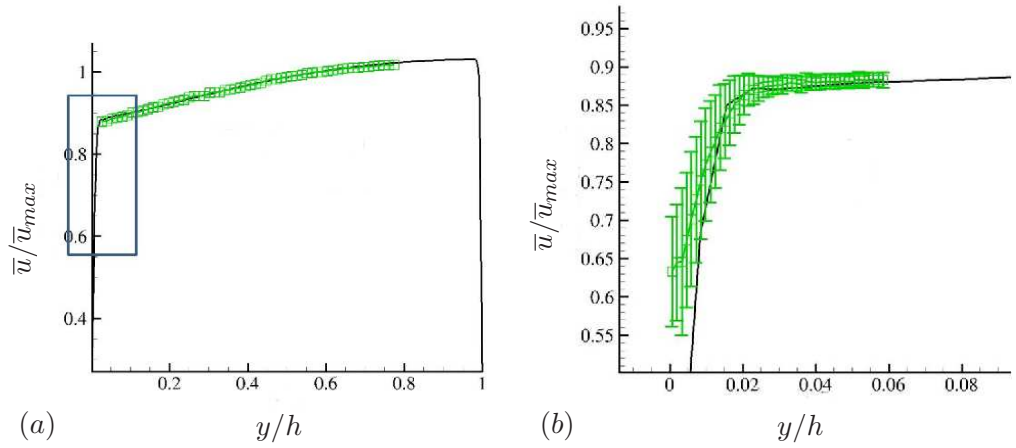

Figure 5.6: Mean velocity comparison at wedge inlet $x/h = -3.25$, —— : LES , —— : Experiment ([10]). (b) shows the close–up view of near wall region as illustrated in (a).

nature of the flow downstream prevents a coherent wave–like behavior there, since turbulence breaks up the wave thus causing highly intermittent pressure fluctuations. The pressure waves produced on cavity collapse impinges on the growing sheet cavity and affects its growth significantly. Figure 5.5(b) shows isocontours of Q-criterion colored with streamwise velocity. The intensely vortical nature of the flow and wide range of length scales are apparent in both sheet and cloud regions. The presence of sheet and cloud is also evident from the vortical structures in the flow, where the sheet cavity has larger structures due to its relatively two–dimensional nature while the cloud has both large and small structures. Note that the vorticity in the cloud persists even after the cloud collapses.

5.3.1 Comparison to experiment

We compare the mean inlet velocity profile, mean and RMS void fraction and the Strouhal number corresponding to cavity auto–oscillation. The averaged statistics presented in this section are obtained by performing a time average over 40 th/u_∞ and has approximately 30,000 samples. The separation between the samples is 0.001 th/u_∞

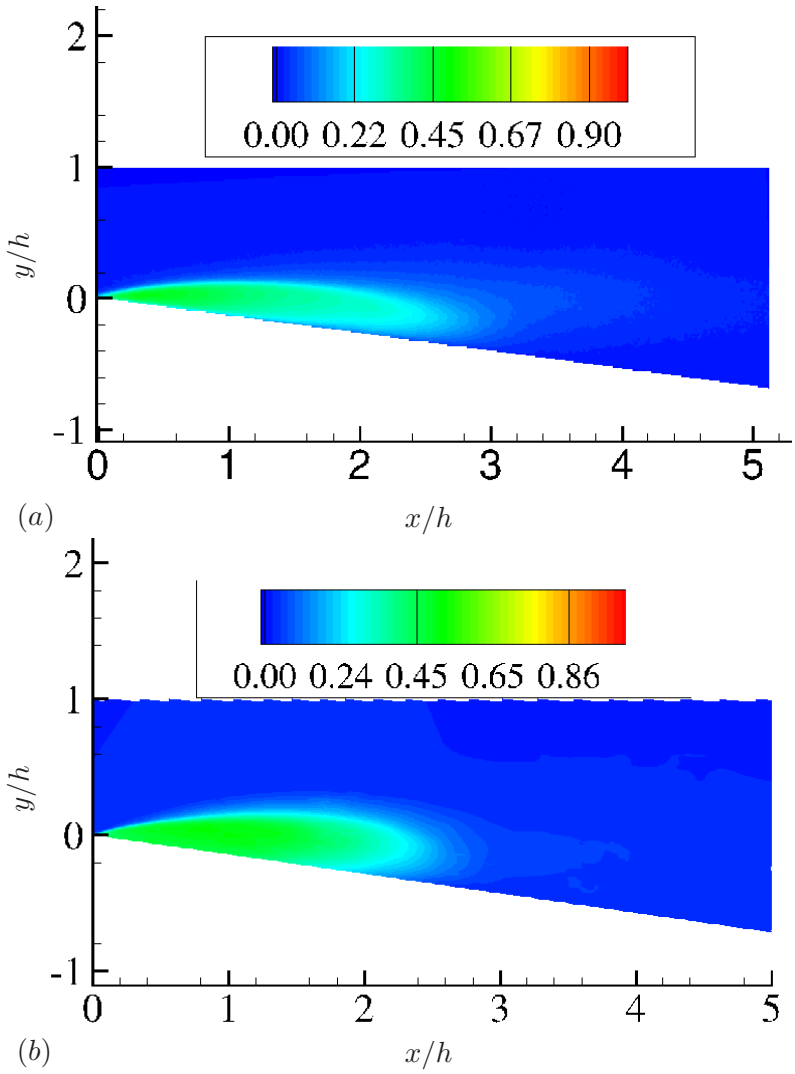

Figure 5.7: Comparison of mean void fraction contours, (a) Experiment (b) LES.

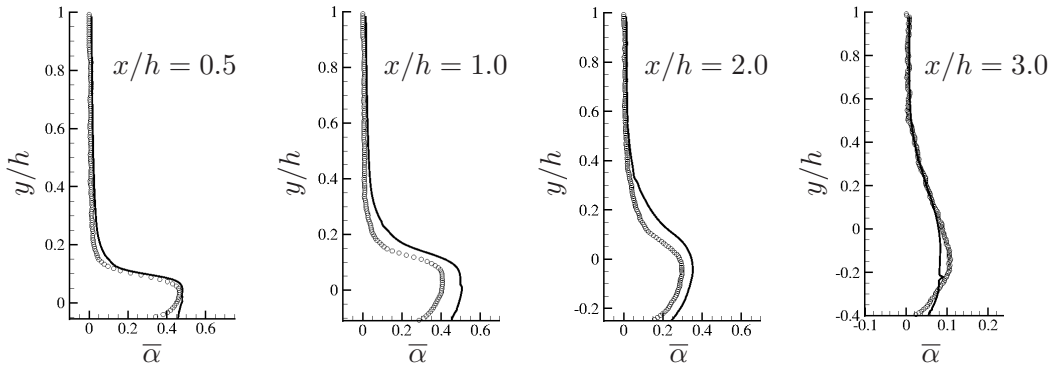

Figure 5.8: Comparison of mean void fraction profiles at different streamwise locations, ∘ : Experiment, —— : LES.

which captures all relevant high frequencies. The time averaged results are then averaged along the spanwise direction to further improve convergence of the statistics. The mean inlet velocity profile obtained from the simulation is first compared to the experiment to ensure that the oncoming velocity profile to the wedge is predicted properly. Figure 5.6(a) shows the overall comparison obtained between simulation and experiments and Figure 5.6(b) shows a close–up view of the velocity profile near the bottom wall. Overall good agreement is obtained. Figure 5.7 compares the mean void fraction contours obtained from experiment and simulation. Note the overall good agreement of the cavity length and the value of mean void fraction inside the cavity. The cavity thickness predicted by the simulation is slightly larger than the experimental measurement. The mean void fraction at different streamwise locations on the wedge are compared to the experimental results in Figure 5.8. The agreement for the mean void fraction is very good at $x/h = 0.5$ and $x/h = 3.0$ stations, while LES slightly over–predicts void fraction at the other two stations. No error bars are available from experiment for mean void fraction data. Next we compare the RMS of void fraction obtained from simulation and experiment in Figure 5.9. Note that error bars are not available from the experiment for this quantity either, and that only the resolved portion of the fluctuation obtained from LES is shown here. The free stream fluctuation measured in the experiment does not go to zero while that predicted by LES goes to zero away from the cavity. The qualitative trend from LES agrees well with the experiment at all the stations. The fact

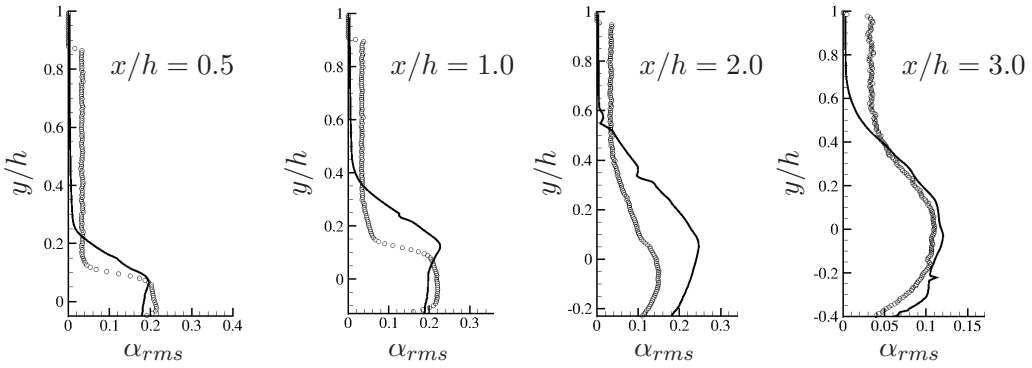

Figure 5.9: Comparison of RMS of void fraction profiles at different streamwise locations, ∘ : Experiment, —— : LES.

that LES predicts a thicker cavity is also manifested in the form of higher magnitude of fluctuations away from the wedge. Overall, the comparisons for void fraction data are encouraging suggesting the suitability of LES in predicting this highly unsteady phenomenon. The Strouhal number corresponding to shedding frequency obtained from the numerical simulation is $St = 0.28$, which is computed from the time histories of pressure and void fraction at several locations inside and downstream of the mean cavity and will be discussed in Section 5.3.3. This value lies within the range of 0.25-0.3 obtained by the experiment.

5.3.2 Mean pressure, density and velocity field

Figure 5.10(a) shows the variation of mean velocity and pressure along a streamline at $y/h = 1$. The flow accelerates in the converging portion (upto $x/h = 0$) and pressure drops correspondingly. The presence of the cavity accelerates the free stream flow further due to the confining effect of the wall, upto about $x/h = 1.5$ after which the flow decelerates. Also shown in the figure is $\overline{p} + 0.5\overline{\rho}\ \overline{u}^2$, which remains nearly constant showing that the viscous effects are confined close to the wall. The mean streamlines (Figure 5.10(b)) show a reverse flow region which corresponds to the cavity location. The separation streamline that separates the reverse flow inside the cavity from the flow outside the cavity stagnates at the cavity closure. The adverse pressure gradient at this closure location causes a reverse flow to penetrate the cavity, which contributes to cloud

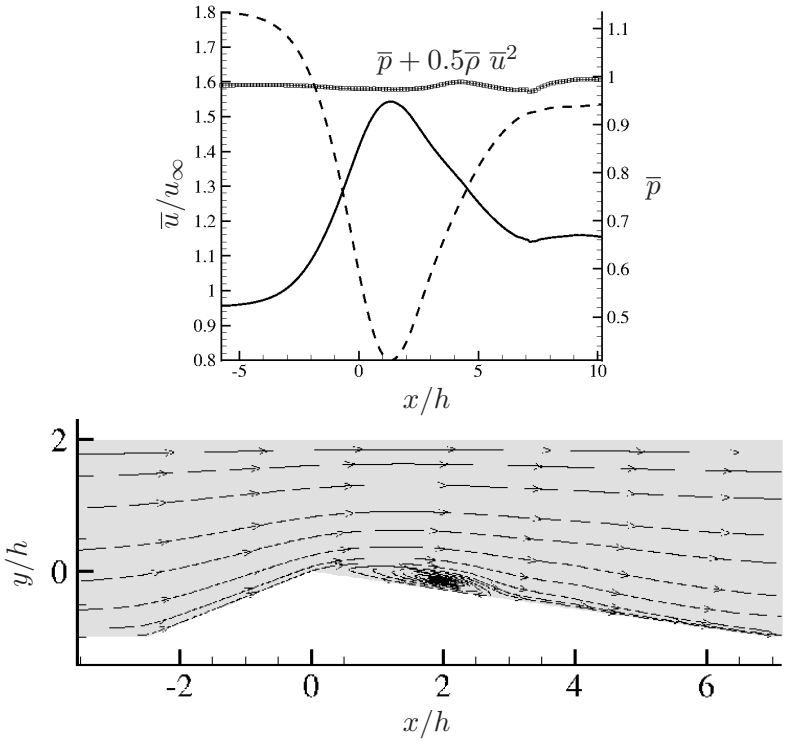

Figure 5.10: (a)Variation of mean velocity and pressure along streamwise direction, —— : u-velocity and - - - - : pressure, (b) Mean streamlines.

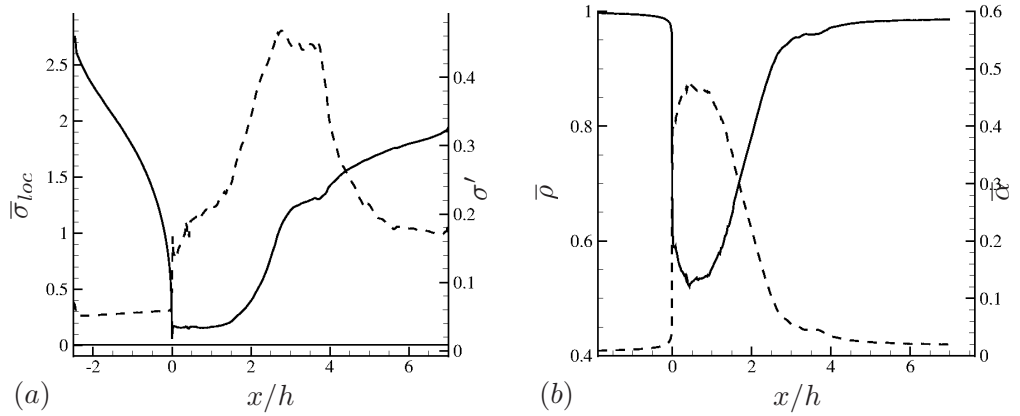

Figure 5.11: (a) Variation of $\overline{\sigma}_{loc}$ (——) and σ' (----) along the wedge wall, (b) Variation of mean density (——) and mean void fraction (----) along the wedge wall.

formation.

We define, $\overline{\sigma}_{loc} = 2(\overline{p} - p_v)/\rho_\infty u_\infty^2$ and $\sigma^{'} = 2\sqrt{\overline{p'^2}}/\rho_\infty u_\infty^2$ to further quantify the mean and rms characteristics of the vapor. Figure 5.11 (a) shows the variation of $\overline{\sigma}_{loc}$ and $\sigma^{'}$ along the wedge. $x/h = 0$ is the apex region and minimum $\overline{\sigma}_{loc}$ is obtained there. It is interesting to see that the mean pressure never falls below the vapor pressure, but the fluctuations at the apex are large enough for the instantaneous local pressure to fall below vapor pressure. Note that the value of rms is maximum $x/h = 2.5$ which corresponds to the mean closure location of the cavity. This behavior points to cavity oscillation about that position. Figure 5.11 (b) shows the variation of mean density and mean volume fraction along the wedge. It is clear that inception occurs at the apex and the maximum amount of vapor in the mean flow occurs inside the sheet cavity. The region corresponding to the cloud has lesser void fraction than that in the sheet. This observation is also in line with the observations of Coutier-Delgosha et al. [54]

The boundary layer evolution is illustrated using tangential velocity profiles at several streamwise locations as shown in Figure 5.12(a). Figure 5.12(b) shows the mean boundary layer profiles in the converging portion. Here, $\overline{u_t}$ is the mean velocity tangential to the wall and d is the distance normal to the wall. The acceleration of free stream and thinning of the boundary layer is evident. The velocity at the station $x/h = -0.5$ reduces as we move away from the bottom wall. Since this station has the least cross

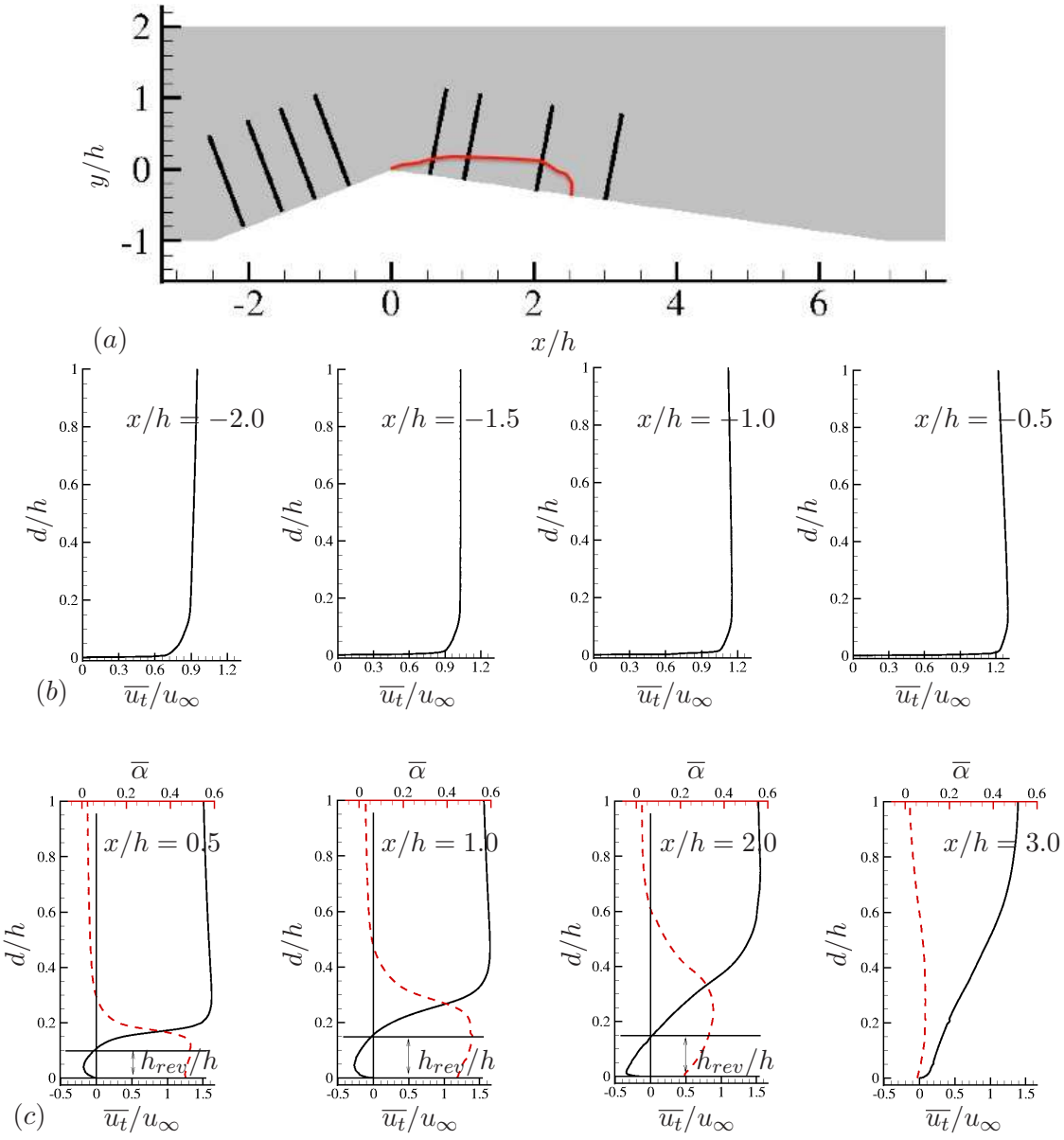

Figure 5.12: Mean boundary layer profiles at different streamwise locations.

sectional area among the all the stations shown, the effect of top wall is predominant which can be seen in the form deceleration of the bulk flow away from the wall. Figure 5.12(c) shows the mean boundary layer profiles in the diverging portion. The first three stations are inside the mean cavity and the last station is just outside the mean cavity. Negative tangential velocity is seen inside the cavity at the first three stations. Also shown are mean void fraction profiles to illustrate the relative thickness of the reverse flow inside the cavity with respect to the cavity thickness. A re–entering jet may be defined as a region of relatively high density fluid moving towards the leading edge of the cavity. The thickness of this re–entering jet h_{rev}/h is also shown in Figure 5.12(c) and is computed to be 0.1 at the station $x/h = 0.5$ and 0.15 at the stations $x/h = 1.0$ and 2.0. The adverse pressure gradient causes the magnitude of the reverse flow to be maximum at $x/h = 2.0$ which further reduces in magnitude as it moves towards the leading edge of the cavity. The magnitude of this negative velocity plays an important role in determining the location where the sheet cavity pinches off to a cloud.

The magnitude of void fraction inside the cavity as observed in Figure 5.12(c) has a maximum value of about 0.5. A more detailed understanding of the evolution of void fraction is obtained by computing its probability density function. Figure 5.13 shows the PDF of void fraction at several locations inside and outside the cavity. Figure 5.13(a) illustrates the location of points chosen for computing the PDFs. The mean cavity profile is illustrated using the red curve. The PDF close to leading edge of the cavity (at $x/h = 0.001$) shows a high probability for $\alpha = 0.1$. Since this is the cavity inception region, the value of void fraction here is not expected to be high. It is interesting to note that the time averaged value of void fraction at this location is 0.01. Thus the most probable value of void fraction at that location is very different from the mean value, illustrating the highly unsteady nature of the flow. As we move downstream along the cavity, the PDF at $x/h = 1.0$ shows a wider distribution with finite probability of occurrence for a large range of void fraction. Larger values of void fraction are more probable during the sheet cavity growth phase and smaller values during the cloud shedding phase. The mean void fraction value at this location is 0.46, which is also close to the most probable value. The location $x/h = 2.5$ corresponds to

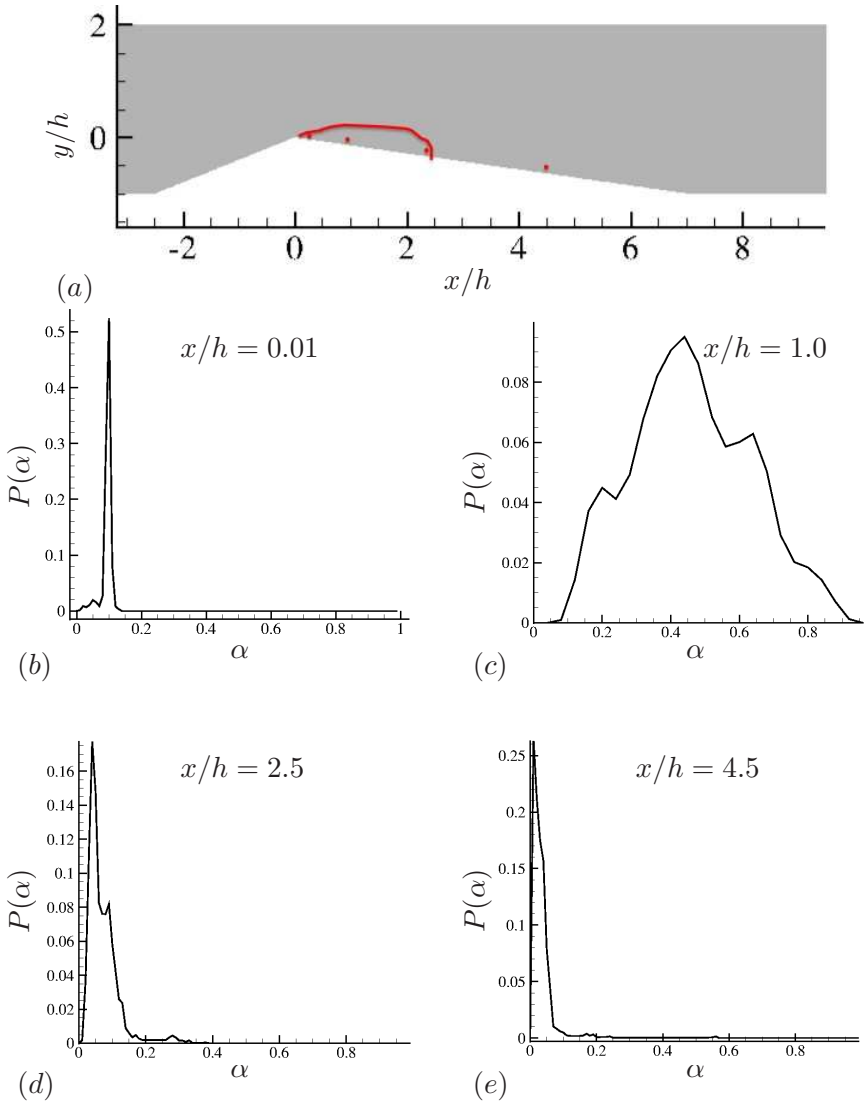

Figure 5.13: PDF of void fraction at various points inside and outside mean cavity.

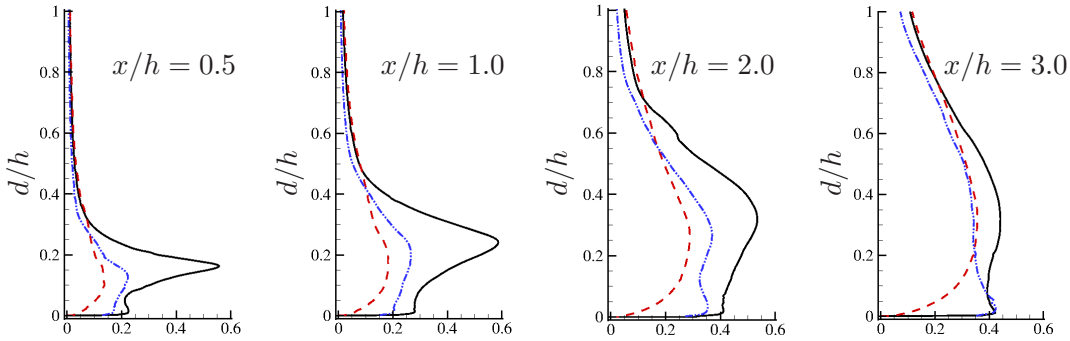

Figure 5.14: RMS of velocity profiles at different streamwise location, —— : $\sqrt{u_t'u_t'}/u_\infty$, - - - - : $\sqrt{u_n'u_n'}/u_\infty$, —·· — : $\sqrt{w'w'}/u_\infty$

the mean cavity closure and this location is highly affected by the cavity unsteadiness. The two most probable values of void fraction here are 0.05 and 0.1. Note that these values differ significantly from the time averaged value of 0.01 there and the occurrence of 0.1 corresponds to the passage of a cloud. Finally the location at $x/h = 4.5$ in the wake of the cavity shows that the most probable value of void fraction there is close to the free-stream void fraction $\alpha_0 = 0.01$. However, the passage of clouds at periodic intervals means that there is also a finite probability of void fraction around 0.1. The void fraction content in a cloud is low as observed by Coutier-Delgosha et al. [54] and it drops further as the cloud convects to a high pressure region.

Figure 5.14 shows the turbulent velocity profiles at the stations discussed in Figure 5.12. Note that we show only the resolved fluctuations. Within the cavity at $x/h = 0.5$ and 1.0, the fluctuations along the tangential direction dominate the other two components. However, near the cavity closure and downstream of the cavity, all three components of fluctuations are equally significant. This indicates that the flow near the cavity closure and in the cavity wake are highly three–dimensional compared to that inside the cavity.

5.3.3 Time evolution of cavity growth and collapse

The time evolution of sheet to cloud transition is shown as a series of snapshots in Figure 5.15. On the left are instantaneous span–averaged contours of void fraction and

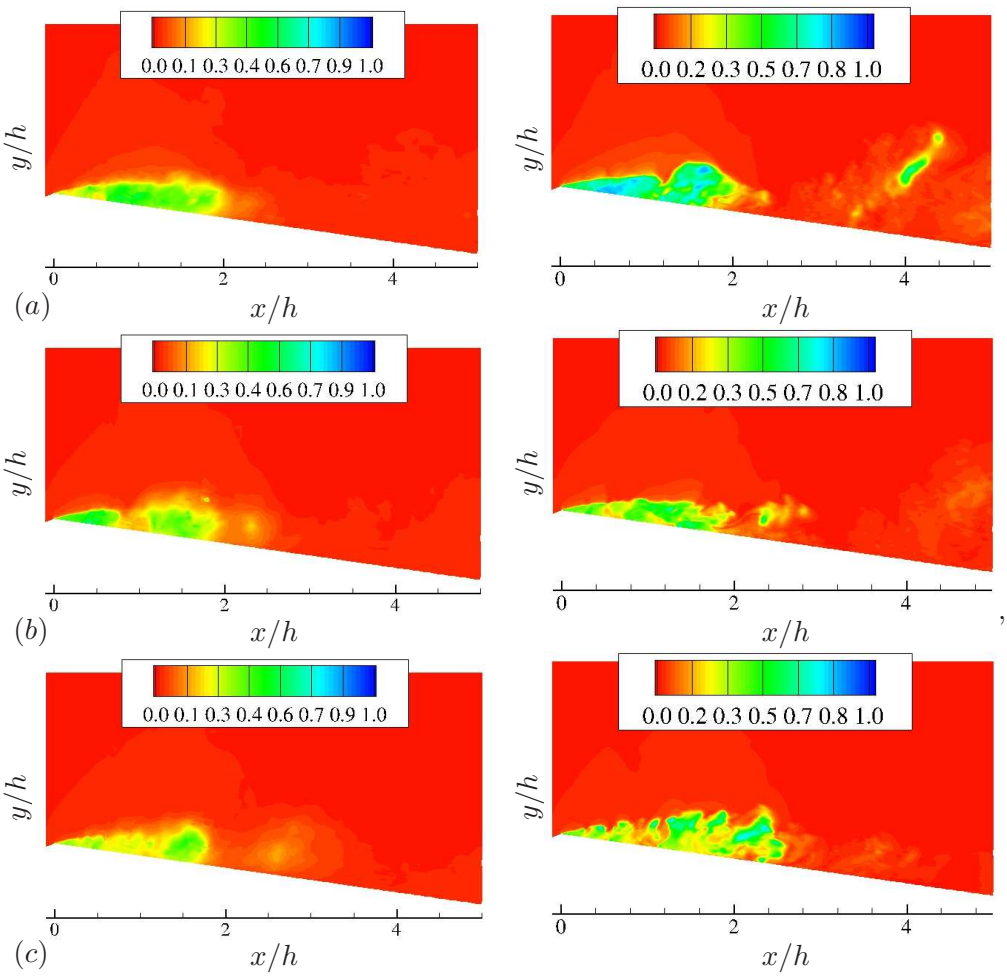

Figure 5.15: See next page for caption.

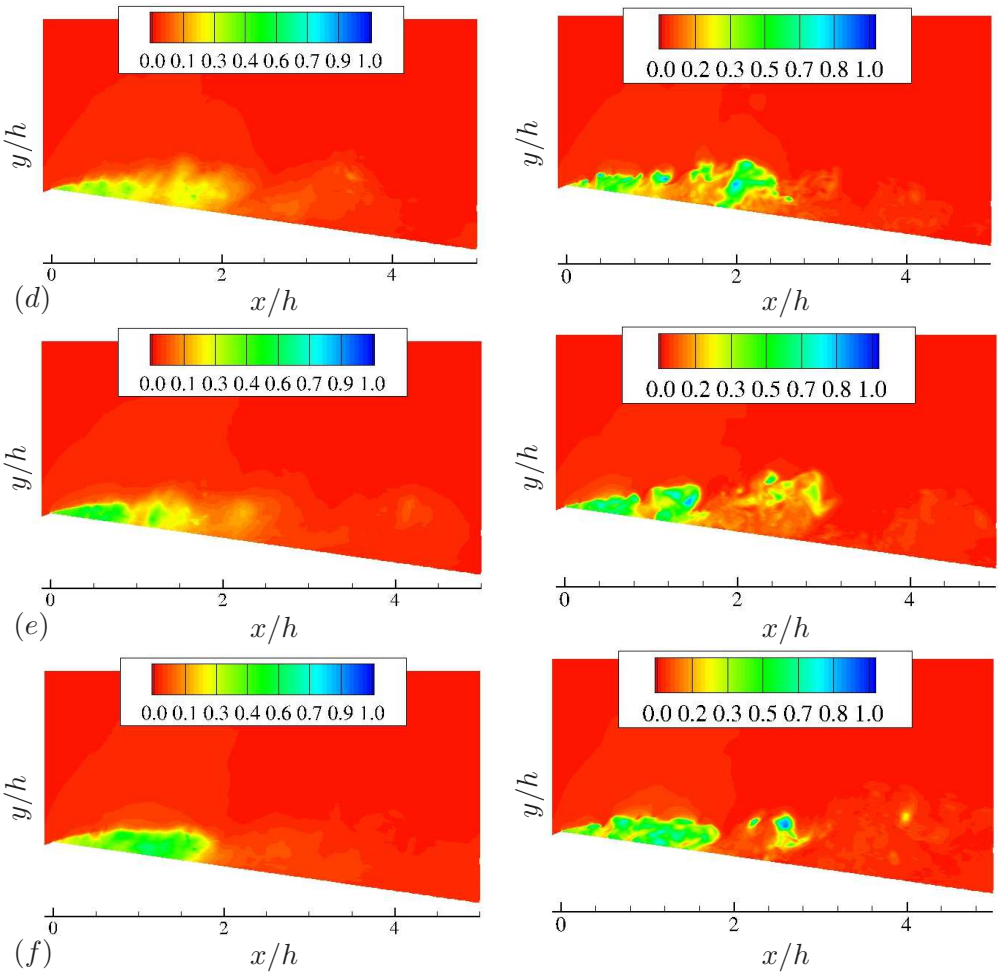

Figure 5.15: Time evolution of sheet to cloud transition. (Left) Instantaneous span–averaged void fraction contours, (Right) Instantaneous void fraction contours in the symmetry plane.

on the right are the instantaneous void fraction contours from the symmetry plane. The entire cycle can be roughly divided into different events and each figure in Figure 5.15 is representative of a particular event. The events are : (a) growth of sheet cavity to its full length, (b) primary cloud pinch off, (c) primary cloud shedding and cavity regrowth, (d) and (e) secondary cloud shedding and (f) sheet cavity regrowth. The cavity first grows to an average length of $x/D = 2.0$. The instantaneous symmetry plane contours show the impending pinch off at the trailing edge of sheet cavity. The cavity then pinches off and the primary cloud sheds as shown in the span–averaged contours. The symmetry plane contours do not show a clear pinch off indicating that the cloud is still attached to the sheet in the symmetry plane. The stark contrast between the span–averaged and instantaneous contours indicates the three-dimensionality of the cavity. The cavity then regrows to about 50% of the full cavity length and a secondary cloud pinching occurs. This phenomenon is highly three-dimensional and the instantaneous contours show the presence of multiple small cavities. These multiple smaller cavities get represented as two secondary clouds in the span–averaged contours. This three–dimensional feature is often not captured in $2D$ RANS simulation. The sheet cavity then grows to its maximum length and the entire cycle repeats again. Figure 5.16 shows the isocontours of void fraction showing the three–dimensional view of the sheet to cloud transition process. The fully grown sheet cavity is evident in (a) and a clear detached cloud is seen in (b). The secondary shedding and the three-dimensional nature of the secondary cloud is evident in (c) and finally (d) shows the sheet cavity close to it full length before the next cycle begins. The side plane in Figure 5.16 shows pressure contours. Low pressure signatures seen downstream in (a) correspond to the cloud that had shed and collapsed from the previous cycle. Similar low pressure signatures can also be observed in (c) and (d).

The frequency of the shedding phenomenon (both primary and secondary) can be estimated from the point spectra computed from the time history of pressure at several locations inside the cavity and in the wake of the cavity. Figure 5.17 shows the time history of pressure and its corresponding spectrum in the frequency domain at three different locations $x/h = 0.1, 2.5$ and 4.5 and adjacent to the wedge wall. The spectra

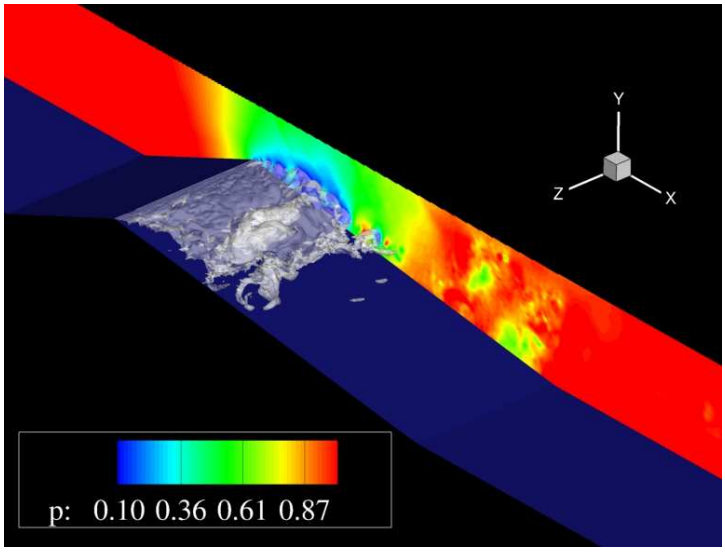

(*a*)

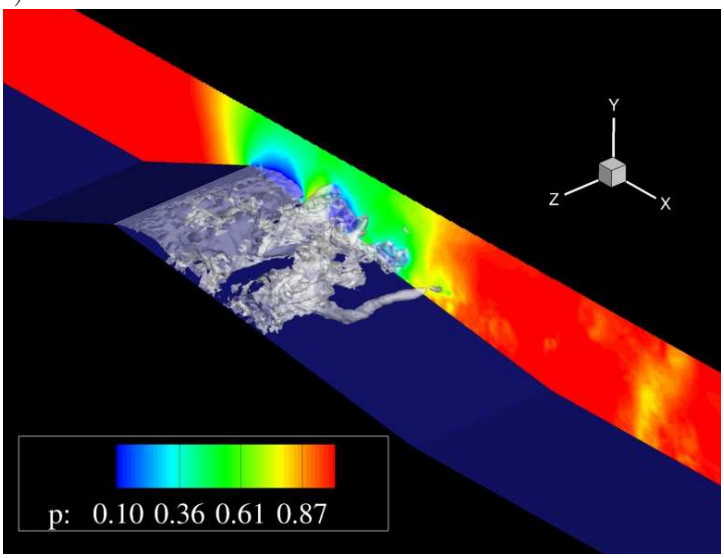

(*b*)

Figure 5.16: See next page for caption.

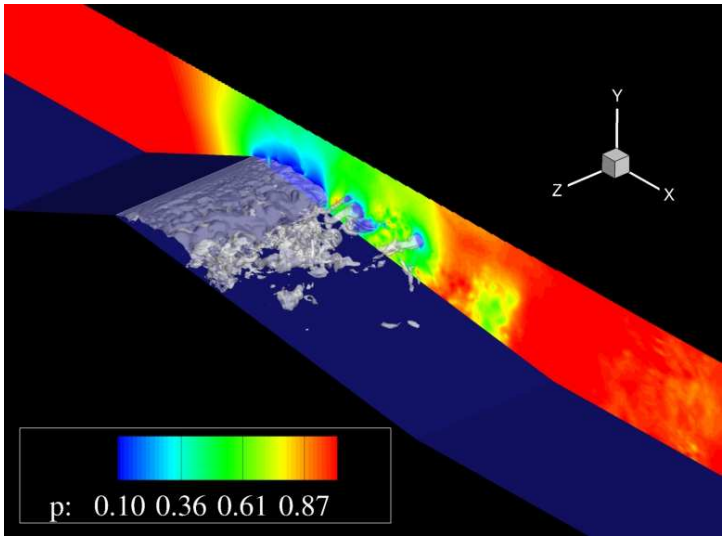

(*c*)

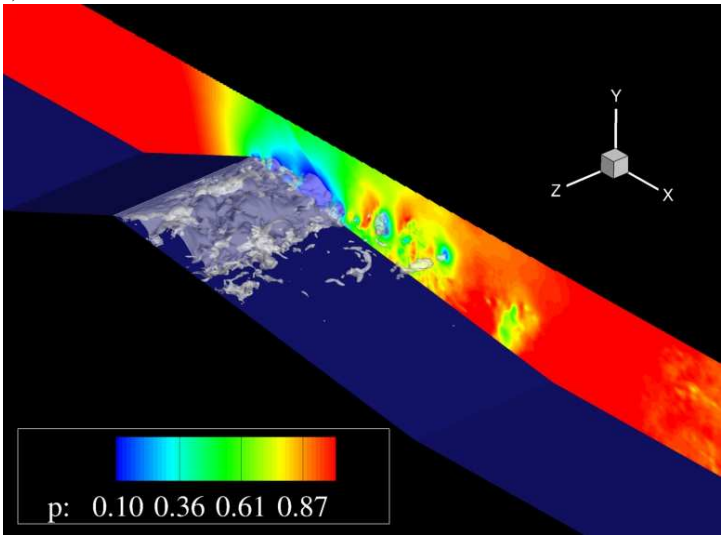

(*d*)

Figure 5.16: Three dimensional isocontours of void fraction showing time evolution of sheet to cloud transition. Side plane shows contours of pressure.

at $x/h = 2.5$ and 4.5 show a peak at $St = 0.14$, where $St = fh/u_\infty$. The shedding Strouhal number however is always expressed using maximum cavity length and hence $St_{shedding} = fl_{cav}/u_\infty$. Given that the cavity grows to a maximum length $l_{cav}/h = 2.0$, the shedding Strouhal number is 0.28. This value lies within the range of 0.25–0.3 predicted by the experiment [10]. The spectrum at $x/h = 0.1$ shows a maximum peak at $St = 0.3$. This peak corresponds to the secondary shedding which occurs at a higher frequency compared to the primary shedding i.e. many smaller clouds shed within a cycle at a higher frequency. The time history of pressure at $x/h = 0.1$ also clearly indicates this trend, with pressure peaks occurring at a frequency corresponding to $St = 0.3$.

5.3.4 Re–entering jet

The importance of adverse pressure gradient in the cavity closure region in the development of re–entering jet has been studied extensively by Laberteaux and Ceccio [50] and Callenaere et al. [82]. In Figure 5.18(a), the time history of non-dimensional pressure immediately downstream of the mean cavity closure ($x/h = 2.5$) is plotted. Also shown in Figure 5.18(b) is the time history of streamwise velocity at $x/h = 0.5$ and adjacent to the wall. A clear correlation is observed between the pressure peaks and negative velocity peaks. This implies that a strong re–entering jet is formed due to the adverse pressure gradient. Figure 5.18(c) shows the pressure evolution at a downstream location, through which the cloud cavity is expected to advect. The sudden drop in pressure observed in 5.18(c) is indeed due to the cloud passing through and it can be observed that these drops in pressure also correlate with peaks in re–entering jet. The main cloud shedding events are marked as x and z respectively and one of the secondary cloud shedding event is marked as y. For visualizing the re-entering jet, span averaged values are considered. Although spanwise variation in the re-entering jet is present, this method will give us details about the mean behavior. Streamlines plotted at three different time instants within a cycle are shown in Figure 5.19 and it shows the presence of a re-entering jet where a stream of liquid from the cavity closure enters into the cavity. The re-entrant jet then penetrates towards the apex of the wedge and the cavity pinches

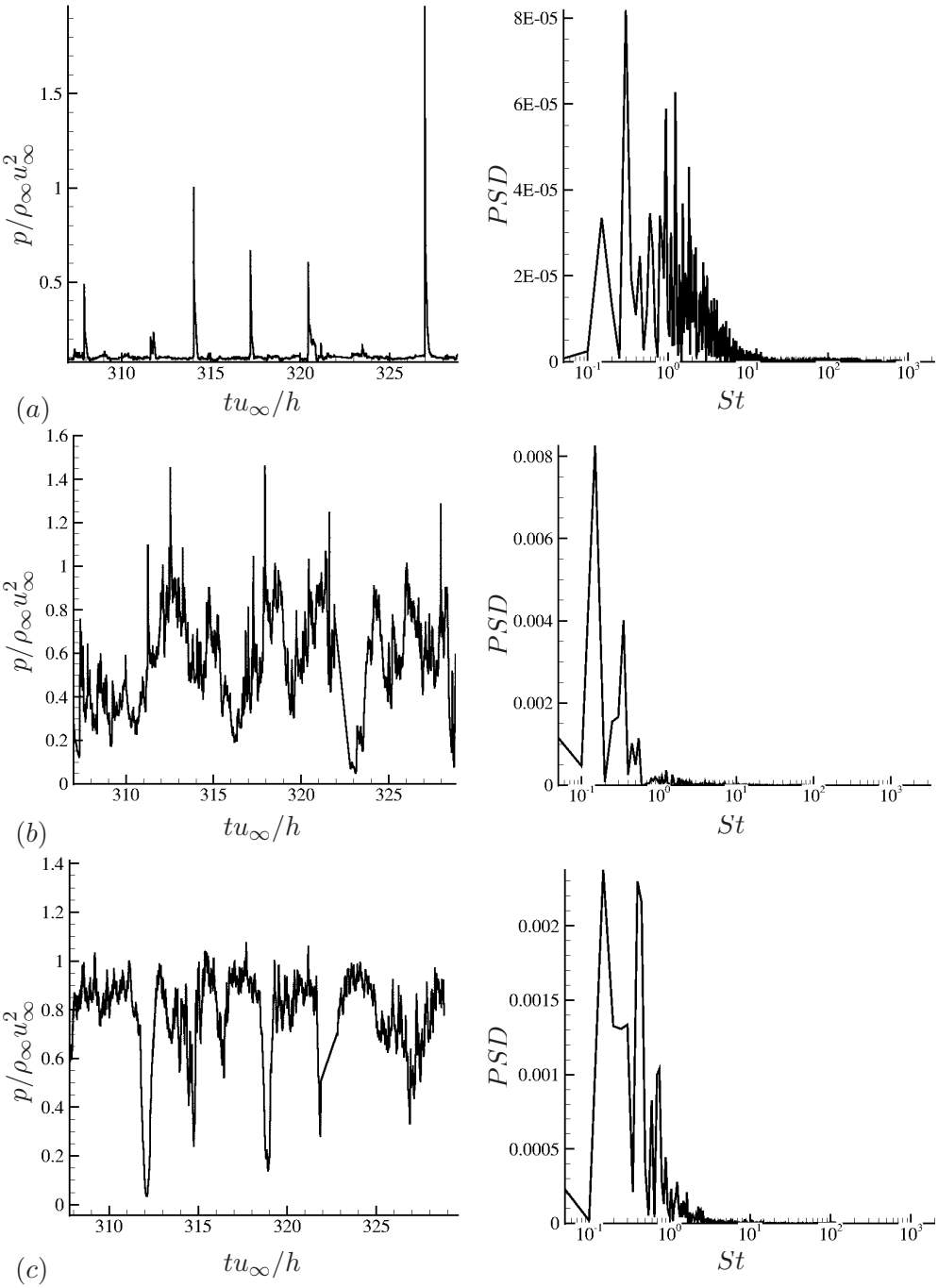

Figure 5.17: Time history of pressure (left) and their corresponding spectra (right), (a) : $x/h = 0.1$, (b) : $x/h = 2.5$ and (c) : $x/h = 4.5$.

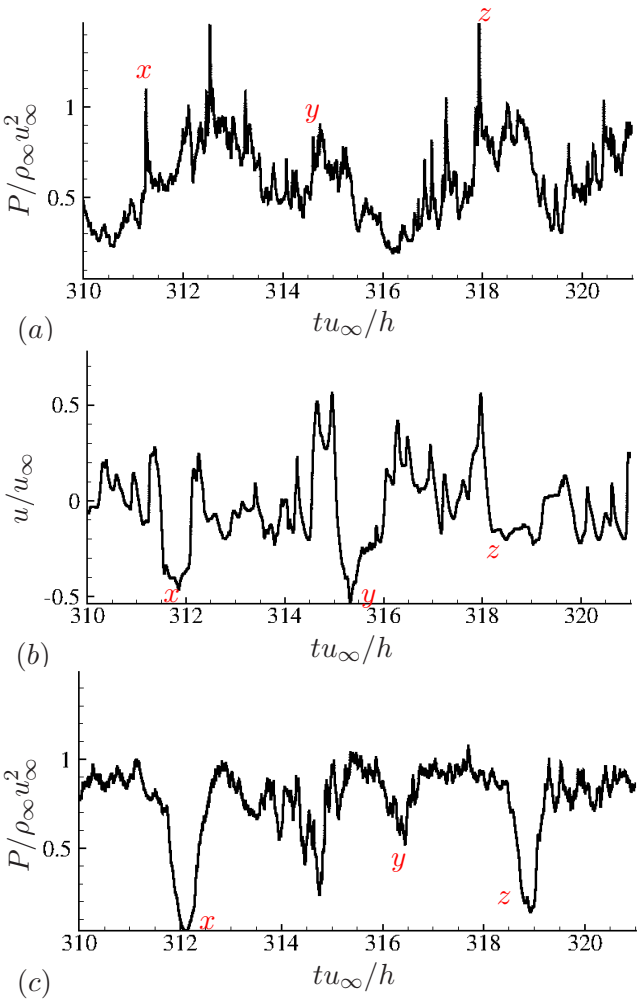

Figure 5.18: Time history of (a) pressure at $x/h = 2.5$, (b) u-velocity at $x/h = 0.5$ and (c) pressure at $x/h = 4.5$.

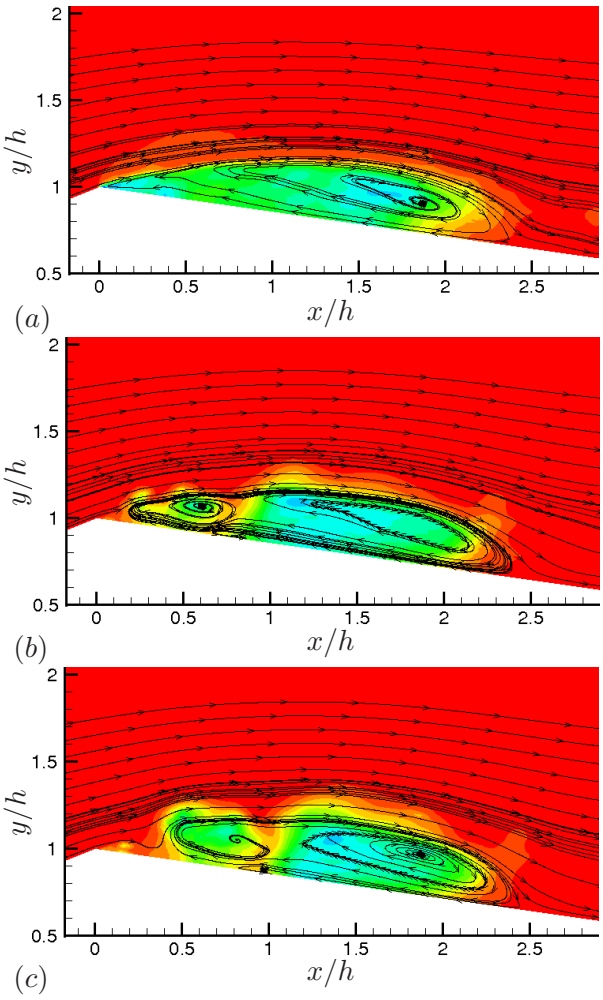

Figure 5.19: Three instants within a cycle showing the re–entering jet.

off close to the apex of the wedge.

5.3.5 Pressure waves

When a vapor cavity collapses, it creates a void and surrounding water rushes into the void creating a water hammer effect. This causes a large amount of pressure to be concentrated locally resulting in compression waves that travel in all directions. Due to the geometry confinement, these pressure waves get reflected multiple times causing a complex pressure wave pattern. These pressure waves also travel towards the inflow

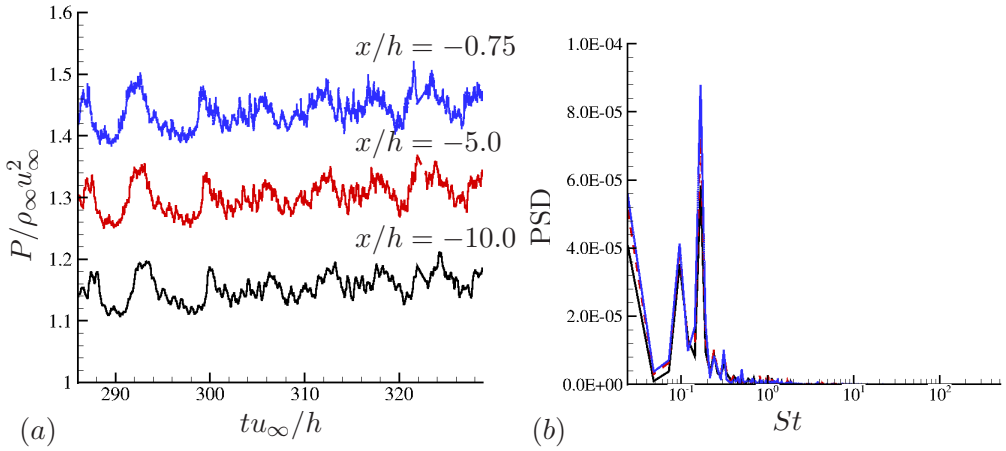

Figure 5.20: Pressure history upstream of the wedge showing the effect of pressure waves.

and modifies the oncoming flow significantly. Figure 5.20(a) shows the pressure history at three locations upstream of the wedge. The pressure increase caused due to pressure waves can be seen and it can be observed that the pressure at these locations are highly correlated. The direction of the pressure waves is towards the inlet. The spectra of pressure history at all these locations look identical as seen in Figure 5.20(b), with a dominant peak at $St = 0.16$. Although the pressure waves are caused due to cloud collapse, the complex interaction between the pressure waves among themselves and the domain boundaries mean that, the Strouhal number observed at the upstream locations is neither equal to the primary shedding Strouhal number nor the secondary shedding Strouhal number.

The pressure waves have both wave–like and intermittent behavior which can be observed from Figure 5.21 which shows lines of pressure in the side plane. The highly intermittent turbulent pressure fluctuations can be observed downstream of the cavity. The white region without pressure lines indicates the presence of the cavity. The pressure waves produced by collapse are seen to impinge on the cavity. Pressure contours on the wedge wall also shed some light on the three–dimensionality of the vapor cavity. A pressure front across the span can be observed in Figure 5.21(a) and the leading edge of the front is denoted by the arrow mark. This indicates the front separating

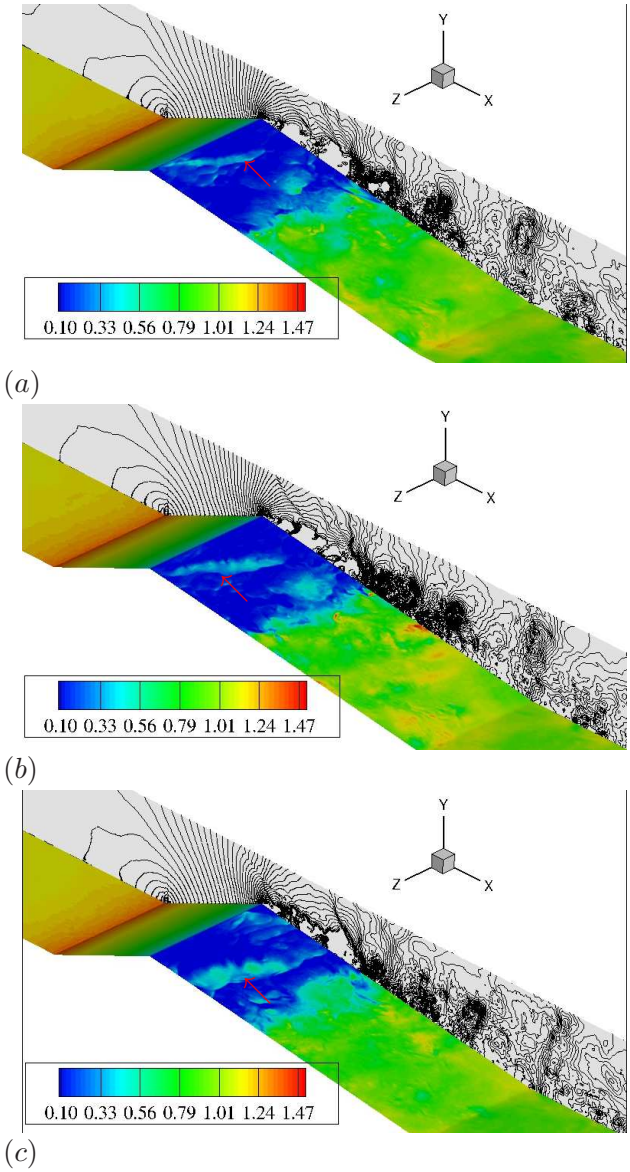

Figure 5.21: Pressure waves caused due to cavity collapse showing highly intermittent behavior. The bottom wall shows pressure contours and the side wall shows contour lines of pressure.

the cloud from the sheet. The process of cloud detachment is also observed to be three dimensional with variations across the span.

To summarize, the quantitative agreement of LES with experiment for this highly complex flow is encouraging and the three–dimensional unsteady data yielded by the LES offers unique physical insight into the sheet to cloud transition phenomenon.

Chapter 6

Summary

This dissertation develops a numerical method for LES/DNS of cavitating flows and applies it to study two different types of cavitation : vortex cavitation over a circular cylinder and sheet to cloud cavitation over a wedge. The numerical method is implemented in an existing compressible solver MPCUGLES, developed in FORTRAN 90 and parallelized using MPI. A homogeneous mixture model is used to model the multiphase mixture as a single compressible fluid. A characteristic-based filter is developed to handle shocks and material discontinuities. A novel predictor corrector method is developed where the predictor step is non-dissipative and the corrector step is independent of the base scheme in the predictor step. A sensor based on vorticity, divergence and volume fraction is used in the corrector step to prevent excessive dissipation from the discontinuities. The method is first validated for canonical one dimensional problems and then extended to solve two and three dimensional problems.

The proposed numerical method is used to study cavitation on a circular cylinder at two Reynolds numbers and several cavitation numbers. The simulated cavitation numbers correspond to two different regimes based on how the cavity is shed into the wake. The dynamics of the cavity formation and collapse, leading to pressure waves are captured in the simulations and discussed in detail. A scaling for cavitation number based on maximum velocity in the shear layer is found to collapse the cavity length as a function of cavitation numbers at different Reynolds number onto a single curve. In

the cyclic regime ($\sigma = 1.0$) of cavitation, cavity detaches from the body itself at the shedding frequency, while in the transitory regime of cavitation ($\sigma = 0.7$ and 0.5), a low frequency cavity detachment phenomenon is observed in addition to the shedding frequency. Cavitation is found to significantly modify the vortex shedding frequency and vorticity dilatation due to vapor is found to be responsible for this shedding frequency reduction. This effect is further verified by computing circulation in the wake, which shows that vorticity reduces as the cavitation number is lowered. The effect of initial void fraction is assessed. It is found that changing the initial void fraction does not affect the general dynamics of cavity formation. However, the speed of sound is altered significantly and this leads to pressure waves traveling at different speeds. The compressibility and acoustic impedance of the medium are altered but the condensation ratio in the medium shows a similarity for different free stream void fraction values. The pressure fluctuation contours show spatially local phenomenon due to the interaction between condensation waves and vortices at specific locations in space. LES of cavitating flow at $Re = 3900$ reveals that for a given cavitation number, the length of the mean cavity obtained at higher Reynolds number is higher than that obtained at a low Reynolds number. The vortex shedding frequency is again lower compared to a single phase shedding frequency and vorticity dilatation is found to be an important factor in reducing vorticity in the wake in this case too. Cavitation effectively reduces Reynolds number in the near wake, suppresses turbulence and delays the three dimensional breakdown of Karman vortices.

The method is then used to perform LES of sheet to cloud cavitation over a wedge geometry. The mean void fraction inside the cavity agrees well with the experiments and the mean length and thickness of the cavity are also predicted reasonably. The Strouhal number corresponding to cloud shedding shows good agreement with the experiment. The velocity fluctuations indicate that only streamwise fluctuations are dominant inside the cavity, while both streamwise and spanwise fluctuations are equally dominant at the cavity closure and in the cavity wake. The probability density function of void fraction plotted at several locations inside the cavity shows that the mean value obtained from time averaged data is very different from the most probable value of void fraction

indicating the unsteadiness of the flow. The time evolution of void fraction shows that multiple smaller cavities are also shed apart from a main cloud. This highly unsteady phenomenon is often not captured in time averaged simulations. The point spectra at various points inside the cavity clearly shows the primary and secondary shedding frequency. The time history at these points also show a clear correlation between adverse pressure gradient, re–entering jet and the cloud formation. The cloud collapse results in pressure waves which have both wave–like and highly intermittent behavior. These pressure waves impinge on the growing cavity and affect the shedding characteristics significantly.

Bibliography

[1] URL http://www.1.k.u-tokyo.ac.jp/yama/fluidlab/Research/CavPictures/index_e.html.

[2] R. E. Henry, M. A. Grolmes, and H. K. Fauske. Pressure–pulse propagation in two–phase one and two–component mixtures. Technical report, Argonne National Lab., Ill., 1971.

[3] N. I. Semenov and S. I. Kosterin. Results of studying the speed of sound in moving gas–liquid systems. *Teploenergetika*, 11(6):46–51, 1964.

[4] H. B. Karplus. Velocity of sound in a liquid containing gas bubbles. *The Journal of the Acoustical Society of America*, 29:12–61, 1957.

[5] R. Saurel and O. Lemetayer. A multiphase model for compressible flows with interfaces, shocks, detonation waves and cavitation. *Journal of Fluid Mechanics*, 431(6):239–271, 2001.

[6] Y. Shen and P. E. Dimotakis. The influence of surface cavitation on hydrodynamic forces. In *Proceedings of 22nd American Towing Tank Conference*, pages 44–53, 1989.

[7] H. Rouse and J. S. McNown. Cavitation and pressure distribution: head forms at zero angle of yaw. 1948.

[8] B. C. Syamala Rao and D. V. Chandrasekhara. Some characteristics of cavity

flow past cylindrical inducers in a venturi. *Journal of Fluids Engineering*, 98(3): 461–466, 1976.

[9] A. Verma and K. Mahesh. A Lagrangian subgrid–scale model with dynamic estimation of Lagrangian time scale for large eddy simulation of complex flows. *Physics of Fluids*, 24(8):085–101, 2012.

[10] H. Ganesh. *Bubbly shock propagation as a cause of sheet to cloud transition of partial cavitation and stationary cavitation bubbles forming on a delta wing vortex.* PhD thesis, University of Michigan, 2015.

[11] R. T. Knapp, J. W. Daily, and F. G. Hammit. *Cavitation.* McGraw-Hill Book Company, London, 1970.

[12] J-P. Franc and J-M. Michel. *Fundamentals of cavitation*, volume 76. Springer Science & Business Media, 2006.

[13] R. E. A. Arndt. Cavitation in fluid machinery and hydraulic structures. *Annual Review of Fluid Mechanics*, 13(1):273–326, 1981.

[14] R. E. A. Arndt. Cavitation in vortical flows. *Annual Review of Fluid Mechanics*, 34(1):143–175, 2002.

[15] B. R. Shin, Y. Iwata, and T. Ikohagi. Numerical simulation of unsteady cavitating flows using a homogenous equilibrium model. *Computational Mechanics*, 30(5-6): 388–395, 2003.

[16] R. F. Kunz, D. A. Boger, D. R. Stinebring, T. S. Chyczewski, J. W. Lindau, H. J. Gibeling, S. Venkateswaran, and T. R. Govindan. A preconditioned Navier–Stokes method for two–phase flows with application to cavitation prediction. *Computers & Fluids*, 29(8):849–875, 2000.

[17] V. Ahuja, A. Hosangadi, and S. Arunajatesan. Simulations of cavitating flows using hybrid unstructured meshes. *Journal of Fluids Engineering*, 123(2):331–340, 2001.

[18] G. H. Schnerr, I. H. Sezal, and S. J. Schmidt. Numerical investigation of three–dimensional cloud cavitation with special emphasis on collapse induced shock dynamics. *Physics of Fluids*, 20(4):1–9, 2008.

[19] T. G. Liu, B. C. Khoo, and W. F. Xie. Isentropic one–fluid modeling of unsteady cavitating flow. *Journal of Computational Physics*, 201(1):80–108, 2004.

[20] Y. Saito, R. Takami, I. Nakamori, and T. Ikohagi. Numerical analysis of unsteady behavior of cloud cavitation around a NACA0015 foil. *Computational Mechanics*, 40(1):85–96, 2007.

[21] J. H. Seo and S. Lele. Numerical investigation of cloud cavitation and cavitation noise on a hydrofoil section. In *7th International Symposium on Cavitation*, number 0062, pages 1–15, 2009.

[22] J. H. Seo, Y. J. Moon, and B. R. Shin. Prediction of cavitating flow noise by direct numerical simulation. *Journal of Computational Physics*, 227(13):6511–6531, 2008.

[23] A. K. Singhal, M. M. Athavale, H. Li, and Y. Jiang. Mathematical basis and validation of the full cavitation model. *Journal of Fluids Engineering*, 124(3):617–624, 2002.

[24] I. Senocak and W. Shyy. A pressure–based method for turbulent cavitating flow computations. *Journal of Computational Physics*, 176(2):363–383, 2002.

[25] S. Frikha, O. Coutier-Delgosha, and J-A. Astolfi. Influence of the cavitation model on the simulation of cloud cavitation on 2D foil section. *International Journal of Rotating Machinery*, 2008:1–12, 2009.

[26] R. E. A. Arndt, C. C. S. Song, M. Kjeldsen, J. He, and A. Keller. Instability of partial cavitation: a numerical/experimental approach. In *Proceedings of the 23rd Symposium on Naval Hydrodynamics*, pages 519–615. National Academies Press, 2000.

[27] R. E. Bensow and G. Bark. Implicit LES predictions of the cavitating flow on a propeller. *Journal of Fluids Engineering*, 132(4):1–10, 2010.

[28] N. Dittakavi, A. Chunekar, and S. Frankel. Large eddy simulation of turbulent–cavitation interactions in a venturi nozzle. *Journal of Fluids Engineering*, 132(12): 1–12, 2010.

[29] M. P. Kinzel, J. W. Lindau, L. J. Peltier, R. F. Kunz, and V. Sankaran. Detached–eddy simulations for cavitating flows. In *Proceedings of the 18th AIAA Computational Fluid Dynamics Conference, AIAA Paper*, number 4098, pages 1–10, 2007.

[30] B. Ji, X-W. Luo, X-X. Peng, and Y-L. Wu. Three–dimensional large eddy simulation and vorticity analysis of unsteady cavitating flow around a twisted hydrofoil. *Journal of Hydrodynamics, Ser. B*, 25(4):510–519, 2013.

[31] G. Wang and M. Ostoja-Starzewski. Large eddy simulation of a sheet/cloud cavitation on a NACA0015 hydrofoil. *Applied Mathematical Modelling*, 31(3):417–447, 2007.

[32] A. Hosangadi and V. Ahuja. Numerical study of cavitation in cryogenic fluids. *Journal of Fluids Engineering*, 127(2):267–281, 2005.

[33] X. B. Zhang, L. M. Qiu, Y. Gao, and X. J. Zhang. Computational fluid dynamic study on cavitation in liquid nitrogen. *Cryogenics*, 48(9):432–438, 2008.

[34] E. Goncalvès and R. F. Patella. Numerical study of cavitating flows with thermodynamic effect. *Computers & Fluids*, 39(1):99–113, 2010.

[35] K. Mahesh, G. Constantinescu, and P. Moin. A numerical method for large eddy simulation in complex geometries. *Journal of Computational Physics*, 197(1):215–240, 2004.

[36] Y. Hou and K. Mahesh. A robust, colocated, implicit algorithm for direct numerical simulation of compressible, turbulent flows. *Journal of Computational Physics*, 205 (1):205–221, 2005.

[37] H. C. Yee, N. D. Sandham, and M. J. Djomehri. Low–dissipative high–order shock–capturing methods using characteristic–based filters. *Journal of Computational Physics*, 150(1):199–238, 1999.

[38] N. Park and K. Mahesh. Numerical and modeling issues in LES of compressible turbulence on unstructured grids. In *Proceedings of the 45th AIAA Aerospace Sciences Meeting and Exhibit, AIAA Paper*, number 0722, pages 1–18, 2007.

[39] S-C. Lo, G. A. Blaisdell, and A. S. Lyrintzis. High–order shock capturing schemes for turbulence calculations. *International Journal for Numerical Methods in Fluids*, 62(5):473–498, 2010.

[40] B. Gustafsson and P. Olsson. Fourth–order difference methods for hyperbolic IB-VPs. *Journal of Computational Physics*, 117(2):300–317, 1995.

[41] A. Harten. High resolution schemes for hyperbolic conservation laws. *Journal of Computational Physics*, 49(3):357–393, 1983.

[42] F. Ducros, V. Ferrand, F. Nicoud, C. Weber, D. Darracq, C. Gacherieu, and T. Poinsot. Large–eddy simulation of the shock/turbulence interaction. *Journal of Computational Physics*, 152(2):517–549, 1999.

[43] A. Gnanaskandan and K. Mahesh. A numerical method to simulate turbulent cavitating flows. *International Journal of Multiphase Flow*, 70:22–34, 2015.

[44] A. Gnanaskandan and K. Mahesh. Large eddy simulation of sheet to cloud cavitation. In *Proceedings of the 30th Symposium on Naval Hydrodynamics*, pages 1–13, 2014.

[45] R. S. Lagumbay, O. V. Vasilyev, and A. Haselbacher. Homogeneous equilibrium mixture model for simulation of multiphase/multicomponent flows. *International Journal for Numerical Methods in Fluids*, 4(00821):1–6, 2007.

[46] R. Abgrall and S. Karni. Computations of compressible multifluids. *Journal of Computational Physics*, 169(2):594–623, 2001.

[47] S. Karni. Multicomponent flow calculations by a consistent primitive algorithm. *Journal of Computational Physics*, 112(1):31–43, 1994.

[48] T. Barberon and P. Helluy. Finite volume simulation of cavitating flows. *Computers & fluids*, 34(7):832–858, 2005.

[49] J-B. Leroux, J. A. Astolfi, and J. Y. Billard. An experimental study of unsteady partial cavitation. *Journal of Fluids Engineering*, 126(1):94–101, 2004.

[50] K. R. Laberteaux and S. L. Ceccio. Partial cavity flows. Part 1. Cavities forming on models without spanwise variation. *Journal of Fluid Mechanics*, 431:1–41, 2001.

[51] P. R. Spalart and S. R. Allmaras. A one equation turbulence model for aerodynamic flows. *AIAA Journal*, 94(439):1–22, 1992.

[52] J-P. Franc and J-M. Michel. Unsteady attached cavitation on an oscillating hydrofoil. *Journal of Fluid Mechanics*, 193:171–189, 1988.

[53] A. Kubota, H. Kato, and H. Yamaguchi. A new modelling of cavitating flows: A numerical study of unsteady cavitation on a hydrofoil section. *Journal of Fluid Mechanics*, 240(1):59–96, 1992.

[54] O. Coutier-Delgosha, B. Stutz, A. Vabre, and S. Legoupil. Analysis of cavitating flow structure by experimental and numerical investigations. *Journal of Fluid Mechanics*, 578:171–222, 2007.

[55] S. Fry. Investigating cavity/wake dynamics for a circular cylinder by measuring noise spectra. *Journal of Fluid Mechanics*, 142:187–200, 1984.

[56] Y. Matsudaira, Y. Gomi, and R. Oba. Characteristics of bubble–collapse pressures in a Karman-vortex cavity. *JSME International Journal*, 35(2):179–185, 1992.

[57] A. Roshko. Experiments on the flow past a circular cylinder at very high Reynolds number. *Journal of Fluid Mechanics*, 10(03):345–356, 1961.

[58] P. W. Bearman. On vortex shedding from a circular cylinder in the critical Reynolds number regime. *Journal of Fluid Mechanics*, 37(03):577–585, 1969.

[59] C. H. K. Williamson. Defining a universal and continuous Strouhal–Reynolds number relationship for the laminar vortex shedding of a circular cylinder. *Physics of Fluids*, 31(10):2742–2744, 1988.

[60] C. H. K. Williamson. Oblique and parallel modes of vortex shedding in the wake of a circular cylinder at low Reynolds numbers. *Journal of Fluid Mechanics*, 206: 579–627, 1989.

[61] M. Hammache and M. Gharib. An experimental study of the parallel and oblique vortex shedding from circular cylinders. *Journal of Fluid Mechanics*, 232:567–590, 1991.

[62] J. J. Varga and G. Y. Sebestyen. Determination of hydrodynamic cavitation intensity by noise measurement. In *Proceedings of the 2nd International JSME Symposium on Fluid Machinery and Fluidics*, pages 285–292, 1972.

[63] P. A. Brandner, G. J. Walker, P. N. Niekamp, and B. Anderson. An experimental investigation of cloud cavitation about a sphere. *Journal of Fluid Mechanics*, 656: 147–176, 2010.

[64] B. C. Syamala Rao, D. V. Chandrasekhara, and K. Seetharamiah. A high–speed photographic study of vortex shedding behind circular cylinders of cavitating flows. In *Proceedings of 2nd International JSME Symposium Fluid Machinery and Fluidics*, pages 293–302, 1972.

[65] S. M. Selim. *Cavitation erosion in fluid flow.* PhD thesis, University of Southampton, 1981.

[66] R. Balachandar and A. S. Ramamurthy. Pressure distribution in cavitating circular cylinder wakes. *Journal of Engineering Mechanics*, 125(3):356–358, 1999.

[67] Y. Saito and K. Sato. Cavitation bubble collapse and impact in the wake of a circular cylinder. In *Proceedings of the 5th International Symposium on Cavitation*, number 4, pages 1–6, 2003.

[68] J. O. Young and J. W. Holl. Effects of cavitation on periodic wakes behind symmetric wedges. *Journal of Fluids Engineering*, 88(1):163–176, 1966.

[69] B. Belahadji, J-P. Franc, and J-M. Michel. Cavitation in the rotational structures of a turbulent wake. *Journal of Fluid Mechanics*, 287:383–403, 1995.

[70] A. Gnanaskandan and K. Mahesh. Towards numerical simulation of cavitating flows in complex geometries. In *Proceedings of the 8th International Symposium On Cavitation*, number 153, pages 1–6, 2012.

[71] J. H. Gerrard. The mechanics of the formation region of vortices behind bluff bodies. *Journal of Fluid Mechanics*, 25(02):401–413, 1966.

[72] P. J. Strykowski and K. R. Sreenivasan. On the formation and suppression of vortex shedding at low Reynolds numbers. *Journal of Fluid Mechanics*, 218:71–107, 1990.

[73] A. Dipankar, T. K. Sengupta, and S. B. Talla. Suppression of vortex shedding behind a circular cylinder by another control cylinder at low Reynolds numbers. *Journal of Fluid Mechanics*, 573:171–190, 2007.

[74] S. Mittal and A. Raghuvanshi. Control of vortex shedding behind circular cylinder for flows at low Reynolds numbers. *International Journal for Numerical Methods in Fluids*, 35(4):421–447, 2001.

[75] J. Katz. Cavitation phenomena within regions of flow separation. *Journal of Fluid Mechanics*, 140:397–436, 3 1984. ISSN 1469-7645.

[76] R. E. A. Arndt and B. H. Maines. Nucleation and bubble dynamics in vortical flows. *Journal of Fluids Engineering*, 122(3):488–493, 2000.

[77] C-T. Hsiao and G. L. Chahine. Scaling of tip vortex cavitation inception noise with a bubble dynamics model accounting for nuclei size distribution. *Journal of Fluids Engineering*, 127(1):55–65, 2005.

[78] T. Colonius. Modeling artificial boundary conditions for compressible flow. *Annual Review of Fluid Mechanics*, 36:315–345, 2004.

[79] B. Stutz and J-L. Reboud. Two–phase flow structure of sheet cavitation. *Physics of Fluids*, 9(12):3678–3686, 1997.

[80] T. M. Pham, F. Larrarte, and D. H. Fruman. Investigation of unsteady sheet cavitation and cloud cavitation mechanisms. *Journal of Fluids Engineering*, 121 (2):289–296, 1999.

[81] Y. Kawanami, H. Kato, H. Yamaguchi, M. Tanimura, and Y. Tagaya. Mechanism and control of cloud cavitation. *Journal of Fluids Engineering*, 119(4):788–794, 1997.

[82] M. Callenaere, J-P. Franc, J. Michel, and M. Riondet. The cavitation instability induced by the development of a re-entrant jet. *Journal of Fluid Mechanics*, 444: 223–256, 2001.

[83] I. Senocak and W. Shyy. Interfacial dynamics–based modelling of turbulent cavitating flows, Part–1: Model development and steady–state computations. *International Journal for Numerical Methods in Fluids*, 44(9):975–995, 2004.

[84] E. Goncalves and R-F. Patella. Numerical simulation of cavitating flows with homogeneous models. *Computers & Fluids*, 38(9):1682–1696, 2009.

[85] S. Kim. A numerical study of unsteady cavitation on a hydrofoil. In *Proceedings of the 7th International Symposium on Cavitation*, number 56, pages 1–13, 2009.

[86] A. Koop and H. Hoeijmakers. Numerical simulation of unsteady three–dimensional sheet cavitation. In *Proceedings of the 7th International Symposium on Cavitation*, number 26, pages 1–12, 2009.

[87] B. Ji, X.W. Luo, Y. Wu, X. Peng, and Y. Duan. Numerical analysis of unsteady cavitating turbulent flow and shedding horse–shoe vortex structure around a twisted hydrofoil. *International Journal of Multiphase Flow*, 51:33–43, 2013.

[88] B. Ji, X. W. Luo, R. E. A. Arndt, X. Peng, and Y. Wu. Large eddy simulation and theoretical investigations of the transient cavitating vortical flow structure around a NACA66 hydrofoil. *International Journal of Multiphase Flow*, 68:121–134, 2015.

[89] B. Huang, Y. Zhao, and G. Wang. Large eddy simulation of turbulent vortex–cavitation interactions in transient sheet/cloud cavitating flows. *Computers & Fluids*, 92:113–124, 2014.

[90] R. E. A. Arndt, M. Wosnik, and Q. Qin. Experimental and numerical investigation of large scale structures in cavitating wakes. In *Proceedings of the 36th AIAA Fluid Dynamics Conference and Exhibit, AIAA Paper*, number 3046, pages 1–8, 2006.

[91] X. Yu, C. Huang, T. Du, L. Liao, X. Wu, Z. Zheng, and Y. Wang. Study of characteristics of cloud cavity around axisymmetric projectile by large eddy simulation. *Journal of Fluids Engineering*, 136(5):1–10, 2014.

[92] O. Coutier-Delgosha, R. Fortes-Patella, and J-L. Reboud. Evaluation of the turbulence model influence on the numerical simulations of unsteady cavitation. *Journal of Fluids Engineering*, 125(1):38–45, 2003.

Appendix A

Flux Jacobian and Eigen vectors

A.1 Flux Jacobian

The non-zero elements of the Jacobian matrix A_{ij} are listed below.

$A_{12} = n_x$

$A_{13} = n_y$

$A_{14} = n_z$

$A_{21} = (\gamma^* - 1)e_k^* n_x - uv_N$

$A_{22} = v_N - (\gamma^* - 2)un_x$

$A_{23} = un_y - (\gamma^* - 1)vn_x$

$A_{24} = un_z - (\gamma^* - 1)wn_x$

$A_{25} = (\gamma^* - 1)n_x$

$A_{26} = (\gamma^* - 1)e^* n_x$

$A_{31} = (\gamma^* - 1)e_k^* n_y - vv_N$

$A_{32} = vn_x - (\gamma^* - 1)un_y$

$A_{33} = v_N - (\gamma^* - 2)vn_y$

$A_{34} = vn_z - (\gamma^* - 1)wn_y$

$A_{35} = (\gamma^* - 1)n_y$

$A_{36} = (\gamma^* - 1)e^* n_y$

$A_{41} = (\gamma^* - 1)e_k^* n_z - wv_N$

$$A_{42} = wn_x - (\gamma^* - 1)un_z$$
$$A_{43} = wn_y - (\gamma^* - 1)vn_z$$
$$A_{44} = v_N - (\gamma^* - 2)wn_z$$
$$A_{45} = (\gamma^* - 1)n_z$$
$$A_{46} = (\gamma^* - 1)e^* n_z$$
$$A_{51} = ([(\gamma^* - 1)e_k^* - h_t]v_N$$
$$A_{52} = h_t n_x - (\gamma^* - 1)uv_N$$
$$A_{53} = h_t n_y - (\gamma^* - 1)vv_N$$
$$A_{54} = h_t n_z - (\gamma^* - 1)wv_N$$
$$A_{55} = \gamma^* v_N$$
$$A_{56} = (\gamma^* - 1)e^* v_N$$
$$A_{61} = -Yv_N$$
$$A_{62} = -Yn_x$$
$$A_{63} = -Yn_y$$
$$A_{64} = -Yn_z$$
$$A_{66} = v_N$$

where

$$\begin{aligned}
\gamma^* &= 1 + \frac{\rho(1-Y)K_l p + \rho Y R_g(p + P_c)}{2p\rho C_{vm} + \rho P_c((1-Y)C_{pl} + YC_{vg}) - \rho e_s(\rho(1-Y)K_l + \rho Y R_g)}, \\
e_k^* &= \frac{1}{2}u_i u_i + \frac{p\rho e_s K_l - p^2 C_{vl} - pP_c C_{pl}}{p\rho(1-Y)K_l + \rho Y R_g(p + P_c)}, \\
e^* &= \frac{\rho e_s R_g(p + P_c) - pC_{vg}(p + P_c)}{p\rho(1-Y)K_l + \rho Y R_g(p + P_c)} - \frac{p\rho e_s K_l - p^2 C_{vl} - pP_c C_{pl}}{p\rho(1-Y)K_l + \rho Y R_g(p + P_c)}.
\end{aligned}$$

A.2 Eigenvectors

$$R_{ij} = \begin{pmatrix} 1 & 1 & 1 & 0 & 0 & 0 \\ u - an_x & u & u + an_x & n_y & -n_z & 0 \\ v - an_y & v & v + an_y & -n_x & 0 & n_z \\ w - an_z & w & w + an_z & 0 & n_x & -n_y \\ h_t - av_N & e_k & h_t + av_N & un_y - vn_x & wn_x - un_z & vn_z - wn_y - e^* \\ -Y & -\dfrac{e_1}{e^*} & Y & 0 & 0 & 1 \end{pmatrix}$$

$$R_{ij}^{-1} = \begin{pmatrix} \frac{av_N+(\gamma^*-1)e_k^*}{2a^2} & \frac{-an_x-(\gamma^*-1)u}{2a^2} & \frac{-an_y-(\gamma^*-1)v}{2a^2} & \frac{-an_z-(\gamma^*-1)w}{2a^2} & \frac{\gamma-1}{2a^2} & \frac{(\gamma-1)e^*}{2a^2} \\ \frac{a^2-(\gamma^*-1)e_k^*}{a^2} & \frac{(\gamma^*-1)u}{a^2} & \frac{(\gamma^*-1)v}{a^2} & \frac{(\gamma^*-1)w}{a^2} & \frac{1-\gamma}{a^2} & \frac{(1-\gamma)e^*}{a^2} \\ \frac{-av_N+(\gamma^*-1)e_k^*}{2a^2} & \frac{an_x-(\gamma^*-1)u}{2a^2} & \frac{an_y-(\gamma^*-1)v}{2a^2} & \frac{an_z-(\gamma^*-1)w}{2a^2} & \frac{\gamma-1}{2a^2} & \frac{(\gamma-1)e^*}{2a^2} \\ \frac{v-v_Nn_y}{n_x} + \frac{e_1n_z}{e^*n_x} & n_y & \frac{n_y^2-1}{n_x} & \frac{n_yn_z}{n_x} & 0 & \frac{n_z}{n_x} \\ \frac{v_Nn_z-w}{n_x} + \frac{e_1n_y}{e^*n_x} & -n_z & -\frac{n_yn_z}{n_x} & \frac{1-n_z^2}{n_x} & 0 & \frac{n_y}{n_x} \\ \frac{e_1}{e^*} & 0 & 0 & 0 & 0 & 1 \end{pmatrix}$$

The above matrix becomes singular when $n_x = 0$. In order to avoid this, the above matrix is used only when $n_x > n_y$ and $n_x > n_z$. In other cases the following matrices are used. If $n_y > n_x$ and $n_y > n_z$, then

$$R_{ij} = \begin{pmatrix} 1 & 1 & 1 & 0 & 0 & 0 \\ u - an_x & u & u + an_x & n_y & -n_z & 0 \\ v - an_y & v & v + an_y & -n_x & 0 & n_z \\ w - an_z & w & w + an_z & 0 & n_x & -n_y \\ h_t - av_N & e_k & h_t + av_N & un_y - vn_x & wn_x - un_z - e^* & vn_z - wn_y \\ -Y & -\dfrac{e_1}{e^*} & Y & 0 & 1 & 0 \end{pmatrix}$$

$$R_{ij}^{-1} = \begin{pmatrix} \frac{av_N+(\gamma^*-1)e_k^*}{2a^2} & \frac{-an_x-(\gamma^*-1)u}{2a^2} & \frac{-an_y-(\gamma^*-1)v}{2a^2} & \frac{-an_z-(\gamma^*-1)w}{2a^2} & \frac{\gamma-1}{2a^2} & \frac{(\gamma-1)e^*}{2a^2} \\ \frac{a^2-(\gamma^*-1)e_k^*}{a^2} & \frac{(\gamma^*-1)u}{a^2} & \frac{(\gamma^*-1)v}{a^2} & \frac{(\gamma^*-1)w}{a^2} & \frac{1-\gamma}{a^2} & \frac{(1-\gamma)e^*}{a^2} \\ \frac{-av_N+(\gamma^*-1)e_k^*}{2a^2} & \frac{an_x-(\gamma^*-1)u}{2a^2} & \frac{an_y-(\gamma^*-1)v}{2a^2} & \frac{an_z-(\gamma^*-1)w}{2a^2} & \frac{\gamma-1}{2a^2} & \frac{(\gamma-1)e^*}{2a^2} \\ \frac{v_N n_x-u}{n_y}+\frac{e_1 n_z}{e^* n_y} & \frac{1-n_x^2}{n_y} & -n_x & -\frac{n_x n_z}{n_y} & 0 & \frac{n_z}{n_y} \\ \frac{e_1}{e^*} & 0 & 0 & 0 & 0 & 1 \\ \frac{w-v_N n_z}{n_y}+\frac{e_1 n_x}{e^* n_y} & \frac{n_x n_z}{n_y} & n_z & \frac{n_z^2-1}{n_y} & 0 & \frac{n_x}{n_y} \end{pmatrix}$$

If $n_z > n_x$ and $n_z > n_y$, then

$$R_{ij} = \begin{pmatrix} 1 & 1 & 1 & 0 & 0 & 0 \\ u-an_x & u & u+an_x & n_y & -n_z & 0 \\ v-an_y & v & v+an_y & -n_x & 0 & n_z \\ w-an_z & w & w+an_z & 0 & n_x & -n_y \\ h_t-av_N & e_k & h_t+av_N & un_y-vn_x-e^* & wn_x-un_z & vn_z-wn_y \\ -Y & -\frac{e_1}{e^*} & Y & 1 & 0 & 0 \end{pmatrix}$$

$$R_{ij}^{-1} = \begin{pmatrix} \frac{av_N+(\gamma^*-1)e_k^*}{2a^2} & \frac{-an_x-(\gamma^*-1)u}{2a^2} & \frac{-an_y-(\gamma^*-1)v}{2a^2} & \frac{-an_z-(\gamma^*-1)w}{2a^2} & \frac{\gamma-1}{2a^2} & \frac{(\gamma-1)e^*}{2a^2} \\ \frac{a^2-(\gamma^*-1)e_k^*}{a^2} & \frac{(\gamma^*-1)u}{a^2} & \frac{(\gamma^*-1)v}{a^2} & \frac{(\gamma^*-1)w}{a^2} & \frac{1-\gamma}{a^2} & \frac{(1-\gamma)e^*}{a^2} \\ \frac{-av_N+(\gamma^*-1)e_k^*}{2a^2} & \frac{an_x-(\gamma^*-1)u}{2a^2} & \frac{an_y-(\gamma^*-1)v}{2a^2} & \frac{an_z-(\gamma^*-1)w}{2a^2} & \frac{\gamma-1}{2a^2} & \frac{(\gamma-1)e^*}{2a^2} \\ \frac{e_1}{e^*} & 0 & 0 & 0 & 0 & 1 \\ \frac{u-v_N n_x}{n_x}+\frac{e_1 n_y}{e^* n_z} & \frac{n_x^2-1}{n_z} & \frac{n_x n_y}{n_z} & n_x & 0 & \frac{n_y}{n_z} \\ \frac{v_N n_y-v}{n_z}+\frac{e_1 n_x}{e^* n_z} & -\frac{n_x n_y}{n_z} & \frac{1-n_y^2}{n_z} & -n_y & 0 & \frac{n_x}{n_z} \end{pmatrix}$$

Appendix B

Spalart Allmaras eddy viscosity model

The standard Spalart-Allmaras model [51] is

$$\frac{D\tilde{\nu}}{Dt} = c_{b1}\tilde{S}\tilde{\nu} + \frac{1}{\sigma}\left[\nabla\cdot\left(\left(\nu+\tilde{\nu}\right)\nabla\tilde{\nu}\right) + c_{b2}\left(\nabla\tilde{\nu}\right)^2\right] - c_{w1}f_w\left(\frac{\tilde{\nu}}{d}\right)^2, \tag{B.1}$$

where $\nu_T = \tilde{\nu}f_{v1}$, $f_{v1} = \chi^3/(\chi^3+c_{v1})$ and $\chi = \tilde{\nu}/\nu$. S is either magnitude of vorticity or strain rate. The model is closed with the following coefficients and wall functions:

$$\begin{gathered}
\tilde{S} = S + \frac{\tilde{\nu}}{\kappa^2 d^2}f_{v2},\ f_{v2} = \left(1+\frac{\chi}{c_{v2}}\right)^{-3}, \\
f_w = g\left(\frac{1+c_{w3}^6}{g^6+c_{w3}^6}\right)^{1/6},\ g = r + c_{w2}(r^6-r),\ r = \frac{\tilde{\nu}}{\tilde{S}\kappa^2 d^2}, \\
c_{b1} = 0.1355,\ \sigma = \frac{2}{3},\ c_{b2} = 0.622,\ \kappa = 0.41,\ c_{v2} = 5, \\
c_{w1} = \frac{c_{b1}}{\kappa^2} + \frac{1+c_{b2}}{\sigma},\ c_{w2} = 0.3,\ c_{w3} = 2,\ c_{v1} = 7.1.
\end{gathered} \tag{B.2}$$

Combining Equation B.1 and the continuity equation, a conservative form of the SA equation can be obtained,

$$\frac{\partial\rho\tilde{\nu}}{\partial t} + \frac{\partial(\rho\tilde{\nu}u_k)}{\partial x_k} = c_{b1}\tilde{S}\rho\tilde{\nu} + \frac{1}{\sigma}\left[\nabla\cdot\left(\left(\rho\nu+\rho\tilde{\nu}\right)\nabla\tilde{\nu}\right) + c_{b2}\rho\left(\nabla\tilde{\nu}\right)^2\right] - \rho c_{w1}f_w\left(\frac{\tilde{\nu}}{d}\right)^2. \tag{B.3}$$

Because the second term in the diffusion term does not easily lend itself to a stable scheme, the diffusion term is modified to obtain the form:

$$\frac{\partial \rho\tilde{\nu}}{\partial t} + \frac{\partial(\rho\tilde{\nu}u_k)}{\partial x_k} = c_{b1}\tilde{S}\rho\tilde{\nu} + \frac{1}{\sigma}\left[(1+c_{b2})\nabla\cdot\left((\rho\nu+\rho\tilde{\nu})\,\nabla\tilde{\nu}\right) - c_{b2}\left(\rho\nu+\rho\tilde{\nu}\right)\nabla\cdot\nabla\tilde{\nu}\right] - \rho c_{w1} f_w \left(\frac{\tilde{\nu}}{d}\right)^2. \quad \text{(B.4)}$$

For cavitating flows however, Coutier-Delgosha et al. [92] observed that the eddy viscosity obtained from standard RANS models was excessive, especially near the cavity closure region, which prevented the cloud formation. Hence they suggested to modify the eddy viscosity as

$$\mu_T = \nu_T[\rho_g + (\rho_l - \rho_g)(1-\alpha)^{10}]. \quad \text{(B.5)}$$

Once ν_T is computed, the Reynolds stress is given by

$$\mathcal{R}_{ij} = -2\rho\nu_T\overline{S}_{ij}. \quad \text{(B.6)}$$